

**JAERI-Research
94-007**



**3-D THERMAL STRESS ANALYSIS OF HOT SPOTS IN
REACTOR PIPING USING BEM**

August 1994

Raghpat S. BAINS* and Jun SUGIMOTO

**日本原子力研究所
Japan Atomic Energy Research Institute**

本レポートは、日本原子力研究所が不定期に公刊している研究報告書です。

入手の問合わせは、日本原子力研究所技術情報部情報資料課（〒319-11 茨城県那珂郡東海村）あて、お申し越してください。なお、このほかに財団法人原子力弘済会資料センター（〒319-11 茨城県那珂郡東海村日本原子力研究所内）で複写による実費頒布をおこなっております。

This report is issued irregularly.

Inquiries about availability of the reports should be addressed to Information Division, Department of Technical Information, Japan Atomic Energy Research Institute, Tokaimura, Naka-gun, Ibaraki-ken 319-11, Japan.

© Japan Atomic Energy Research Institute, 1994

編集兼発行 日本原子力研究所
印刷 (株)原子力資料サービス

3-D Thermal Stress Analysis of Hot Spots
in Reactor Piping using BEM

Raghat S. BAINS* and Jun SUGIMOTO

Department of Reactor Safety Research
Tokai Research Establishment
Japan Atomic Energy Research Institute
Tokai-mura, Naka-gun, Ibaraki-ken

(Received June 20, 1994)

A three-dimensional steady state thermoelastic analysis has been conducted on the hot leg of a pressurized water reactor (PWR) containing localised hot spots resulting from fission product aerosol deposition occurring during a hypothetical severe accident. The boundary element method (BEM) of numerical solution was successfully employed to investigate the structural response of the hot leg.

Convergence of solution can be realised provided sufficiently large number of elements are employed and correct modelling of the temperature transition region (TTR) adjacent to the hot spot on the inner surface is conducted. The only correct temperature field across the TTR is that which can be represented by the interpolation functions employed in the BEM code. Further, incorrect solutions can also be generated if the TTR is too thin.

The nature of the deformation at the hot spot location depends on whether the thermal boundary condition on the outer surface of the hot leg is one of constant temperature or adiabatic. In the former only inner surface swelling was obtained, while, in the latter bulging of both the inner and outer surface was obtained.

The analysis shows that at the location of the hot spot on the inner surface large compressive stresses can be established. On the outer surface at the same location, large tensile stresses can be established. The presence of

* Science & Technology Agency (STA) Fellowship

these large stress elevations in the vicinity of the hot spot could be detrimental to the integrity of the hot leg. The tensile stresses are extremely important since they can act as sites of crack initiation and subsequent propagation. Further, if a crack like defect is already present prior to the formation of the hot spot then it is possible that once a hot spot is formed the elevated tensile stresses could lead to its propagation. Once a crack propagates through the thickness, leak worthiness of the hot leg comes into question. Consequently, additional analysis incorporating the effects of plasticity and temperature dependence of the material properties must be conducted to ascertain the integrity of the hot leg.

Keywords: Severe Accident, BEM, Integral Equation, 3D Thermal Stress, Linear Elastic, Reactor Piping, Hot Spot.

BEMによる原子炉配管ホットスポットの3次元熱応力解析

日本原子力研究所東海研究所原子炉安全工学部

Raghpit S. BAINS*・杉本 純

(1994年6月20日受理)

PWRのシビアアクシデント時において、ホットレグ内にFP沈着により形成される局部ホットスポットを対象とした3次元熱弾性解析を実施した。本解析では境界要素法(BEM)を数値解析法として適用し、ホットレグの構造応答を調べた。

要素数が十分にあり、かつ配管内壁のホットスポットに近接する温度遷移領域(TTR)を適切にモデル化すれば、解は収束する。BEMコードで用いられる内挿関数により表現可能な、TTR内の温度場だけが許容できる。さらに、TTRが薄過ぎると数値不安定により不正確な解を与えることがある。

ホットスポット近傍における変形は、ホットレグ外壁の熱的境界条件が一定温度か断熱かに依存する。一定温度の場合、内側表面の膨張のみが生じる。一方、断熱の場合は、内側及び外側両表面が膨張する。

解析から、内側表面のホットスポット位置において、大きな垂直方向の圧縮応力が形成されることが示された。同じ場所の外側表面では、大きな垂直方向の引張り応力が生じる。ホットスポット近傍におけるこのような大きな応力増加の存在は、ホットレグの構造健全性にとっては好ましくない。引張り応力は、亀裂の発生及びその後の伝播に作用するので極めて重要である。さらに、ホットスポットの形成以前に亀裂状欠陥が存在する場合は、一旦ホットスポットが形成されると、大きな引張り応力が亀裂を伝播させる可能性がある。亀裂が配管内肉厚方向に伝播すると、ホットレグの気密性が問題となり得る。したがって、ホットレグの健全性を確認するには、材料の物性値に及ぼす塑性と温度依存性の影響を考慮した解析をさらに実施する必要がある。

Contents

1. Introduction	1
1.1 General	1
1.2 Structural Response of RCS Piping	1
1.3 Scope & Objectives of Present Work	1
2. Thermoelasticity & BEM	3
2.1 Governing Equations of Thermoelasticity	3
2.2 Boundary Element Method(BEM)	4
3. PWR Hot Leg Modelling	8
3.1 Modelling Assumptions	9
3.2 Convergence Studies	9
3.3 TTR Modelling	15
3.4 Conclusions	21
4. Numerical Solutions	22
4.1 Hot Spot in Straight Section of Hot Leg	22
4.2 Hot Spot at Bend Section of Hot Leg	38
4.3 Conclusions	53
5. Final Conclusions	59
Acknowledgements	60
Bibliography	61
Appendix A Analytical & Numerical Solution	62
Appendix B Transformations	65

目 次

1. 序	1
1.1 背 景	1
1.2 原子炉冷却系配管の構造的応答	1
1.3 本研究の範囲と目的	1
2. 熱弾性と境界値法 (BEM)	3
2.1 熱弾性を支配する方程式	3
2.2 境界値法 (BEM)	4
3. PWRホットレグのモデル化	8
3.1 モデルの仮定	9
3.2 収束解析	9
3.3 TTRモデル	15
3.4 ま と め	21
4. 数 値 解	22
4.1 ホットレグ直管におけるホットスポット	22
4.2 ホットレグ曲管におけるホットスポット	38
4.3 ま と め	53
5. 結 論	59
文 献	61
付録A 解析解及び数値解	62
付録B 変 形	65

List of Figures

3.1	PWR Hot leg	8
3.2	Problem definition	10
3.3	Boundary conditions	11
3.4	Definition of temperature transition region (TTR)	11
3.5	Mesh1	12
3.6	Mesh2	13
3.7	Mesh3	13
3.8	Mesh4	14
3.9	Mesh5	14
3.10	U_r : Inner surface, $z = 1.0m$	16
3.11	U_r : Inner surface, $z = 0.0m$	16
3.12	U_θ : Inner surface, $z = 1.0m$	17
3.13	U_θ : Inner surface, $z = 0.0m$	17
3.14	TTR size variation: U_r and U_θ at $z = 1.0m$ along inner surface.	18
3.15	TTR size variation: U_r and U_θ at $z = 0.0m$ along inner surface.	19
3.16	Deformation at $z = 1.0m$ for Mesh4: Linear temperature.	20
3.17	Deformation at $z = 1.0m$ for Mesh4: Step temperature.	20
4.1	Mesh for 1/4 analysis of problem	23
4.2	Comparison of displacement variations	23
4.3	U_r variation on inner surface	25
4.4	U_θ variation on inner surface	25
4.5	U_z variation on inner surface	26
4.6	Contour plot of U_z on inner surface	26
4.7	Hot leg deformation	27
4.8	ϵ_{rr} on inner surface	28
4.9	$\epsilon_{\theta\theta}$ on inner surface	28
4.10	ϵ_{zz} on inner surface	29
4.11	$\epsilon_{r\theta}$ on inner surface	29
4.12	ϵ_{rz} on inner surface	29
4.13	$\epsilon_{\theta z}$ on inner surface	30
4.14	ϵ_{rr} on outer surface	30
4.15	$\epsilon_{\theta\theta}$ on outer surface	31
4.16	ϵ_{zz} on outer surface	31
4.17	$\epsilon_{r\theta}$ on outer surface	32
4.18	ϵ_{rz} on outer surface	32
4.19	$\epsilon_{\theta z}$ on outer surface	33
4.20	σ_{rr} on inner surface	33
4.21	$\sigma_{\theta\theta}$ on inner surface	33
4.22	σ_{zz} on inner surface	34
4.23	$\sigma_{r\theta}$ on inner surface	34
4.24	σ_{rz} on inner surface	34
4.25	$\sigma_{\theta z}$ on inner surface	35
4.26	σ_{rr} on outer surface	36
4.27	$\sigma_{\theta\theta}$ on outer surface	36
4.28	σ_{zz} on outer surface	36

4.29	$\sigma_{r\theta}$ on outer surface	37
4.30	σ_{rz} on outer surface	37
4.31	$\sigma_{\theta z}$ on outer surface	37
4.32	Bend geometry definition	38
4.33	Mesh for bend analysis	40
4.34	Cylindrical polar Coordinates centered on hot leg bend axis.	40
4.35	Bend deformation: temperature prescribed on outer surface	41
4.36	Inner surface variation of U_r	42
4.37	Inner surface variation of U_{θ_2}	43
4.38	Inner surface variation of $U_{x'}$	43
4.39	σ_{rr} on inner surface	45
4.40	$\sigma_{\theta_2\theta_2}$ on inner surface	45
4.41	$\sigma_{x'x'}$ on inner surface	45
4.42	$\sigma_{r\theta_2}$ on inner surface	46
4.43	$\sigma_{rx'}$ on inner surface	46
4.44	$\sigma_{\theta_2x'}$ on inner surface	46
4.45	σ_{rr} on outer surface	47
4.46	$\sigma_{\theta_2\theta_2}$ on outer surface	47
4.47	$\sigma_{x'x'}$ on outer surface	47
4.48	$\sigma_{r\theta_2}$ on outer surface	48
4.49	$\sigma_{rx'}$ on outer surface	48
4.50	$\sigma_{\theta_2x'}$ on outer surface	48
4.51	Bend deformation: adiabatic boundary condition on outer surface	49
4.52	Temperature variation on outer surface	50
4.53	Inner surface variation of U_r	51
4.54	Inner surface variation of U_{θ_2}	51
4.55	Inner surface variation of $U_{x'}$	52
4.56	σ_{rr} on inner surface	55
4.57	$\sigma_{\theta_2\theta_2}$ on inner surface	55
4.58	$\sigma_{x'x'}$ on inner surface	55
4.59	$\sigma_{r\theta_2}$ on inner surface	56
4.60	$\sigma_{rx'}$ on inner surface	56
4.61	$\sigma_{\theta_2x'}$ on inner surface	56
4.62	σ_{rr} on outer surface	57
4.63	$\sigma_{\theta_2\theta_2}$ on outer surface	57
4.64	$\sigma_{x'x'}$ on outer surface	57
4.65	$\sigma_{r\theta_2}$ on outer surface	58
4.66	$\sigma_{rx'}$ on outer surface	58
4.67	$\sigma_{\theta_2x'}$ on outer surface	58
A.1	Mesh refinement for 1/8 modelling of Hot leg.	63
A.2	Temperature variation across thickness.	64
A.3	Analytic and numerical solutions.	64
B.1	Rotation about y axis.	65
B.2	Definition of cylindrical polar coordinates.	66

Chapter 1

Introduction

1.1 General

Since the accidents at the Three Mile Island Unit 2 (TMI-2) in 1979 and at the Chernobyl Unit 4 in 1986 many research activities have been conducted to gain a better understanding of severe nuclear accident sequences and consequences. This is a direct consequence of the fact that such a severe accident in a nuclear power plant anywhere in the world can affect nuclear operations considerably.

The consequences of a severe nuclear accident necessitates research to be conducted to predict possible accident scenarios. To this end, Japan Atomic Energy Research Institute (JAERI) has initiated many severe accident research programs to better understand and to predict the physical and chemical phenomena which might occur in severe accidents. Abe, Sugimoto and Kajimoto [1] have summarized the analytical and experimental research activities at JAERI.

In 1993, JAERI initiated the 'Wide Range Piping Integrity Demonstration' project, WIND. The aim of WIND is to demonstrate the reliability of piping in nuclear power plants under severe accident conditions. The objectives of this project are two fold, firstly, to evaluate the fission product aerosol behaviour (i.e., deposition, revaporization and resuspension) and secondly to demonstrate the reliability of piping under localised heat input due to decay of deposited fission products.

1.2 Structural Response of RCS piping

During a hypothetical accident, degradation of the reactor core could give rise to the release of fission product aerosols. There is a possibility these fission product aerosols could get transported into the Reactor Coolant System (RCS) piping. If such an event does occur, then it is also possible that deposition of the aerosols could occur on the reactor piping wall due to sedimentation or inertial impact. These deposited fission product aerosols will produce decay heat. This decay heat will generate localised hot spots which in turn will produce thermal stresses. Therefore, it is imperative that the structural response of the RCS piping is understood to predict possible RCS piping failure in advance of the reactor containment failure.

1.3 Scope & Objectives of Present Work

A numerical study is conducted on the hot leg of a pressurized water reactor (PWR) containing a localised hot spot, resulting from fission product deposition. This problem could have been solved using the finite element method (FEM), by employing shell elements, which would reduce the numerical problem size considerably. The main drawback of these elements is

they only generate an average value of the field quantities such as displacements and stresses, they cannot show the variation of the field quantities through pipe thickness. In the analysis of the hot spot, it is envisaged that the inner and outer surfaces of the pipe in the vicinity of the hot spot will behave differently due to the complex thermal stress boundary conditions. Consequently, only a complete three dimensional analysis can represent this type of problem accurately.

The objectives of the present study are three fold. Firstly, to investigate the linear elastic structural response of the hot leg resulting from the presence of hot spots. Secondly, show that the Boundary Element Method (BEM) can be successfully employed to solve problems of such complexity. And thirdly, conduct an extensive numerical convergence study based on mesh refinement to ascertain the validity of the solutions obtained.

To ease the computation, the hot leg, which comprises of a circular cross-section pipe with a straight section and a bend will be considered in two separate parts. The first part of the analysis will concentrate on the straight section of the hot leg containing a local hot spot without the presence of the bend. The latter part of the analysis will investigate the bend section containing the hot spot.

This report is divided into five chapters, the first of which is the Introduction. In Chapter 2, the numerical formulation of the Boundary Element Method (BEM), in conjunction with thermal stress analysis is presented. The main advantages of this numerical solution technique are presented with respect to the well established finite element method. A brief description of the BEM code is also given. In Chapter 3, the modelling assumptions and numerical convergence analysis are presented. Here a convergence analysis is performed on the straight section of the pipe containing the hot spot. Attention is also focused on the region adjacent to the hot spot where the temperature changes from the average inner wall temperature to the hot spot temperature. Solution sensitivity to the size of this region and different temperature boundary conditions (*i.e.*, linear and step change) are presented. In Chapter 4, more realistic severe accident thermal boundary conditions and more accurate hot leg geometry is employed in the analysis. Here solutions are presented for the straight and bend section of a hot leg containing a hot spot. To get a better understanding of the structural behaviour of the straight section of the hot leg containing a hot spot, an auxiliary problem is also solved containing no hot spot but otherwise employing identical boundary conditions. In the analysis of the bend section the solution obtained, is based on an extremely complex interaction of the bend geometry and the boundary conditions. Two separate solutions are presented, one employing a constant temperature and the other an adiabatic boundary condition (*i.e.*, zero heat flux) on the outer surface. The final conclusions and recommendations for future work are presented in Chapter 5.

Chapter 2

Thermoelasticity & BEM

2.1 Governing Equations of Thermoelasticity

Derivation of the governing equations of thermoelasticity can be found in the work of Boley and Weiner [2]. Essentially, for infinitesimal deformations and linear isotropic materials the strain–displacement relationship in cartesian coordinates (1,2,3) is

$$\varepsilon_{ij} = \frac{1}{2}(u_{i,j} + u_{j,i}), \quad i, j = 1, 2, 3 \quad (2.1)$$

and the following notation is used to denote differentiation:

$$f_{,r} = \frac{\partial f}{\partial r}.$$

The stress–strain relationship can be expressed as

$$\sigma_{ij} = \lambda \delta_{ij} \sum_{k=1}^3 \varepsilon_{kk} + 2\mu \varepsilon_{ij} - (3\lambda + 2\mu) \delta_{ij} \alpha (\Theta - \Theta_0) \quad (2.2)$$

and the Fourier law of heat conduction as

$$q_i = -\kappa \Theta_{,i}. \quad (2.3)$$

In equations (2.1)–(2.3), u_i is displacement vector, ε_{ij} is strain tensor, σ_{ij} is stress tensor, Θ_0 is initial temperature, Θ is final temperature, q_i is heat flux vector, α is the coefficient of thermal expansion, κ is thermal conductivity, δ_{ij} is the Kronecker Delta, λ and μ are Lamé constants.

In the absence of body forces, heat sources, inertia and rate of change of temperature, application of the laws of conservation of momentum and energy gives

$$\mu u_{i,jj} + (\lambda + \mu) u_{j,ij} = (3\lambda + 2\mu) \alpha \Theta_{,i} \quad (2.4)$$

and

$$\kappa \Theta_{,jj} = (3\lambda + 2\mu) \alpha \Theta_0 \dot{u}_{j,j}. \quad (2.5)$$

Where the dot over the displacement term u in equation (2.5) denotes differentiation with respect to time. It has been shown, see Boley *et. al.*, [2], that the term $\dot{u}_{j,j}$ is generally negligible from an engineering point of view. Thus, equation (2.5) can be simplified further to

$$\kappa \Theta_{,jj} = 0. \quad (2.6)$$

This simplification leads to uncoupling of the momentum and energy balance equations and implies that a steady state thermoelastic problem can be solved in two steps. The first step involves solving equation (2.6) for the temperature distribution. Subsequently, equation (2.4) is solved for the displacements with the known temperature distribution.

2.2 Boundary Element Method (BEM)

Due to the difficulty of obtaining analytical solutions for three-dimensional problems, the governing equations must be solved numerically. Generally, the two most popular numerical solution techniques are the finite element method (FEM) [3] and the boundary element method (BEM) [4]. The main disadvantage of FEM is the cost of preparing mesh data since the whole problem domain has to be discretized. Further, it generates vast amounts of unwanted information at internal nodal points and elements which may never be used in linear homogeneous problems. For steady state problems BEM gives better numerical accuracy than FEM.

The boundary element method gives rise to integral equations which relate to boundary data only. This method offers a reduction in the dimensionality of the problem by one *i.e.*, for three-dimensional problems only the surface of the domain need be discretized. This reduction in dimensionality gives rise to a substantial reduction in data preparation, a smaller system of equations to be solved, and also significant reductions in computer storage requirements.

2.2.1 Regularised Boundary Integral Equation

A regularised boundary integral equation relating displacements u_i , tractions $t_i (= \sigma_{ij}n_j)$, temperature Θ and heat flux q at the surface Γ , can be expressed in the absence of body forces as

$$\begin{aligned} \int_{\Gamma} T_{ij}(x', x) [u_i(x') - u_i(x)] d\Gamma &= \int_{\Gamma} U_{ij}(x', x) t_i(x') d\Gamma \\ &+ \alpha\mu \left(\frac{1+\nu}{1-\nu} \right) \int_{\Gamma} G_{ij,ik}(x', x) n_i(x') \Theta(x') d\Gamma \\ &+ \frac{\alpha\mu}{\kappa} \left(\frac{1+\nu}{1-\nu} \right) \int_{\Gamma} G_{ij,i}(x', x) q(x') d\Gamma. \end{aligned} \quad (2.7)$$

This equation is valid providing u_i is assumed to be Hölder-continuous. Details of the regularization procedure can be found in the work of Matsumoto and Tanaka [5]. This regularization of the boundary integral equations implies that no Cauchy-principal-value integrals need to be defined. In equation (2.7), $n_i(x')$ is the unit outward normal vector, ν is Poisson's ratio, x' and x are points on the surface Γ and represent the collocation and field points respectively. The tensors $U_{ij}(x', x)$ and $T_{ij}(x', x)$ are known fundamental displacement and traction solutions respectively for a point force in an infinite domain. The term $G_{ij}(x', x)$ is the Galerkin tensor. Expressions for the tensors $U_{ij}(x', x)$, $T_{ij}(x', x)$ and $G_{ij}(x', x)$ can be found in ref [6]. Terms $\Theta(x')$ and $q(x')$ represent known temperature and heat flux respectively. The solution procedure is that the integral equations are solved for unknowns *i.e.*, u_i , if t_i is prescribed or for t_i , if u_i is specified. Resulting solutions give displacements, tractions and stresses everywhere on the boundary. A knowledge of these allows displacements and stresses to be obtained at any specified interior points.

The boundary integral equation (2.7) requires knowledge of thermal input data at each node. Integral equations using similar ideas as above can also be established for Θ and q . Thus, Θ and q can also be obtained using BEM. Analysis for the heat transfer problem is much easier due to its scalar characteristics.

2.2.2 Numerical Discretisation of Integral Equation

The boundary integral equation (2.7) can be solved numerically by discretizing the surface Γ of the problem into N elements with \mathcal{M} nodes per element. For a three-dimensional problem, the surface of the problem domain is divided into two-dimensional elements. These elements can be curved, the surface of which is defined in terms of intrinsic coordinates of the element ξ, η

where $(-1 \leq \xi, \eta \leq 1)$. Over each element the geometry, displacements, tractions, temperature and heat flux are represented in terms of nodal values x^a , u^a , t^a , Θ^a and q^a as

$$x(\xi, \eta) = \sum_{a=1}^M \mathcal{N}^a(\xi, \eta) x^a, \quad (2.8)$$

$$u(\xi, \eta) = \sum_{a=1}^M \mathcal{N}^a(\xi, \eta) u^a, \quad (2.9)$$

$$t(\xi, \eta) = \sum_{a=1}^M \mathcal{N}^a(\xi, \eta) t^a, \quad (2.10)$$

$$\Theta(\xi, \eta) = \sum_{a=1}^M \mathcal{N}^a(\xi, \eta) \Theta^a \quad (2.11)$$

and

$$q(\xi, \eta) = \sum_{a=1}^M \mathcal{N}^a(\xi, \eta) q^a, \quad (2.12)$$

where $\mathcal{N}^a(\xi, \eta)$ are shape functions or interpolation functions. These shape functions can be found in ref [4, 6]. With the boundary discretised, the integral equation can be written as

$$\begin{aligned} \sum_{\beta=1}^N \int_{\Gamma_\beta} T_{ij}(x', x) [u_i(x') - u_i(x)] d\Gamma_\beta &= \sum_{\beta=1}^N \int_{\Gamma_\beta} U_{ij}(x', x) t_i^\beta(x') d\Gamma_\beta \\ &+ \alpha\mu \left(\frac{1+\nu}{1-\nu} \right) \sum_{\beta=1}^N \int_{\Gamma_\beta} G_{ij,ik}(x', x) n_i^\beta(x') \Theta^\beta(x') d\Gamma_\beta \\ &+ \frac{\alpha\mu}{\kappa} \left(\frac{1+\nu}{1-\nu} \right) \sum_{\beta=1}^N \int_{\Gamma_\beta} G_{ij,i}(x', x) q^\beta(x') d\Gamma_\beta. \end{aligned} \quad (2.13)$$

where

$$\Gamma = \sum_{\beta=1}^N \Gamma_\beta. \quad (2.14)$$

In equation (2.7) the integrals are evaluated locally and the differential area $d\Gamma_\beta(x)$ must be redefined according to

$$d\Gamma_\beta(x) = J^\beta(\xi, \eta) d\xi d\eta. \quad (2.15)$$

This is the transformation required to go from the global coordinates x_i to the local coordinate system (ξ, η) defined on the β^{th} element. The term $J^\beta(\xi, \eta)$ is the Jacobian of the transformation. Substitution of equations (2.8)–(2.12) and (2.15) into (2.13) results in

$$\begin{aligned} \sum_{\beta=1}^N \sum_{a=1}^M [u_i(x') - u_i^{\beta a}(x(\xi, \eta))] \int_{-1}^{+1} \int_{-1}^{+1} T_{ij}^{\beta a}(x', x(\xi, \eta)) \mathcal{N}^a(\xi, \eta) J^\beta(\xi, \eta) d\xi d\eta &= \\ \sum_{\beta=1}^N \sum_{a=1}^M t_i^{\beta a}(x') \int_{-1}^{+1} \int_{-1}^{+1} U_{ij}^{\beta a}(x', x(\xi, \eta)) t_i^\beta(x') \mathcal{N}^a(\xi, \eta) J^\beta(\xi, \eta) d\xi d\eta &+ \\ \alpha\mu \left(\frac{1+\nu}{1-\nu} \right) \sum_{\beta=1}^N \sum_{a=1}^M \Theta^{\beta a}(x') \int_{-1}^{+1} \int_{-1}^{+1} G_{ij,ik}^{\beta a}(x', x(\xi, \eta)) n_i^\beta(x') \mathcal{N}^a(\xi, \eta) J^\beta(\xi, \eta) d\xi d\eta &+ \\ \frac{\alpha\mu}{\kappa} \left(\frac{1+\nu}{1-\nu} \right) \sum_{\beta=1}^N \sum_{a=1}^M q^{\beta a}(x') \int_{-1}^{+1} \int_{-1}^{+1} G_{ij,i}^{\beta a}(x', x(\xi, \eta)) \mathcal{N}^a(\xi, \eta) J^\beta(\xi, \eta) d\xi d\eta. \end{aligned} \quad (2.16)$$

Defining,

$$P_{ij}^{\beta a}(x', x(\xi, \eta)) = \int_{-1}^{+1} \int_{-1}^{+1} T_{ij}^{\beta a}(x', x(\xi, \eta)) \mathcal{N}^a(\xi, \eta) J^\beta(\xi, \eta) d\xi d\eta, \quad (2.17)$$

$$Q_{ij}^{\beta a}(x', x(\xi, \eta)) = \int_{-1}^{+1} \int_{-1}^{+1} U_{ij}^{\beta a}(x', x(\xi, \eta)) t_i^\beta(x') \mathcal{N}^a(\xi, \eta) J^\beta(\xi, \eta) d\xi d\eta, \quad (2.18)$$

$$D_{ij}^{\beta a}(x', x(\xi, \eta)) = \alpha\mu \left(\frac{1+\nu}{1-\nu} \right) \int_{-1}^{+1} \int_{-1}^{+1} G_{ij,ik}^{\beta a}(x', x(\xi, \eta)) n_i^\beta(x') \mathcal{N}^a(\xi, \eta) J^\beta(\xi, \eta) d\xi d\eta \quad (2.19)$$

and

$$W_{ij}^{\beta a}(x', x(\xi, \eta)) = \frac{\alpha\mu}{\kappa} \left(\frac{1+\nu}{1-\nu} \right) \int_{-1}^{+1} \int_{-1}^{+1} G_{ij,i}^{\beta a}(x', x(\xi, \eta)) \mathcal{N}^a(\xi, \eta) J^\beta(\xi, \eta) d\xi d\eta \quad (2.20)$$

equation (2.16) can be reduced to

$$\begin{aligned} \sum_{\beta=1}^N \sum_{a=1}^M P_{ij}^{\beta a}(x', x(\xi, \eta)) [u_i(x') - u_i^{\beta a}(x(\xi, \eta))] &= \sum_{\beta=1}^N \sum_{a=1}^M Q_{ij}^{\beta a}(x', x(\xi, \eta)) t_i^{\beta a}(x') \\ &+ \sum_{\beta=1}^N \sum_{a=1}^M D_{ij}^{\beta a}(x', x(\xi, \eta)) \Theta^{\beta a}(x') \\ &+ \sum_{\beta=1}^N \sum_{a=1}^M W_{ij}^{\beta a}(x', x(\xi, \eta)) q^{\beta a}(x'). \end{aligned} \quad (2.21)$$

If the collocation point x' and the field point x are coincident the term $[u_i(x') - u_i^{\beta a}(x(\xi, \eta))]$ tends to zero and the fundamental traction tensor $T_{ij}(x', x)$ becomes weakly singular. Using mapping techniques [5, 7] this weak singularity can also be cancelled and the kernels can be evaluated very accurately using standard Gaussian quadrature formulae. As the collocation point x' passes through all the nodal points, the following system of linear algebraic equation is obtained:

$$\mathbf{H}\mathbf{u} = \mathbf{C}\mathbf{t} + \mathbf{D}\Theta + \mathbf{W}\mathbf{q}, \quad (2.22)$$

where the matrices \mathbf{H} , \mathbf{C} , \mathbf{D} and \mathbf{W} contain integrals of T_{ij} , U_{ij} , $G_{ij,ik}$ and $G_{ij,i}$ respectively. The vectors $\mathbf{u}(= u(x') - u(x))$ and \mathbf{t} contain boundary displacements and tractions components, respectively. Known nodal temperature and heat flux are contained in vectors Θ and \mathbf{q} . Equations (2.22) are then rearranged in the form

$$\mathbf{A}\mathbf{x} = \mathbf{f}, \quad (2.23)$$

where the vector \mathbf{x} contains the boundary unknowns u_i and t_i . The matrix \mathbf{A} results from rearrangement of \mathbf{H} and \mathbf{C} . The vector \mathbf{f} is composed from rearrangement of \mathbf{H} and \mathbf{C} together with the addition of the terms $(\mathbf{D}\Theta + \mathbf{W}\mathbf{q})$. The coefficient matrix \mathbf{A} is both non-symmetric and fully populated. A banded matrix can be obtained if the domain is divided into sub-regions, for each of which an integral equation can be established. These systems of algebraic equations can be solved with any matrix solution technique. The final solution gives the boundary unknowns in a piece-wise approximation. It must be noted that the unknowns are a mixture of displacements and tractions, rather than the displacements only as in FEM. This is a consequence of the BEM being a "mixed" formulation and constitutes an important advantage over the FEM.

2.2.3 Code Development

The program written in Fortran code, which solves the regularised boundary integral equation was developed at Shinshu University. All the integrals are evaluated numerically using standard Gaussian quadrature. The merit of this code is that since the singularities of the kernels have been explicitly cancelled out in advance through the regularization procedure, all the integrals can be evaluated accurately.

The input data file for this code requires thermal boundary conditions (*i.e.*, temperature and heat flux) at each nodal point of the mesh, in addition to the displacement and traction boundary conditions. Thus variation of temperature and heat flux must be known in advance of solving equation (2.7).

Generally, if two separate codes are used, one to generate thermal boundary conditions and the other to perform the thermal stress analysis then two sets of input data files are required. For realistic problems these data files tend to become large. Further, for two input data files the possibility of errors being introduced increases relative to the case when only one data file is used.

The ideal case would be, one in which a single program performs both the thermal analysis and thermal stress analysis. This coupling is difficult due to the scalar and vector characteristics of the two problems. Nevertheless, the original code was modified enabling the heat transfer analysis and the thermal stress analysis to be conducted consecutively in a single program. Thus a single input data file is required, which contains boundary conditions for the heat transfer analysis (*i.e.*, a mixture of temperature and heat flux) and boundary conditions for the stress analysis (*i.e.*, a mixture displacements and tractions). This reduces the likelihood of errors being introduced since only a single data file is needed, furthermore, the combined code requires less user intervention. The program first solves the thermal problem, generating temperature where heat flux is prescribed and heat flux where temperature is prescribed. The temperature and heat flux is then automatically fed into the thermal stress analysis part of the program.

Additional programs have also been written which facilitate the pre-processing and post-processing of the data needed and generated by the BEM code. In the pre-processing an interface program has been developed which can be used to prescribe different thermal stress boundary conditions at the nodal points of the mesh. A simple mesh generator is also included in the interface program which allows use of eight-node quadrilateral and six-node triangular elements. The triangular elements are generated from the quadrilateral elements. Without this interface program the generation of the boundary element mesh and the associated boundary conditions at each nodal point would be extremely laborious. In the post-processing a mesh plotting program has been developed that allows the boundary element mesh before and after the analysis to be examined. This program produces a global or local view of the mesh deformation relative to the original undeformed mesh.

Chapter 3

PWR Hot Leg Modelling

Part of the primary circuit of a Pressurized Water Reactor (PWR) comprises of the reactor pressure vessel, hot leg and the steam generator, see figure 3.1. The hot leg consists

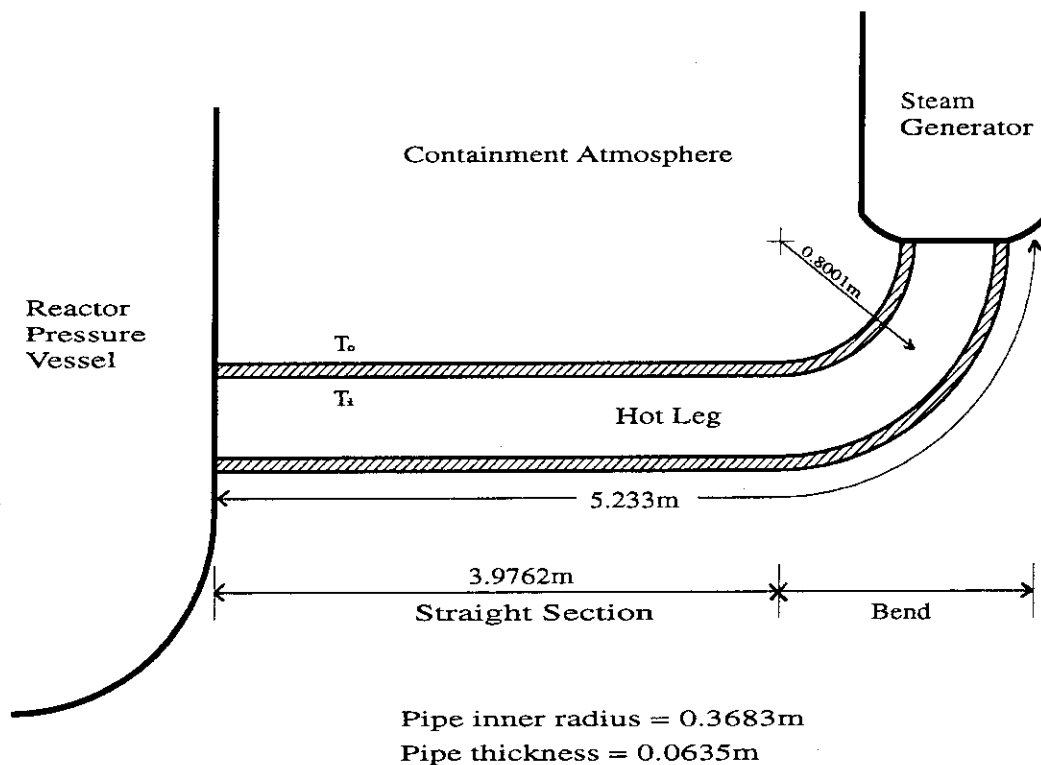


Figure 3.1: PWR Hot leg

of a circular cross-section pipe with a straight section and a bend. Typically, the length of straight section is 3.9762m and the total length of the pipe is 5.233m, with inner radius and pipe thickness of 0.3683m and 0.0635m, respectively. The quantities T_i and T_o denote the inner and outer wall temperatures of the hot leg.

The actual bend section comprising the hot leg forms an angle of approximately 60° with the axis of the horizontal pipe. A 90° bend is chosen for the present analysis since the fission product aerosol deposition models under development at JAERI are at present limited to this geometrical configuration.

Water at high temperature and pressure from the reactor pressure vessel is fed via the hot leg into the steam generator. During a hypothetical severe accident, fission product aerosols could be transported in the primary circuit. Fission product aerosol deposition due to

sedimentation and inertial impact could occur on the piping wall. The amount of deposition will be governed by the flow rate. This deposition could occur in the straight section, the bend section or in both. Fission product decay heat from the deposited aerosols will subsequently determine the structural behaviour of the hot leg. Analysis conducted at JAERI show that during a possible severe accident, the inner and outer pipe wall temperatures of the hot leg can be of the order 926°C and 150°C , respectively.

3.1 Modelling Assumptions

Due to the complexity of the problem, assumptions must be made in the modelling so that solutions can be obtained. As regards this it will be assumed that the pipe behaviour is governed by the laws of linear elasticity. The temperature of the inner surface of the pipe is the same as the average temperature of the fluid. The deposited fission product aerosols form a regular surface patch on the pipe wall which can be characterised by an average temperature. No modelling of the fission product aerosols is attempted, only the effects of temperature are considered. Decay heat from the deposition does not change the average temperature of the inner and outer surface of the pipe. All temperature values are steady state.

3.2 Convergence Studies

To verify the applicability of BEM to piping problems of this type, a representative problem was selected since the actual dimensions and boundary conditions of the hot leg were not available when the convergence analysis was conducted. This problem which consists of a pipe with a hot spot, differs slightly from the one shown in figure 3.1, nevertheless it will give an idea of the general solution behaviour. The contents of this study will then form a basis on which an analysis can be conducted on a hot spot located in the straight and bend section of the hot leg as shown in figure 3.1.

For the convergence analysis consider a pipe of length L , inner and outer radius r_i and r_o respectively, as shown in figure 3.2. The hot spot of length L_h , subtends an angle γ on the pipe wall. It is located at distance $L/2$ from either end of the pipe. The inner wall, outer wall and hot spot temperatures are denoted by T_i , T_o and T_h , respectively. Values of the variables shown in figure 3.2 are listed in table 3.1, where E is Young's Modulus, ν is Poisson's ratio, κ is the thermal conductivity and α is the linear thermal expansion coefficient. This analysis assumes that the pipe has no internal pressure. In this convergence analysis attention is only focused on the variation of the displacement components.

The inner surface of the pipe is at temperature T_i , while the hot spot temperature is T_h , thus in the vicinity of the hot spot there is a step change in the temperature boundary conditions (*i.e.*, jump from T_i to T_h). Clearly, such a temperature discontinuity will not occur in a real situation, where a small region will exist adjacent to the hot spot in which there is a continuous change of temperature from T_i to T_h . In the modelling a thin region adjacent to the hot spot is introduced in which a change of temperature from T_i to T_h can be simulated.

Due to the symmetry of the problem only 1/4 of the geometry will be considered for analysis. Boundary conditions needed by the BEM for the thermal analysis and the thermal stress analysis are shown in figure 3.3. Here the shaded areas represents different boundary conditions in terms of the temperature, heat flux, displacements and tractions. In the thermal analysis, on the symmetry planes, adiabatic (*i.e.*, zero heat flux) boundary conditions were prescribed. In the thermal stress analysis, the inner and outer walls of the pipe are traction free (*i.e.*, $t_i = 0$), the pipe is also constrained in the axial direction. The x - z symmetry plane is constrained in the y -direction. At the point $(0, r_i, 0)$, displacement in the x -direction was also

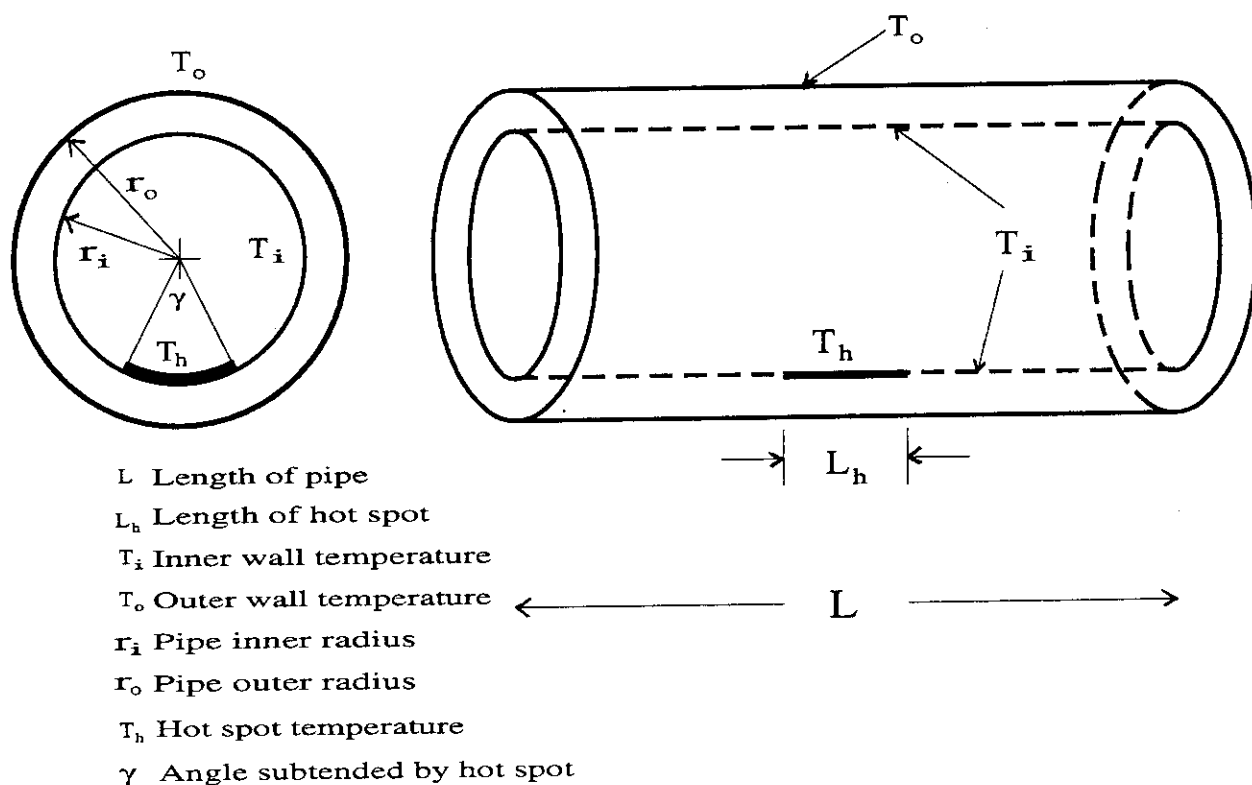


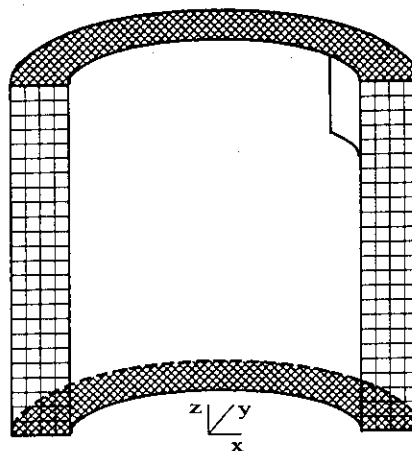
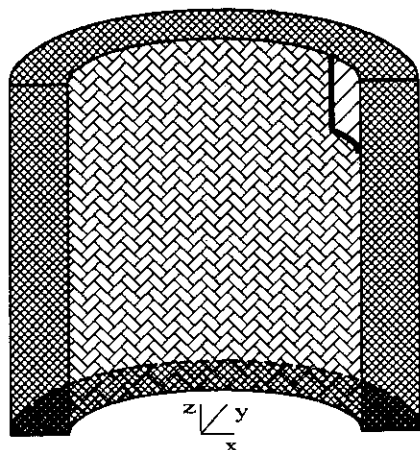
Figure 3.2: Problem definition





Variable	Value
r_i	0.55 m
r_o	0.61 m
L	2.0 m
L_h	0.4 m
γ	20°
T_o	500K
T_i	750K
T_h	1500K
κ	20.0W/(m · K)
α	18.0 × 10 ⁻⁶ C ⁻¹
E	0.17 × 10 ¹² kg/m ²
ν	0.3




Table 3.1: Problem dimensions.

Thermal analysis

Thermal stress analysis



-  Zero heat flux
-  Hot spot temperature
-  Inner surface temperature
-  Outer surface temperature

-  $t_1=0 \quad t_2=0 \quad u_3=0$
-  $t_1=0 \quad u_2=0 \quad t_3=0$
-  $t_i=0$ For all other surfaces

At nodal points must also prescribe temperature & heat flux as obtained from the thermal analysis.

Figure 3.3: Boundary conditions

constrained to prevent rotation and translation of the body.

The thick line adjacent to the hot spot in figure 3.3 represents a small region referred to hereafter as the temperature transition region (TTR), in which an approximation for the temperature change from T_i to T_h can be prescribed. No information is available for this region. A linear temperature rise from T_i to T_h will be assumed although any other variation is equally valid for the analysis. This region was defined to be of constant width (*i.e.*, $S_1 = S_2$) adjacent to the hot spot, see figure 3.4. The length S_1 was chosen such that the arc formed by S_1 subtended

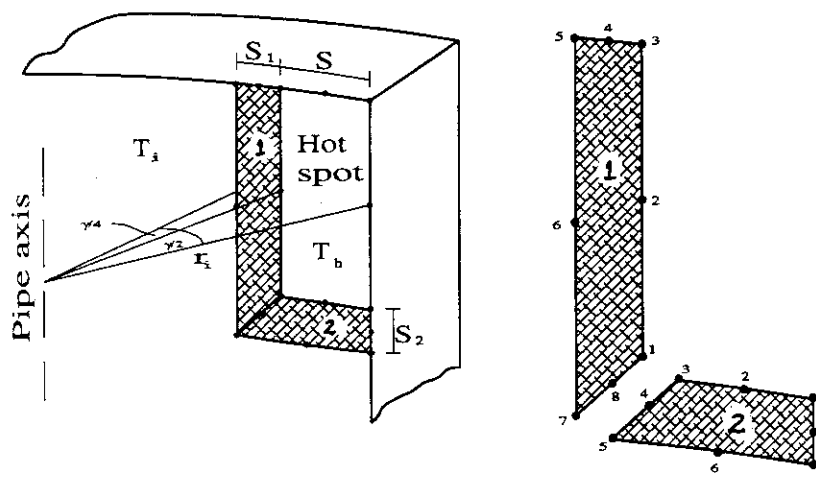


Figure 3.4: Definition of temperature transition region (TTR)

an angle of $\gamma/4$ with respect to the axis of the pipe, γ is defined in figure 3.2. To prescribe temperature variation on the TTR consider this region to be defined by two boundary elements only, with local element numbering system as shown in figure 3.4. For a linear temperature variation across the TTR one must prescribe temperature T_h on nodes 1, 2, 3 and prescribe

temperature T_i on nodes 5, 6, 7. On the remaining nodes 4 and 8 assign temperature $(T_i + T_h)/2$.

For the convergence analysis five meshes were designed for the quarter symmetry the problem possess. These meshes will be designated as Mesh1, Mesh2, Mesh3, Mesh4 and Mesh5; are shown in figure 3.5, figure 3.6, figure 3.7, figure 3.8 and figure 3.9, respectively. The meshes

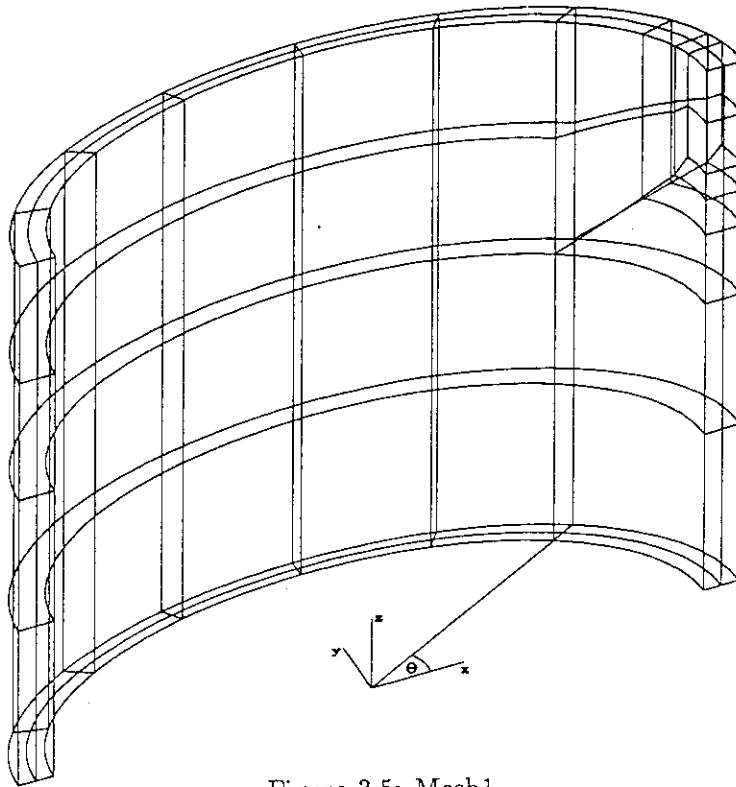


Figure 3.5: Mesh1

have been designed such that a large concentration of elements exist at the location of the hot spot and in its immediate vicinity. All the meshes are composed of eight noded isoparametric surface elements. The total number of elements for Mesh1, Mesh2, Mesh3, Mesh4 and Mesh5 are 130, 178, 186, 208 and 408, respectively. The corresponding degrees of freedom (DOF) is 1176, 1608, 1680, 1878 and 3678, respectively. Mesh2 is obtained from Mesh1 by dividing it once through the hot spot in the z -direction and by dividing the thickness of the pipe into three layers of elements; Mesh1 contains two layers of elements. The only difference between Mesh1 and Mesh3 is that for Mesh3 the thickness of the pipe is divided into four layers of elements. Mesh4 is very similar to Mesh2, the only change here is that Mesh4 has an extra layer of elements in the thickness direction. Mesh5 can be obtained from Mesh4 by dividing the hot spot twice in the z -direction and three times in the θ -direction. Additional subdivisions are also introduced in Mesh5 to decrease the overall size of adjacent element to element ratios, see figure 3.9.

Over each nodal point of the mesh, boundary conditions in terms of known quantities such as temperature, heat flux, displacements and tractions were prescribed according to figure 3.3. The unknown nodal temperature, heat flux, displacements and tractions were calculated using the BEM code described in § 2.2.3. In this convergence analysis the physical interpretation of the displacement solutions obtained will not be discussed. A full explanation of the solution behaviour will be presented in § 4.1, where more realistic dimensions of the hot leg together with more accurate boundary conditions are chosen in the analysis.

In terms of cylindrical polar coordinates (r, θ, z) , where $r^2 = x^2 + y^2$ and θ is measured in the x - y plane relative to the x -axis, the radial and tangential displacements U_r and U_θ respectively are shown plotted in figure 3.10, figure 3.11, figure 3.12 and figure 3.13. For the

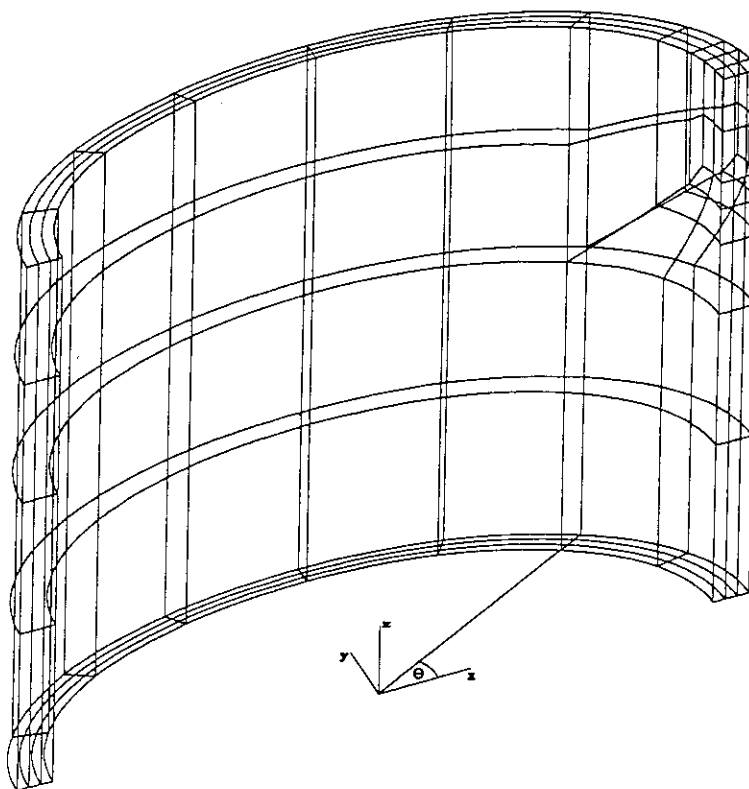


Figure 3.6: Mesh2

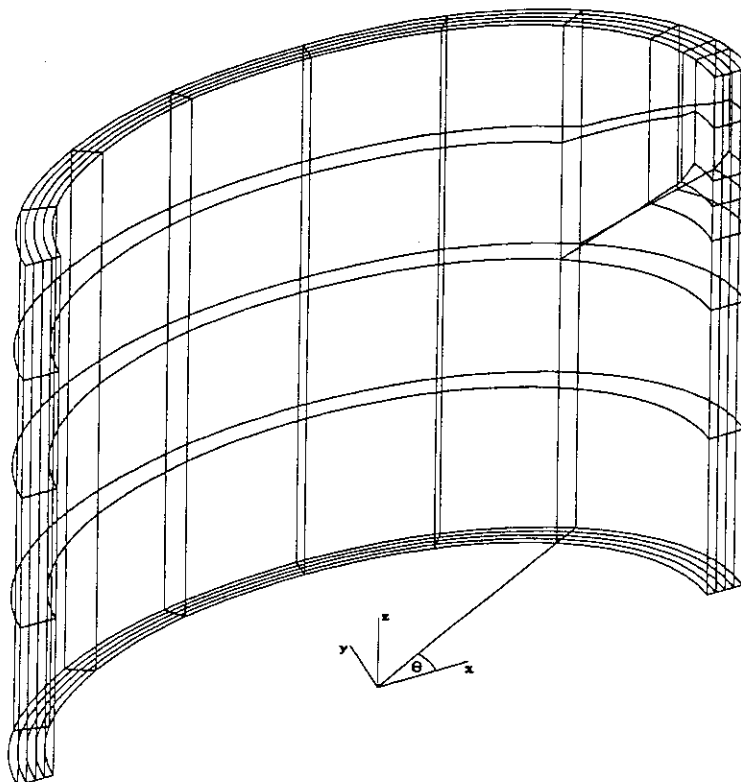


Figure 3.7: Mesh3

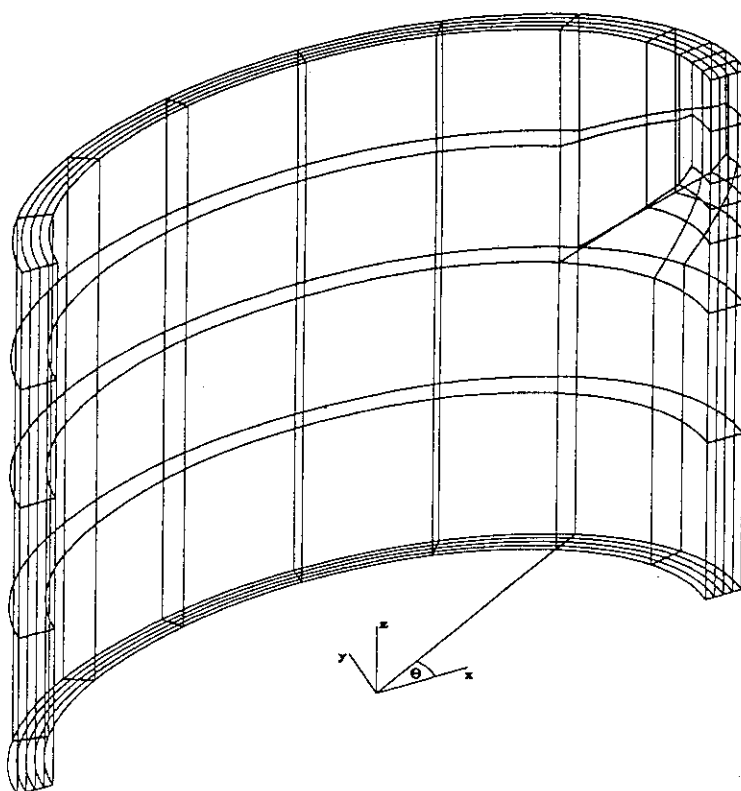


Figure 3.8: Mesh4

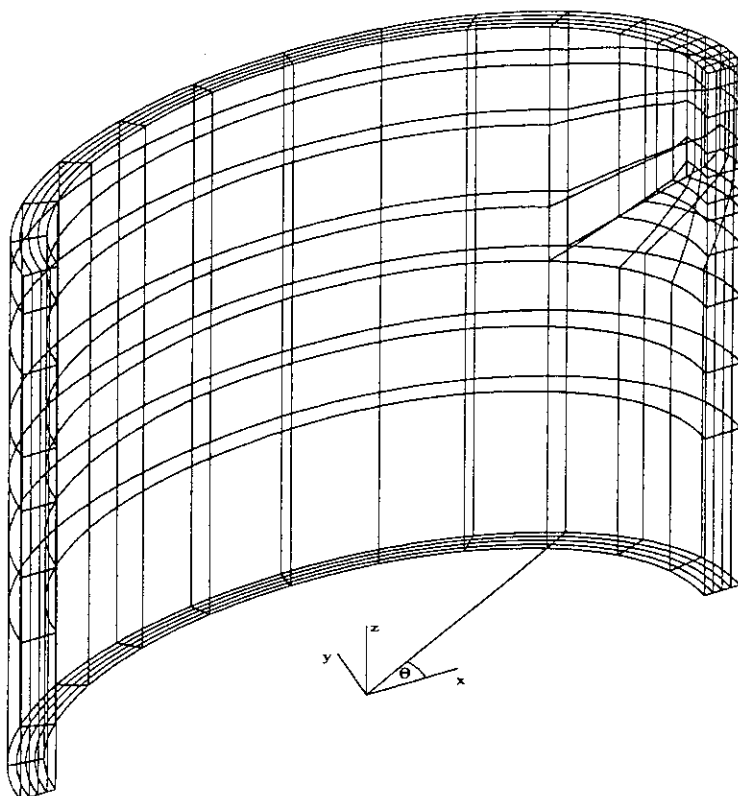


Figure 3.9: Mesh5

benefit of the reader, θ is plotted both in radians and in degrees in these figures. In figure 3.10, and figure 3.11 the U_r variation within the range $0 \leq \theta \leq \pi$ is plotted along the inner surface of the pipe at elevations of $z = 1.0m$ and $z = 0m$. The U_θ variation in figure 3.12 and figure 3.13 is presented in the same range and for the same z elevations.

The U_r and U_θ variations at elevations of $z = 1.0m$ and $z = 0.0m$ show that the presence of the hot spot plays a central role in determining the structural response of the pipe. Solutions obtained using Mesh1 and Mesh3 deviate considerably from those given by the other meshes. This can be attributed to the refinement of the mesh which is restricted only across the thickness of the pipe. Generally, these two meshes contain relatively large adjacent element to element ratios. The maximum difference between the solutions (both U_r and U_θ) obtained for Mesh1 and Mesh3 over the entire range of θ and for both z elevations is 5%. Mesh refinement restricted across the thickness of the pipe only, produces solutions with similar trends. These solutions deviate considerably from the other solutions suggesting that increasing degrees of freedom in this manner cannot guarantee convergence.

Comparison of the solutions obtained for Mesh3 and Mesh4 show that the introduction in Mesh4 of the single subdivision through the hot spot in the z -direction decreases (see figure 3.10) U_r by 26% at $\theta = 0^\circ$. A similar decrease in U_r is shown in figure 3.11 at the same θ location. Generally, this subdivision has a profound effect on the global variation of the displacement components. For Mesh2, this subdivision generates a consistent pattern of results that follow the same trend as the results obtained using Mesh4 and Mesh5.

The U_r solutions (see figure 3.10 and figure 3.11) for Mesh2 and Mesh4 are in good agreement for $\theta \leq 55^\circ$. Within this θ range the two meshes are very similar and the addition of another layer of elements (as in Mesh4) across the thickness direction does not change the ratio of adjacent elements in this region considerably. For $\theta > 55^\circ$ the two solutions in figure 3.10 and figure 3.11 show a maximum difference of 8%. For U_θ (see figure 3.12 and figure 3.13) these two meshes produce similar solution patterns as for U_r , thus in the vicinity of the hot spot the solutions tend to be similar.

The final solution obtained for Mesh5 (largest degrees of freedom used) follows the same trend as Mesh4. For $\theta \leq 20^\circ$ the maximum difference in all the solutions for Mesh4 and Mesh5 is 7%. In the case of $z = 0.0m$ both U_r and U_θ are in good agreement over the entire range of θ considered for both meshes.

In general this study shows that increase in the number of elements (*i.e.*, degrees of freedom) in the model gives rise to solutions that will eventually converge. The distribution of the degrees of freedom in a particular mesh determines the behaviour of the solution and its convergence characteristics. Localised increase in the degrees of freedom (*e.g.*, vicinity of the hot spot) gives rise to localised convergence of the solution in that region. Overall solution convergence requires overall mesh refinement. In this case the refined mesh must be able to model the boundary conditions correctly everywhere, whenever the boundary conditions change rapidly the mesh density must also be increased in that region. The criteria for convergence is not clear due to the complex interaction between the different distribution of elements and their sizes.

3.3 TTR Modelling

In the analysis presented so far the dimensions of the TTR have been fixed. Further, only a linear temperature variation has been prescribed over this region. The question of the solution dependence if any, on the dimensions of the TTR and the variation of different temperature boundary conditions must also be addressed. As regards this, attention is concentrated on Mesh5 (figure 3.9) and solutions obtained for different sizes of the TTR. Finally, solutions are presented for the case when a step change in temperature is prescribed across the TTR in Mesh4.

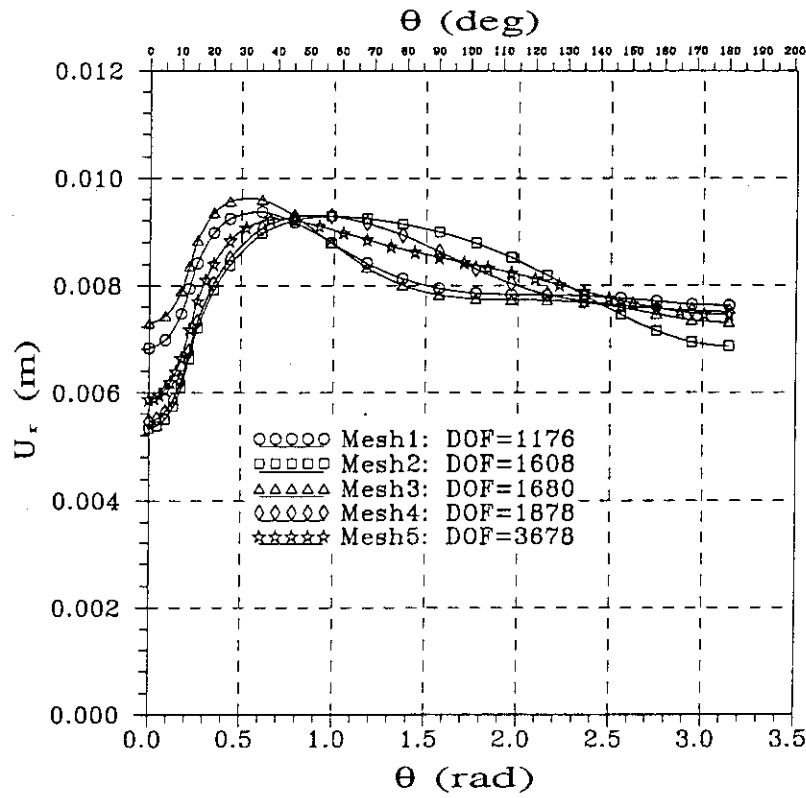


Figure 3.10: U_r : Inner surface, $z = 1.0m$.

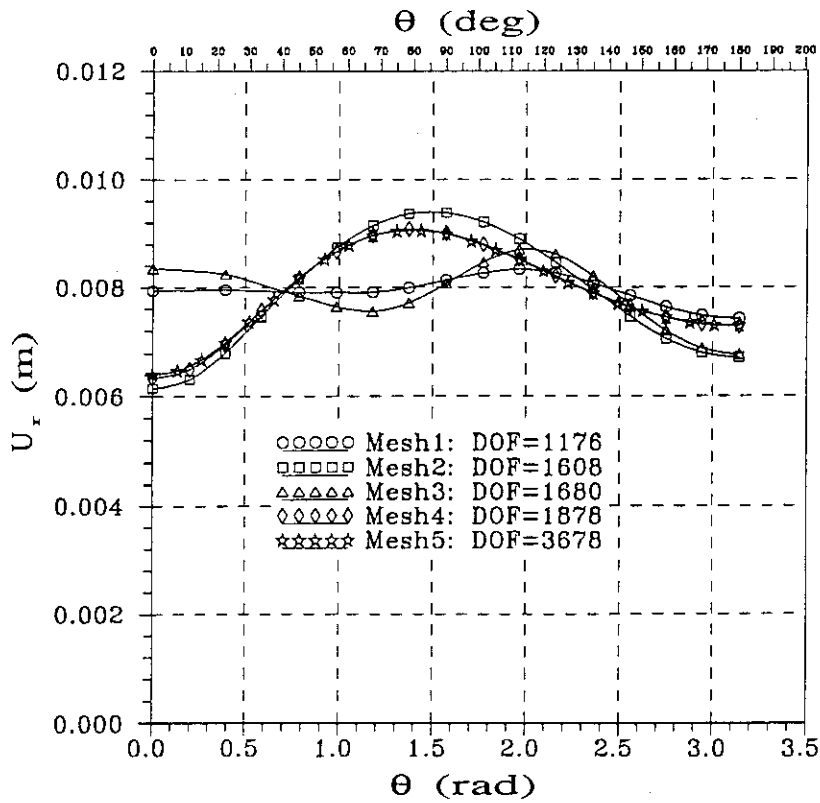


Figure 3.11: U_r : Inner surface, $z = 0.0m$.

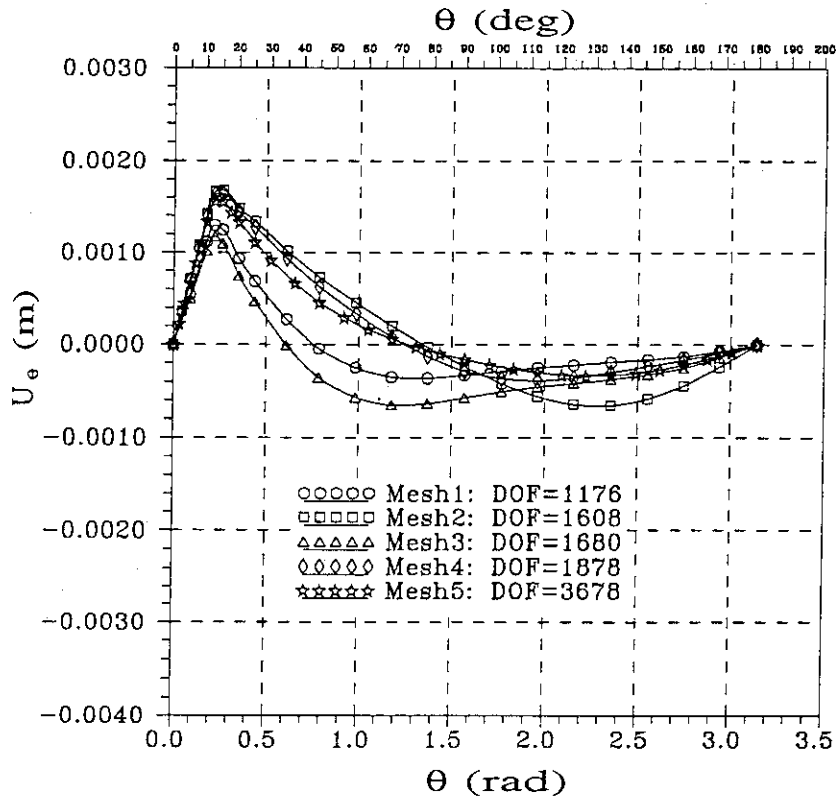


Figure 3.12: U_θ : Inner surface, $z = 1.0m$.

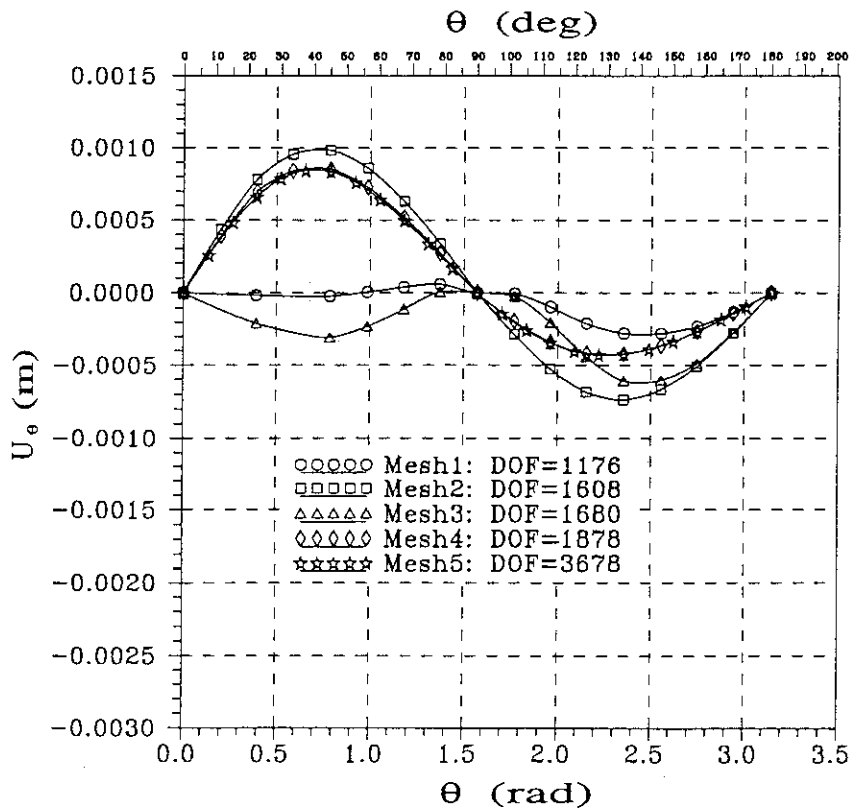


Figure 3.13: U_θ : Inner surface, $z = 0.0m$.

3.3.1 Size Dependence

To determine the solution dependence on the size of the TTR, the ratio S_1/S , as defined in figure 3.4 for Mesh5 was varied. This variation was attained by changing the arc length S_1 (defined by the angle $\gamma/4$ in figure 3.4) while maintaining S constant. Ratios of S_1/S chosen for the analysis were 0.5, 0.25 and 0.125. For each ratio a linear temperature variation was prescribed across the TTR. In changing the arc length S_1 , the mesh distribution adjacent to the TTR, defined by the region $0.55 < z < 0.9$, $\theta < 45^\circ$ and $0.55 \leq r \leq 0.61$ must be slightly modified. The mesh distribution on the remaining part of the pipe and hot spot surface was not altered. For all the different S_1/S ratios employed in the analysis, the distribution of elements and degrees of freedom outside the TTR were essentially the same as for Mesh5.

The radial and tangential displacements U_r and U_θ as obtained for different S_1/S ratios is plotted in figure 3.14 and figure 3.15. These displacement solutions are along the inner surface,

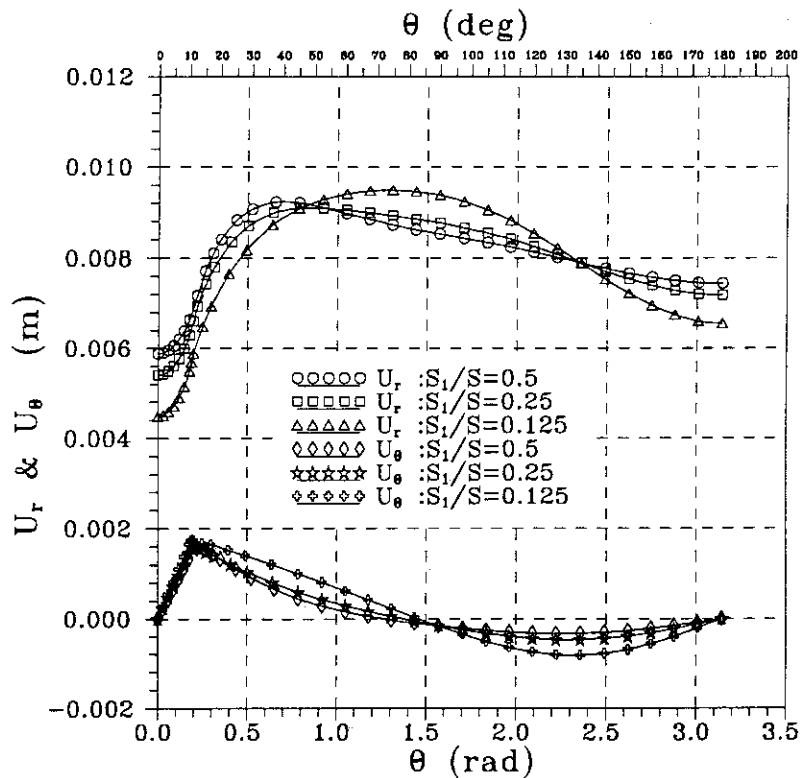


Figure 3.14: TTR size variation: U_r and U_θ at $z = 1.0m$ along inner surface.

at $z = 1.0m$ and $z = 0.0m$ within the range $0.0^\circ \leq \theta \leq 180^\circ$. The results show that for S_1/S ratios of 0.5 and 0.25, all the solutions presented in figure 3.14 and figure 3.15, for both U_r and U_θ , have a maximum difference of 8% over the entire range of θ considered. This maximum difference occurs for U_r at $\theta = 0^\circ$, see figure 3.14. For $\theta > 0^\circ$ the maximum difference in the two solutions is 4%. For S_1/S ratios of 0.5 and 0.25 the displacement solutions at $z = 0m$ are in good agreement, see figure 3.15. The maximum difference between these solutions over the entire range of θ is 2%.

The solutions obtained for S_1/S ratios of 0.5 and 0.25 deviate considerable from the solution obtained when $S_1/S = 0.125$. This deviation is most likely due to the fact that as the ratio S_1/S decreases the elements across the TTR become extremely thin. Thus, a too small value of S_1/S can lead to solutions that become unstable. An optimum value for S_1/S for all problems would be difficult to establish. In the present analysis all the solutions obtained for $0.25 \leq S_1/S \leq 0.5$ are within 8% of each other.

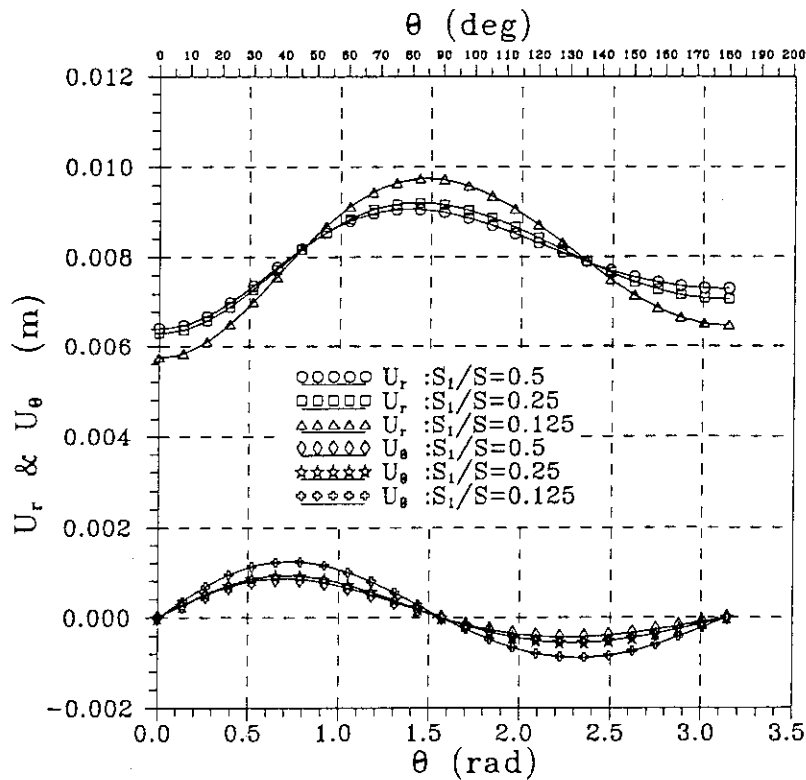


Figure 3.15: TTR size variation: U_r and U_θ at $z = 0.0m$ along inner surface.

3.3.2 Step Change in Temperature

In the temperature transition region (TTR) the prescribed temperature boundary condition can have any variation. So far the analysis has only concentrated on a linear variation of temperature over this region since this is the easiest to prescribe. Theoretically, any variation can be prescribed but from a BEM numerical point of view this is not strictly correct. Any prescribed variation that can be simulated by the interpolation functions employed in the BEM is a valid temperature boundary condition. In the BEM code quadratic interpolation functions are used, thus the variation of prescribed temperature allowed must be such that it can be represented by a quadratic function defined over the three nodes along the side of the element. Invalid solutions can be obtained if a temperature is prescribed over the TTR which cannot be represented by a quadratic function.

In order to get a clear understanding of this, consider the situation when a step change in temperature across the TTR is introduced into the modelling. This step change in temperature can be attained by prescribing temperature T_h over nodes 1, 2 and 3 in figure 3.4. Over the remaining nodes of the element prescribe temperature T_i . Clearly, this jump in temperature at nodes 1, 2 and 3 cannot be modelled using quadratic interpolation functions along the sides of the element defined by nodes 5, 4, 3 and 7, 8, 1 (see figure 3.4).

Two solutions were obtained using Mesh4. The first solution was obtained by prescribing a linear temperature variation across the TTR. The second solution was obtained by prescribing a step change in temperature across the TTR. For both solutions only the temperature variation across the TTR was changed, the remaining boundary conditions were kept the same. Results in terms of the hot leg deformation for the linear and step temperature variation are shown in figure 3.16 and figure 3.17. The results are only presented for the cross-section of the pipe at an elevation of $z = 1.0m$, where z is defined in figure 3.8. In figure 3.16 and figure 3.17 the original undeformed (*i.e.*, continuous line) mesh and deformed (*i.e.*, dashed line) are shown simultaneously. The deformed meshes have been magnified by 15 times. This analysis clearly

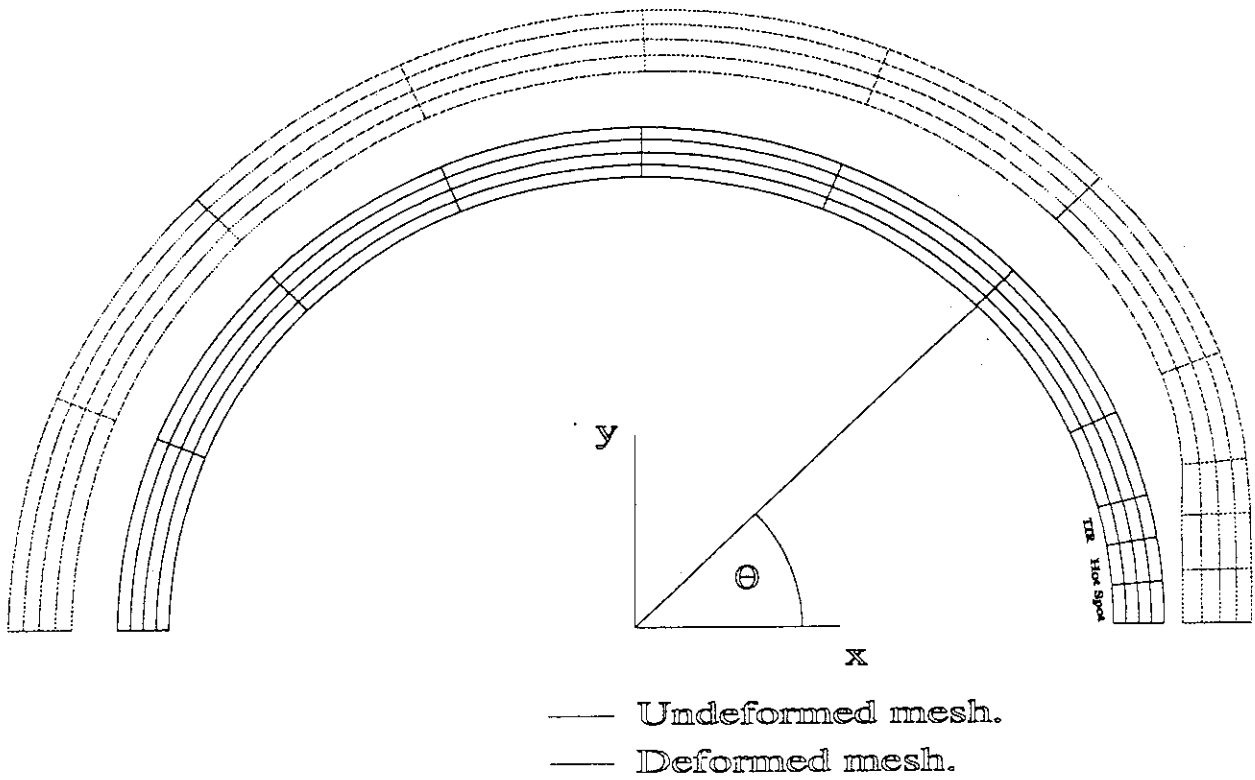


Figure 3.16: Deformation at $z = 1.0m$ for Mesh4; Linear temperature.

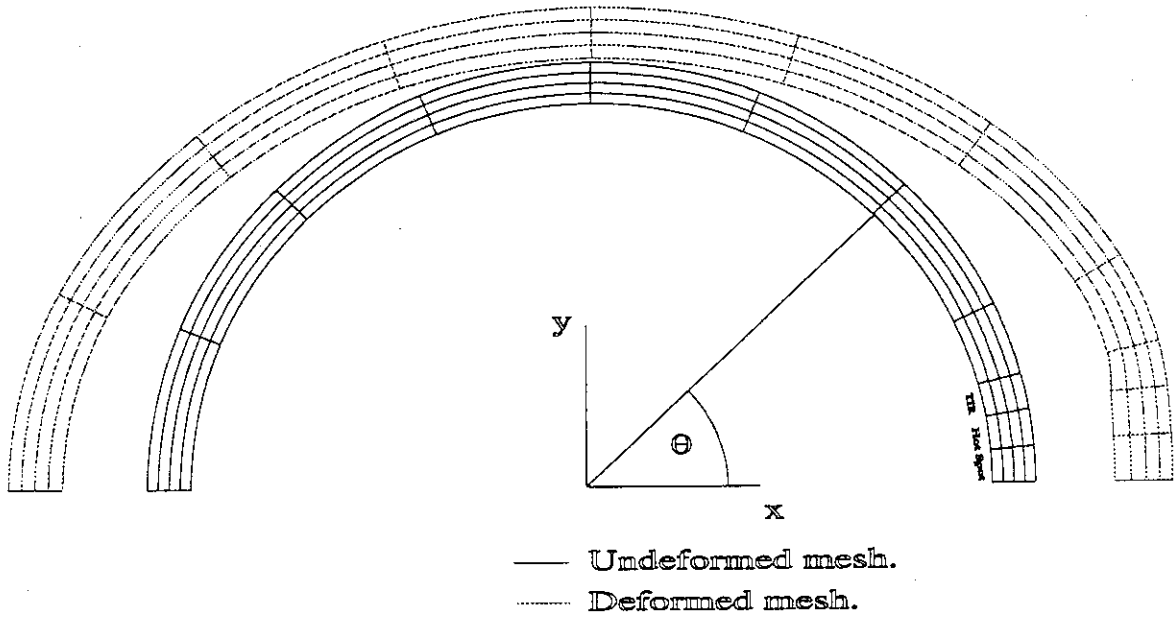


Figure 3.17: Deformation at $z = 1.0m$ for Mesh4; Step temperature.

reveals that the solution obtained (see figure 3.17) using a step temperature variation across the TTR is unreasonable. The large radial deformation obtained at $\theta = 180^\circ$, and the smallest radial expansion occurring at $\theta = 90^\circ$ cannot be accounted for. This deformation behaviour can only be attributed to the fact that the quadratic interpolation functions are incapable of representing a step variation in the temperature boundary conditions across the TTR. Increasing the degrees of freedom in the mesh without altering the size of the TTR, did not change the general behaviour of the solutions.

In contrast, for the linear temperature variation across the TTR the deformation obtained (see figure 3.16) is more in line with that expected from intuitive arguments. At large distances from the location of the hot spot it is reasonable to expect the solution to be unaffected by the presence of the hot spot. On approaching the hot spot region one would expect the solution to be increasingly influenced by the presence of the hot spot. This behaviour is shown in figure 3.16. In the range $112.5^\circ \leq \theta \leq 180^\circ$ the pipe experiences a uniform radial expansion. Within the range $\theta \leq 112.5^\circ$ the deformation becomes influenced by the presence of the hot spot.

3.4 Conclusions

To verify the suitability of BEM to this class of problems, mesh convergence studies were performed on a pipe geometry containing a single hot spot. This analysis showed that solution convergence can be realised provided sufficiently large number of elements are employed and correct modelling of the temperature transition region (TTR) adjacent to the hot spot on the inner surface is done. The only viable temperature field across the TTR is that which can be represented by the interpolation functions employed in the BEM code. Further, the dimensions of the TTR are important, if it is too thin numerical instability may occur giving incorrect solutions.

Chapter 4

Numerical Solutions

The analysis conducted in Chapter 3 is based on an approximate geometry of the straight section of the hot leg. Further, the temperature boundary conditions employed are not very accurate since this data was not available at the time this study was conducted. This chapter comprises of two sections, the first concentrates on the straight section of the hot leg and the latter on the bend section. Exact geometrical dimensions of the hot leg are employed together with more realistic severe accident thermal boundary conditions in the analysis. For the straight section analysis solutions in terms of the displacements, strains and stresses are presented. In the bend analysis, both constant temperature and adiabatic boundary conditions (*i.e.*, zero heat flux) on the outer surface are considered. Here only the displacements and stresses are presented.

4.1 Hot Spot in Straight Section of Hot Leg

The geometry of the straight section of hot leg as depicted in figure 3.2 was chosen with inner radius r_i and outer radius r_o equal to $0.3683m$ and $0.4318m$, respectively. The hot spot geometry is defined such that $L_h = 0.2m$ and γ is chosen so that the hot spot forms a square patch. All other dimensions were the same as those employed in § 3.2. The inner wall, outer wall and hot spot temperatures were prescribed as $926^\circ C$, $150^\circ C$ and $1500^\circ C$ respectively. An internal pressure of $0.554MPa$ was also prescribed in the hot leg, the outer surface was traction free. These severe accident temperature and pressure values were calculated using the THALES-2 computer code [8]. The temperature transition region (TTR) was defined such that $S_1/S = 0.5$, see figure 3.4. A linear temperature variation was prescribed over this region. All the remaining boundary conditions were identical to those presented in § 3.2.

In this analysis only 1/4 of the problem is modelled. The mesh used is shown in figure 4.1 and contained 408 elements with 3678 degrees of freedom. The concentration of elements in the vicinity of the hot spot can be seen more clearly in the mesh with the hidden lines removed. The mesh for the analysis is designed bearing in mind that as the distance increases from the hot spot the solution should become less sensitive to the presence of the hot spot.

The radial and tangential displacement variation (*i.e.*, U_r and U_θ) at elevations of $z = 1.0m$ and $z = 0.0m$ on the inner surface of the hot leg (*i.e.*, $r = r_i$) are shown in figure 4.2. Also shown in figure 4.2 are the solutions obtained at the same locations for an auxiliary problem, in which a hot leg without a hot spot is analysed. In this problem, details of which can be found in § A.1, the geometrical dimensions are identical to those of the hot leg containing a hot spot. Without the presence of the hot spot the problem possesses another plane of symmetry. Thus, in the auxiliary problem only 1/8 of the model needs to be discretised and solved with appropriate boundary conditions on the planes of symmetry. A convergence analysis conducted on the auxiliary problem (see § A.1) show that converged solutions can be obtained with a relative coarse mesh containing 77 elements with 654 degrees of freedom. The solution convergence was

Complete mesh.

Mesh with hidden lines removed.

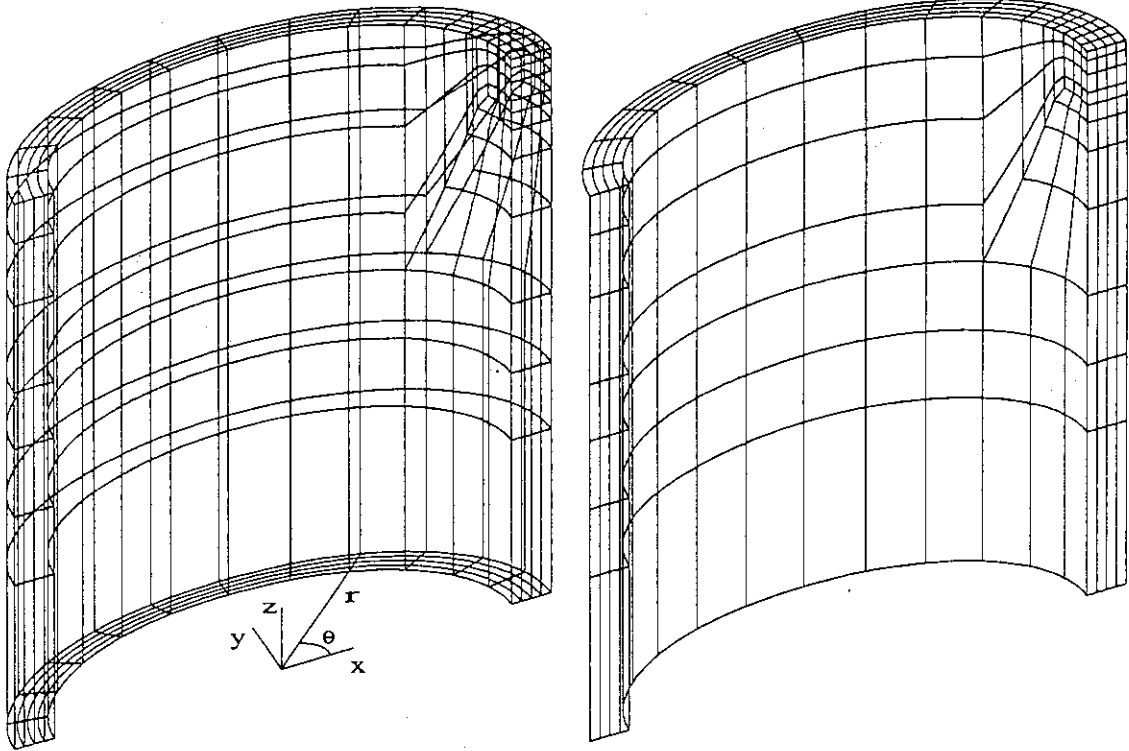


Figure 4.1: Mesh for 1/4 analysis of problem

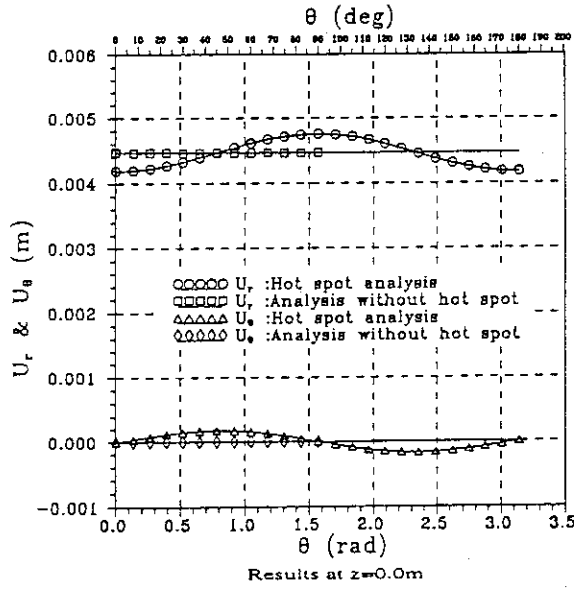
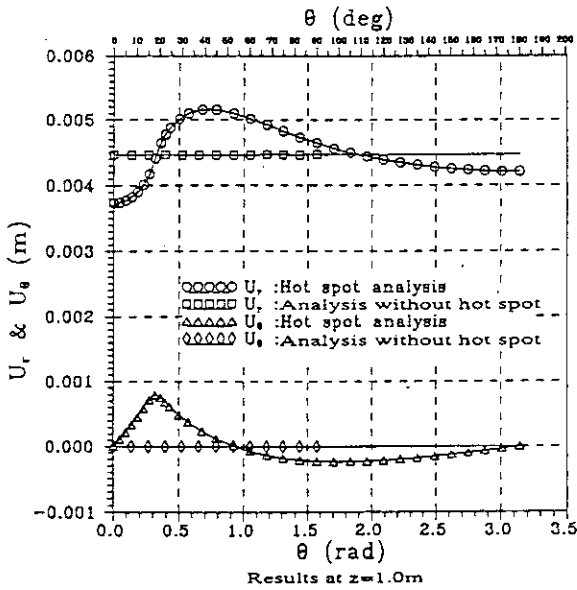


Figure 4.2: Comparison of displacement variations

compared with an analytical solution as obtained in § A.1. This auxiliary problem represents the hot leg response prior to the fission product deposition. Therefore, the auxiliary problem allows the hot leg response to be compared before and after the fission product deposition.

Without the presence of the hot spot the inner surface undergoes a uniform radial expansion of 0.00446m, see figure 4.2. The tangential displacements for this situation is zero as expected. When the hot spot is present in the analysis the inner surface no longer experiences a uniform radial expansion. Further, tangential displacements are also generated. At $z = 1.0m$ the minimum and maximum variation in U_r (see figure 4.2) occurs at $\theta = 0^\circ$ and $\theta \approx 40^\circ$, respectively. For $\theta > 160^\circ$ the U_r variation is approaching a constant value. The difference between the U_r solution (at $z = 1.0m$) obtained when the hot spot is present and not present in the analysis at $\theta = 0^\circ$, $\theta \approx 40^\circ$ and $\theta = 180^\circ$ is 16%, -17% and 6%, respectively. For the tangential displacement U_θ at $z = 1.0m$ the maximum difference in the two solutions is 0.08% and occurs at $\theta \approx 20^\circ$. Further, U_θ is positive in the range $0^\circ \leq \theta \leq 52^\circ$ and negative in the range $52^\circ \leq \theta < 180^\circ$.

At $z = 0.0m$ the U_r variation over the entire range of θ shows less deviation from the solution obtained using no hot spot. The maximum difference in the two solutions is 6%. The U_r variation is symmetrical about $\theta = 90^\circ$. With regard to the tangential displacement at this location, the maximum difference in the two solutions is only 0.02%. This solution is also symmetrical about $\theta = 90^\circ$.

In the hot spot analysis a constraint was imposed at the point $(0, r_i, 0)$ such that this point could not move in the x -direction. This constraint is necessary to ensure that no rotation and translation of the hot leg takes place. This explains why the tangential displacement is zero at $\theta = 90^\circ$ and $z = 0.0m$ in figure 4.2. The results also show that while at $z = 0.0m$ the tangential displacement is zero, at $z = 1.0m$ it has a value of $-0.0002m$. Thus, the y - z plane passing through the points $(0, r_i, 0)$ and $(0, r_i, 1.0)$ does not remain vertical indicating movement of the hot leg material towards the hot spot with increasing z elevation.

The variation of U_r and U_θ as a function of z and θ on the inner surface ($r = r_i$) is shown in figure 4.3 and figure 4.4. The grid showing the variation of U_r and U_θ in these surface plots does not represent the boundary element mesh discretisation used on the inner surface. This grid is generated using a plotting program. Large radial and tangential deformations dominate in the vicinity of the hot spot. These deformations result from the presence of the applied axial constraint and the thermal boundary conditions. The solutions at $z = 1.0m$ and $z = 0.0m$ for all θ in figure 4.3 and figure 4.4 are identical to those presented in figure 4.2. Generally, for U_r and U_θ the deformation is more severe at $z = 1.0m$ than at $z = 0.0m$. This behaviour shows that as the distance increases from the hot spot the solution becomes less sensitive to the presence of the hot spot.

In the analysis, applicability of the plane strain condition needs to be clarified. If plane strain condition prevails, one is justified in assuming that the axial displacement U_z is zero everywhere in the section of hot leg under consideration. The imposed axial constraints at elevations of $z = 0.0m$ and $z = 1.0m$ ensure that U_z is zero at these two positions. At the location of the hot spot, close to the axial constraint at $z = 1.0m$, U_z will also be established due to local expansion of the material in the z -direction, obviously this local axial deformation will decrease to zero at $z = 1.0m$. Far from the hot spot location the prescribed thermal boundary conditions are independent of z , thus U_z will be zero. This variation of U_z at $r = r_i$ can be seen in the surface and contour plots presented in figure 4.5 and figure 4.6, respectively. The surface plot shows that the axial displacement is zero everywhere except in the hot spot region. Thus, outside the hot spot region it is reasonable to assume that the plane strain condition applies since the prescribed loads (mechanical and thermal) are independent of z . At $z = 0.875m$ and $\theta \leq 7^\circ$ (see figure 4.6), U_z peaks to a value of $-0.00052m$. This peak value is the same order of magnitude as the tangential displacement U_θ (see figure 4.2 and figure 4.4) and thus cannot be

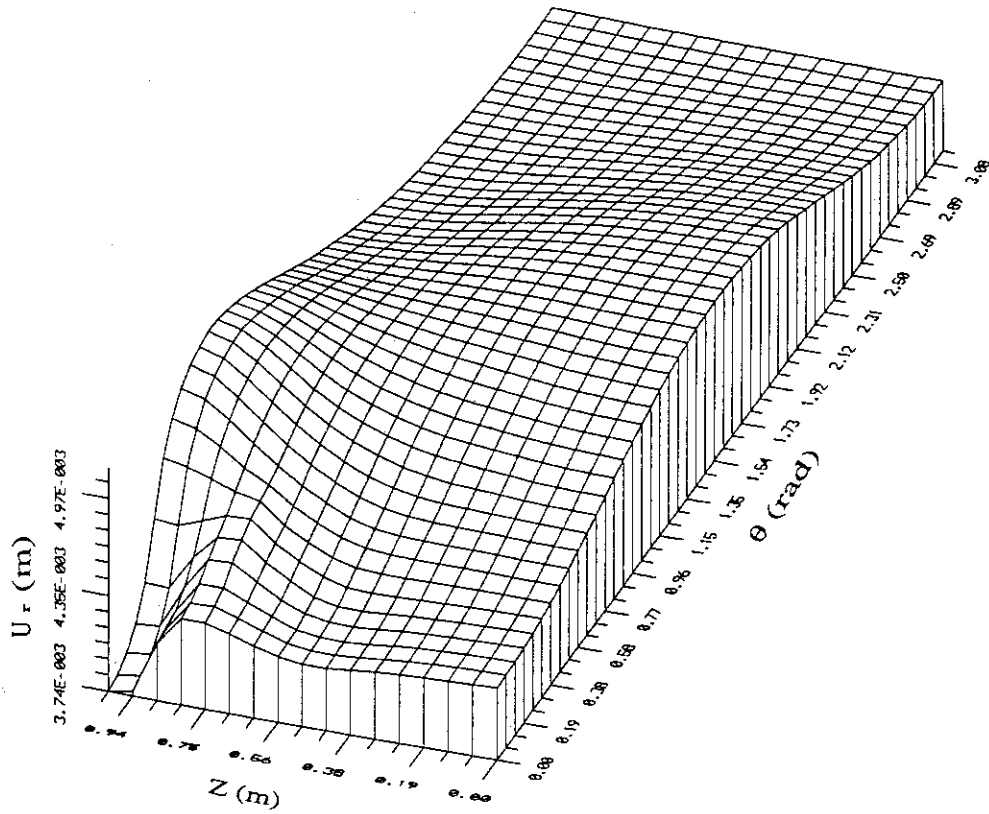


Figure 4.3: U_r variation on inner surface

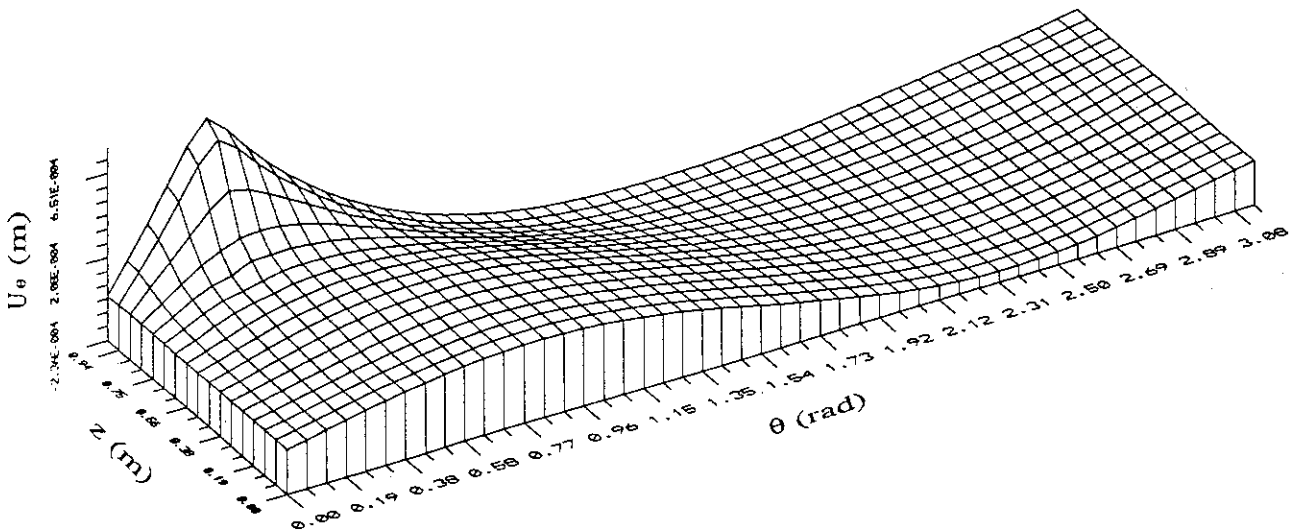


Figure 4.4: U_θ variation on inner surface

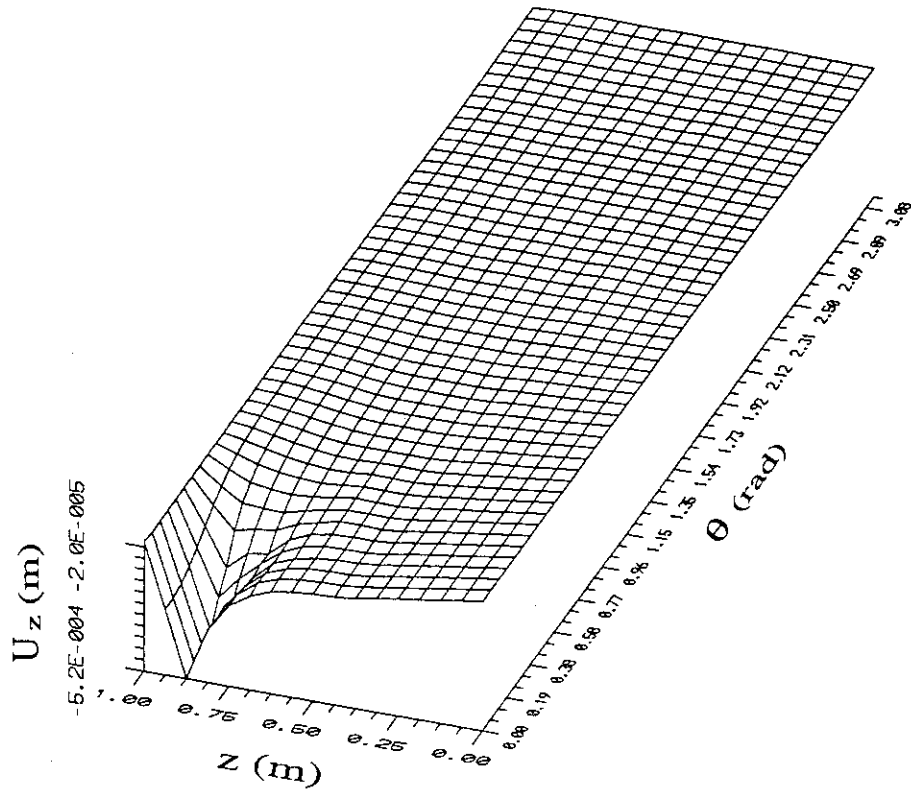


Figure 4.5: U_z variation on inner surface

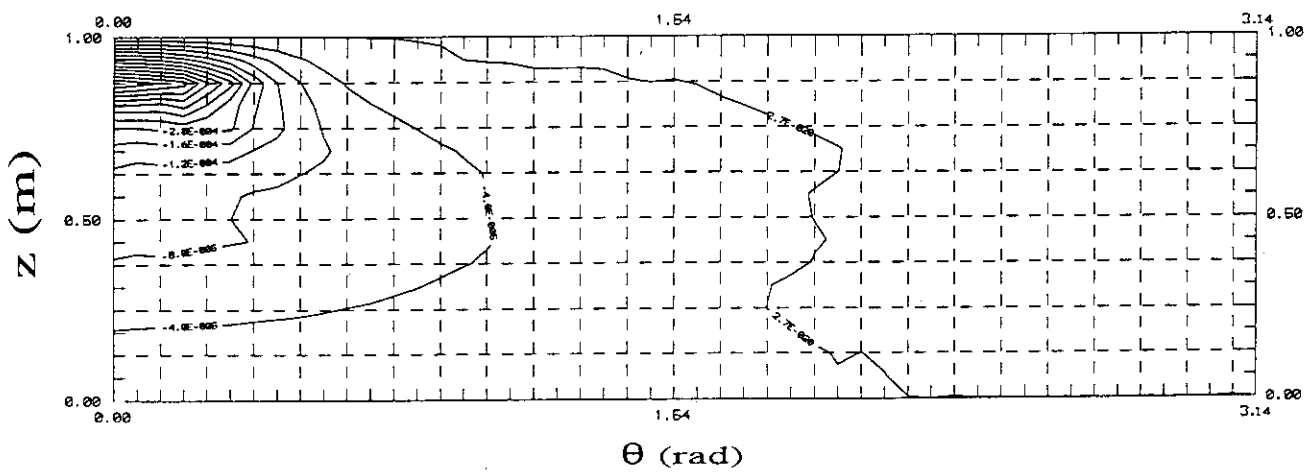


Figure 4.6: Contour plot of U_z on inner surface

ignored. All U_z variations at the hot spot location are negative showing that the direction of the material expansion is in the sense of the negative z -axis. This expansion arises as a consequence of the axial constraint at $z = 1.0m$ and the thermal boundary conditions. A further consequence of this non zero U_z variation is that the strain ϵ_{zz} will not be zero in the vicinity of the hot spot. Thus, only a three-dimensional analysis can adequately explain the behaviour of the hot leg at the site of the hot spot. Assumptions of plane strain or plane stress are not applicable in this region.

A global view of the undeformed (*i.e.*, solid line) and deformed (*i.e.*, dotted line) hot leg is presented in figure 4.7. The undeformed mesh corresponds to that shown in figure 4.1. Two views are presented in figure 4.7, the first view shows the complete mesh used in the modelling before and after the analysis. In the latter view the mesh distribution on the outer surface (*i.e.*, $r = r_o$) and on the x - y plane at $z = 0.0m$ is removed. The deformation is magnified by 80%. This clearly shows the dominating effects of the hot spot on the hot leg. Generally, there is an outward radial expansion of the hot leg everywhere as expected. Further, the higher inner

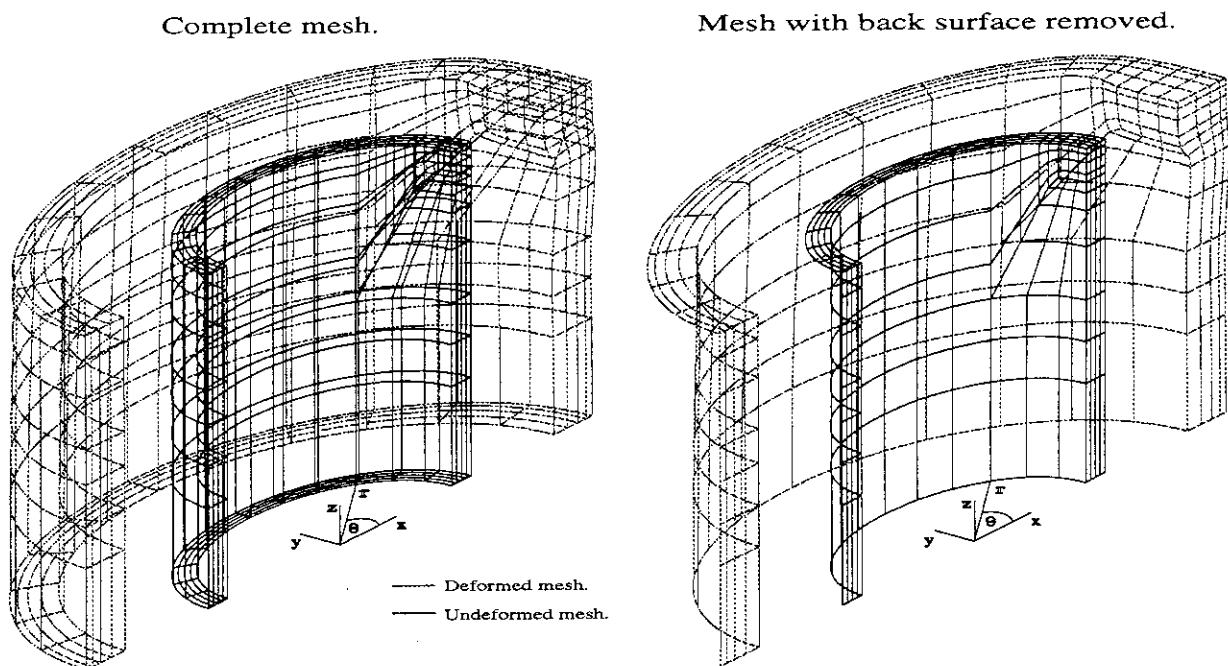


Figure 4.7: Hot leg deformation

prescribed temperature ($T_i \gg T_o$) produces a larger expansion on the inner surface relative to the outer surface. This non uniform, across the thickness expansion can be realised by comparing the element distributions across the thickness between the undeformed and deformed meshes. In the deformed mesh the width of the elements become larger as one moves across the thickness from the outer to the inner surface indicating that the inner and outer surfaces respond differently. This variation across the thickness would not be apparent if shell elements were employed since these elements generate an average value of the field quantities across the thickness.

In order to explain the deformation observed it is necessary to consider the situation when expansion of the hot leg in the axial direction at $z = 1.0m$ is not constrained. In such a case one would expect the axial deformation U_z to have a maximum variation at $\theta = 0^\circ$ due to the presence of the hot spot. This axial deformation would gradually decrease to a minimum value at $\theta = 180^\circ$. Also, since the temperature variation is such that $T_h \gg T_i \gg T_o$ one would also expect U_z at $r = r_i$ to be higher than U_z at $r = r_o$. This effect would be most predominate

in the hot spot location spot.

In the analysis conducted an axial constraint ($U_z = 0$) is prescribed at $z = 1.0m$ which prevents the free expansion described above. Thus, the free end expansion must be redistributed in the unconstrained directions (i.e., radially and tangentially) so that the axial expansion is zero at $z = 1.0$. Hence, large radial and tangential deformations would be expected in the vicinity of the hot spot relative to regions far from it. The swelling of the inner surface at the location of the hot spot and the associated bending obtained in its vicinity are a direct consequence of the axial constraint.

In another study the internal pressure was removed and the analysis repeated. This showed that the contribution the internal pressure makes to the hot leg deformation is negligible (less than 1%). Thus, thermal boundary conditions in conjunction with the constraints are the controlling factors in this problem.

To get a better understanding of the hot leg response the strains and stresses must also be considered. Only the surface variation of these quantities will be presented. Concentrating on the strains first, which are plotted on the inner and outer surfaces in figures 4.8-4.13 and figures 4.14-4.19, respectively, as functions of θ and z . Generally, the pattern of the strains on

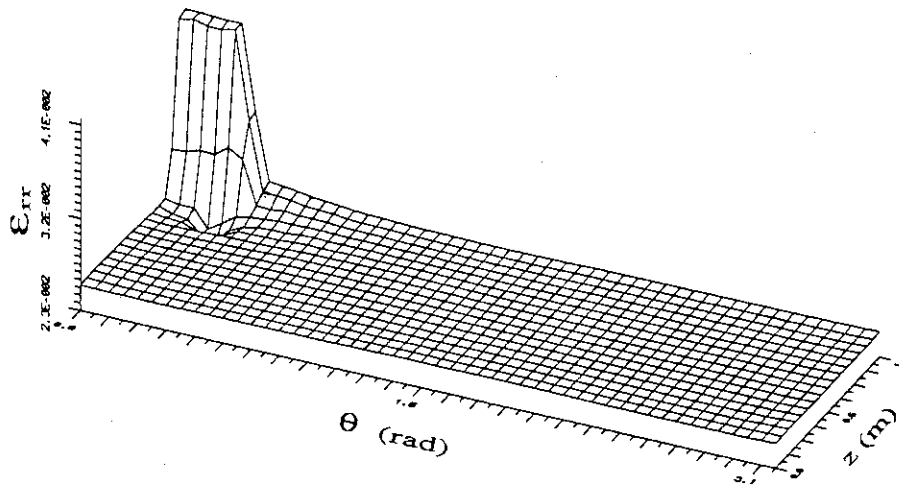


Figure 4.8: ϵ_{rr} on inner surface

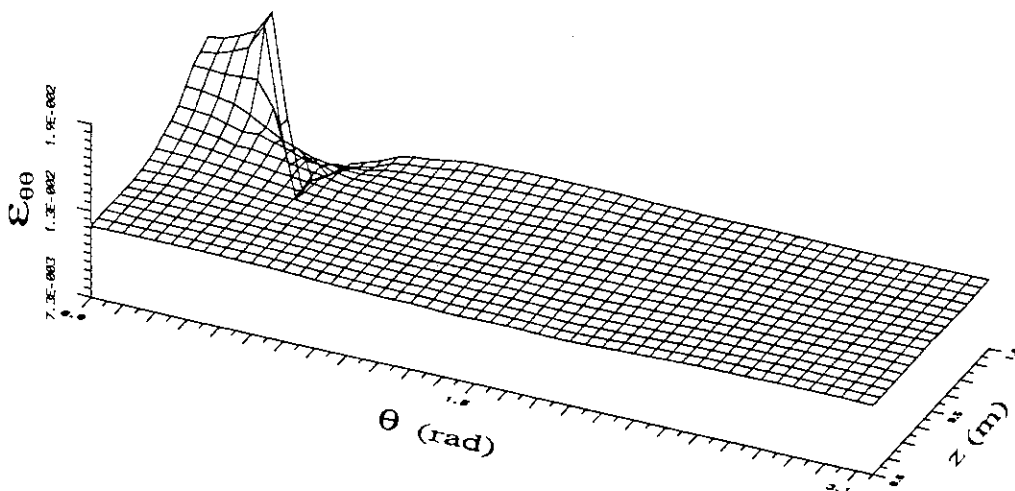


Figure 4.9: $\epsilon_{\theta\theta}$ on inner surface

the inner surface is that the radial strains ϵ_{rr} and the tangential strains $\epsilon_{\theta\theta}$ have the largest magnitudes, with $\epsilon_{rr} > \epsilon_{\theta\theta}$ everywhere on the inner surface. Both these strains are tensile. Outside the hot spot region ϵ_{rr} has a constant value of 0.0253. At the hot spot location ϵ_{rr}

increases to a value of 0.041. This constitutes to approximately 62% increase in ϵ_{rr} due to the presence of the hot spot. The $\epsilon_{\theta\theta}$ variation (see figure 4.9) along the elevation $z = 1.0m$ has a value of 0.016 at $\theta = 0^\circ$. The variation attains a maximum of 0.019 at $\theta = 15^\circ$. There is then a sharp fall to 0.0073, after which it increases to a steady value of 0.0119. This variation occurs

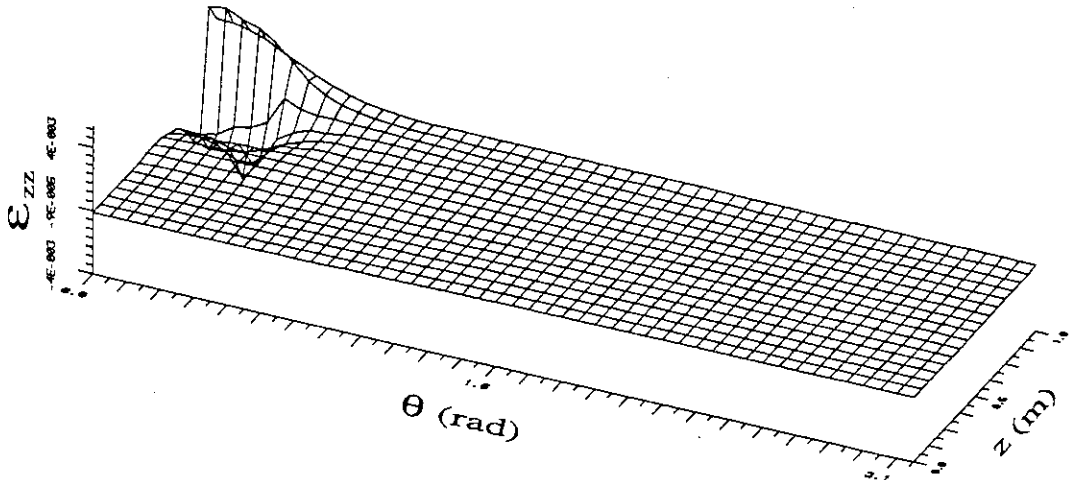


Figure 4.10: ϵ_{zz} on inner surface

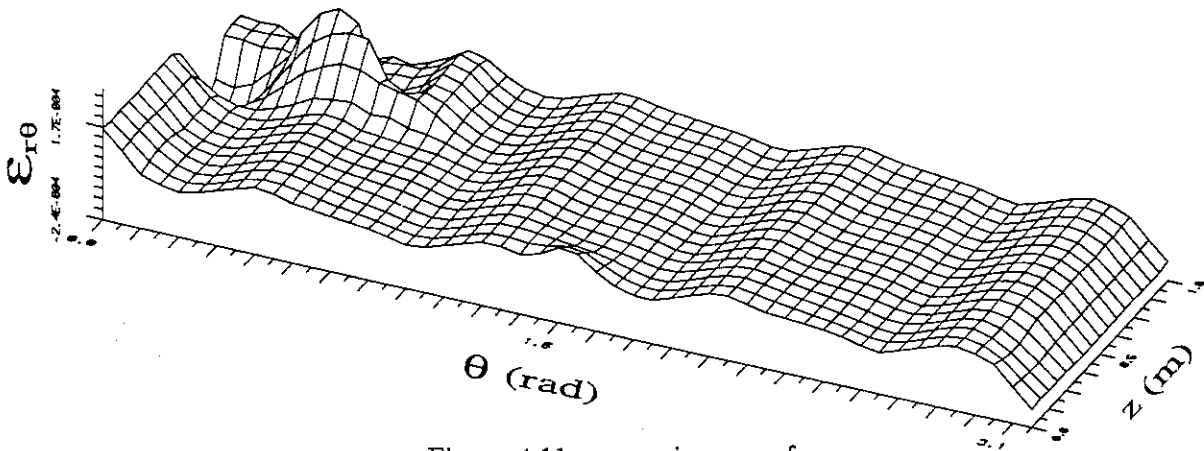


Figure 4.11: $\epsilon_{r\theta}$ on inner surface

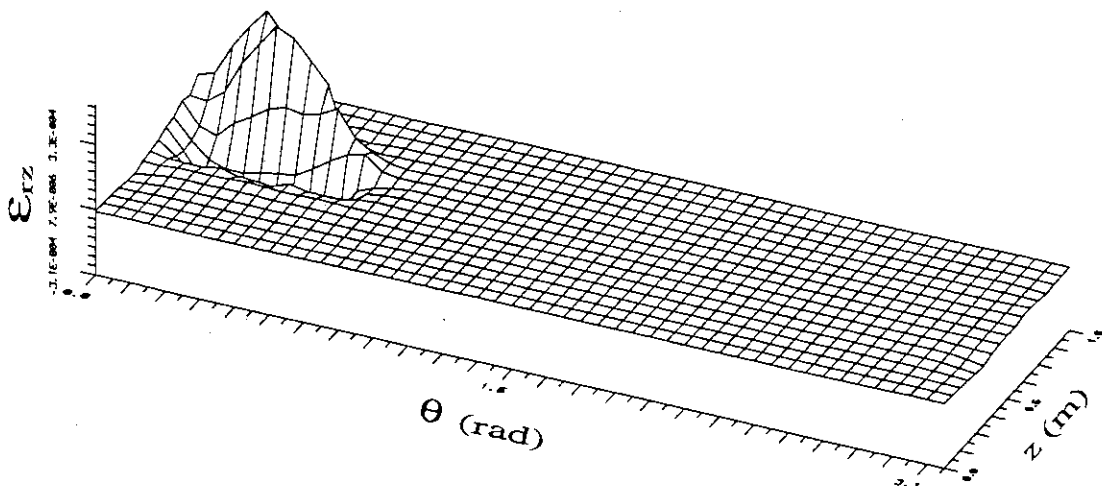


Figure 4.12: ϵ_{rz} on inner surface

due to the inward bending of the hot leg in the vicinity of the hot spot. The peak $\epsilon_{\theta\theta}$ variation

in figure 4.9 occurs at the same location as the peak tangential displacement U_θ in figure 4.4 as expected.

The axial strain ϵ_{zz} is essentially zero, see figure 4.10, except in the vicinity of the hot spot where it exhibits tensile and compressive properties. This variation can be obtained from consideration of the gradient of axial displacement U_z in figure 4.5. In the hot spot region ϵ_{zz} varies between ± 0.004 (i.e., an order of magnitude lower than ϵ_{rr} and $\epsilon_{\theta\theta}$). Far from the hot spot region conditions of plane strain are applicable.

The shear strains $\epsilon_{r\theta}$, ϵ_{rz} and $\epsilon_{\theta z}$ are shown in figure 4.11, figure 4.12 and figure 4.13, respectively. These variations can be deduced through consideration of the relationship (in

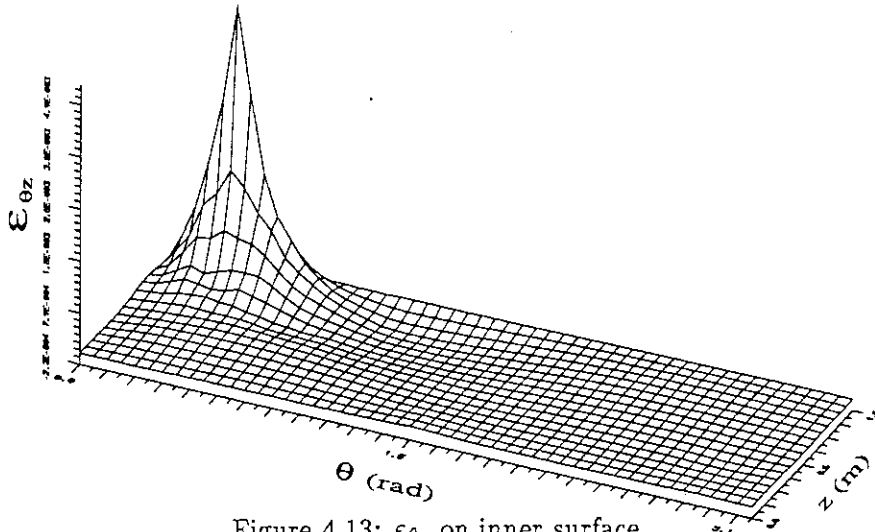


Figure 4.13: $\epsilon_{\theta z}$ on inner surface

cylindrical polar coordinates) connecting the derivatives of U_r, U_θ and U_z with respect to the spatial coordinates. The strain $\epsilon_{r\theta}$ is virtually unaffected by the presence of the hot spot. The ϵ_{rz} and $\epsilon_{\theta z}$ variations are zero except near the hot spot. This is as expected since U_z is non zero in the vicinity of the hot spot. The peak value of ϵ_{rz} is an order of magnitude lower than that of $\epsilon_{\theta z}$.

Considering the strains on the outer surface, ϵ_{rr} is zero everywhere except in the vicinity of the hot spot location where it is compressive, having a maximum value of -0.0021, see figure 4.14. Both $\epsilon_{\theta\theta}$ variations on the inner and outer surface are of the same order of mag-

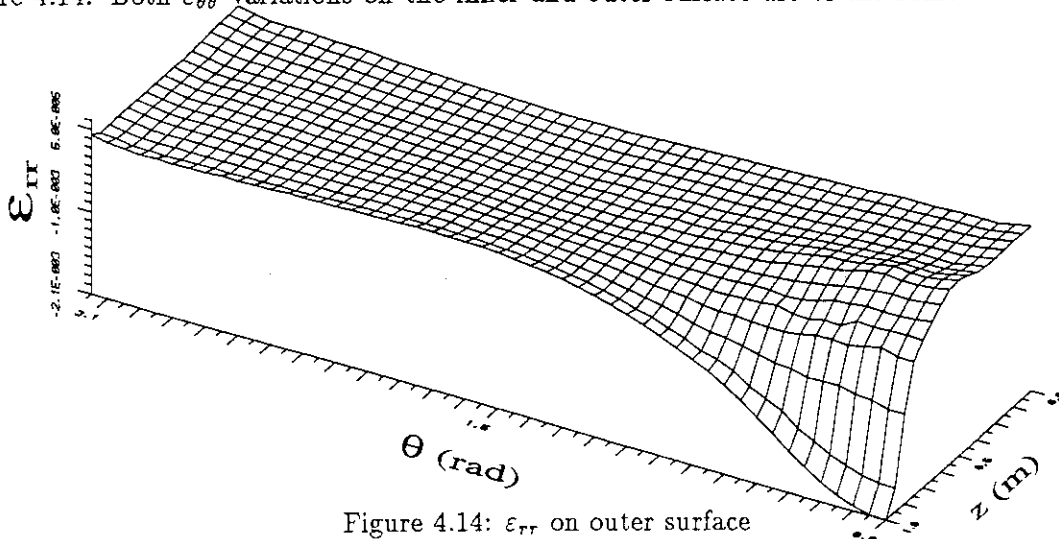


Figure 4.14: ϵ_{rr} on outer surface

nitude. The peak $\epsilon_{\theta\theta}$ variation on the outer surface occurs at the point $\theta = 0^\circ$ and $z = 1.0m$, see figure 4.15. Axial strain ϵ_{zz} (see figure 4.10) becomes tensile (peak value of 0.0026) in the

vicinity of the hot spot. For $\theta > 90^\circ$ all the outer surface experiences zero axial strain. As expected ε_{zz} change in the z -direction is more severe than in the θ -direction. The peak value

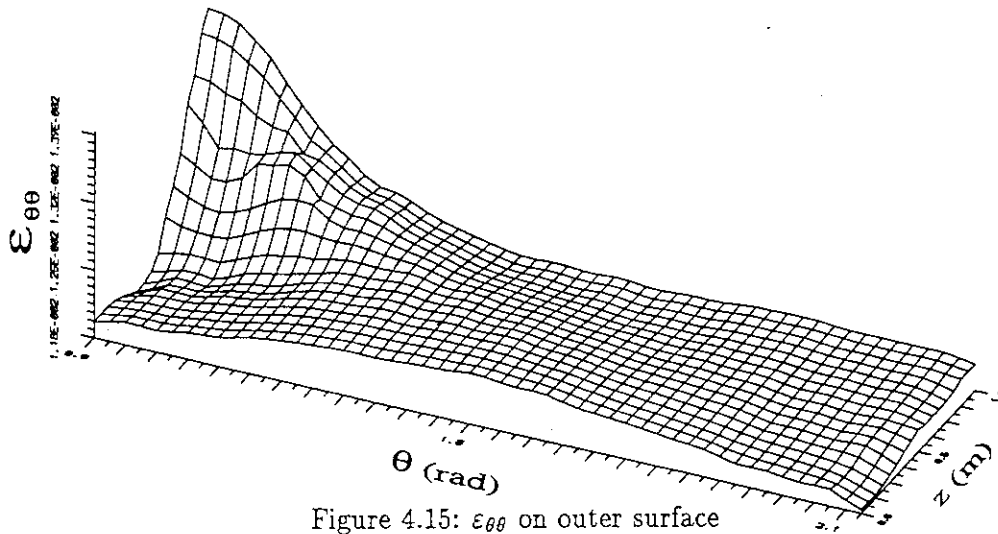


Figure 4.15: $\varepsilon_{\theta\theta}$ on outer surface

on the inner surface (see figure 4.10) is approximately twice as large as the value on the outer surface (see figure 4.16) suggesting that there is a greater axial deformation on the inner surface than the outer. This variation is in agreement with that expected from the thermal boundary conditions imposed in the location of the hot spot. The shear strain $\varepsilon_{r\theta}$ on the inner and outer surfaces are shown in figure 4.11 and figure 4.17, respectively, regions of maxima and minima are

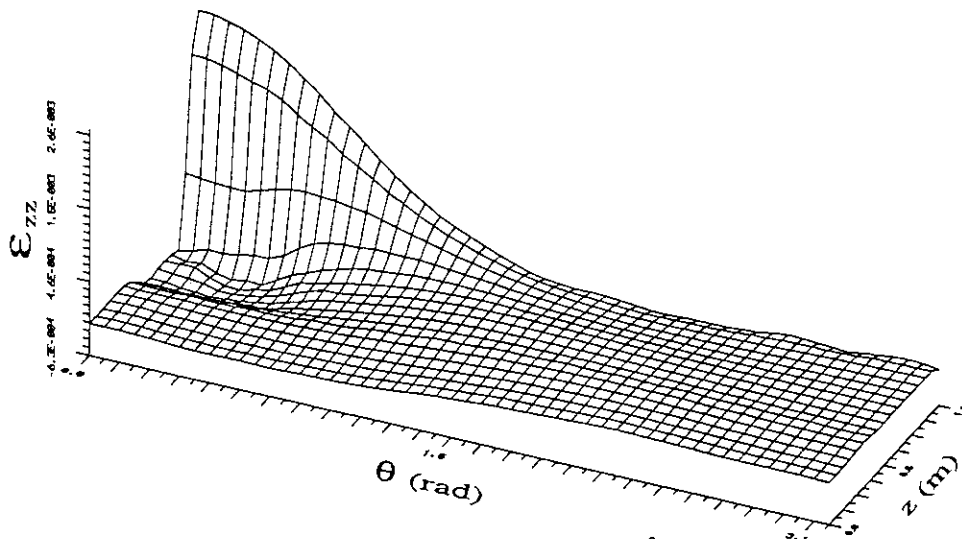


Figure 4.16: ε_{zz} on outer surface

interchanged. Shear strain ε_{rz} is zero everywhere on the outer surface as shown in figure 4.18. The strain $\varepsilon_{\theta z}$ (see figure 4.19) is an order of magnitude lower than values on the inner surface and has a peak variation that occurs at the same θ location and z elevation. At large values of θ and z , both the inner and outer surface variations of $\varepsilon_{\theta z}$ are zero.

Generally, all the strain components on the inner surface are higher than those on the outer surface. This behaviour is reasonable since the inner surface, which is at higher temperature than the outer surface, would experience higher deformations than the outer surface. The swelling observed in figure 4.7 is a direct consequence of these higher strain variations on the inner surface. Further, the strain components do not exhibit rapid changes in the vicinity of the hot spot on the outer surface since the outer surface temperature is uniform relative to the

inner surface temperature.

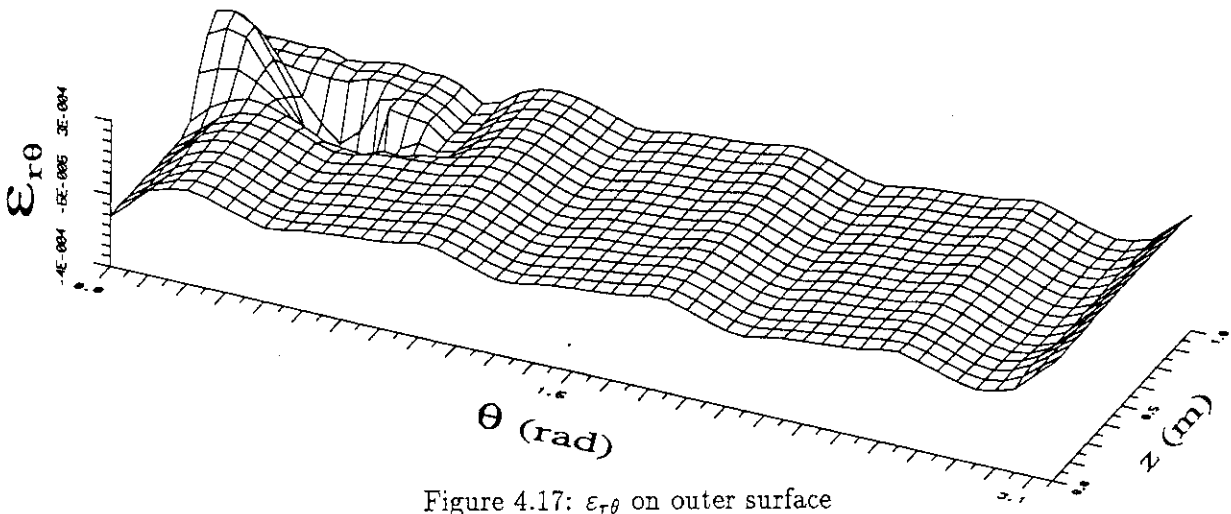


Figure 4.17: $\epsilon_{r\theta}$ on outer surface

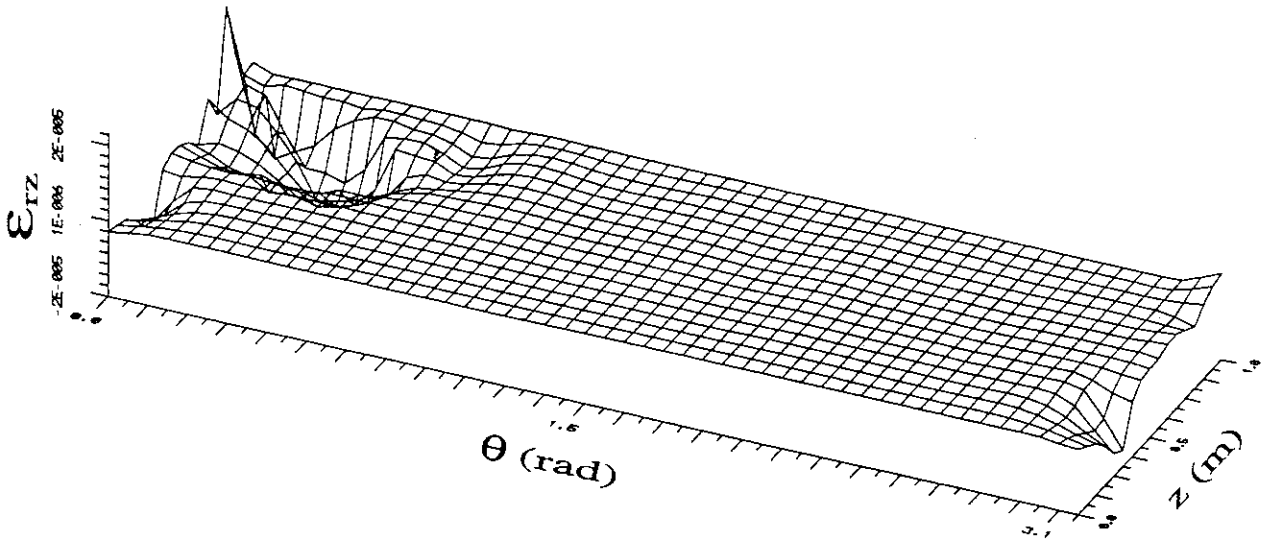


Figure 4.18: ϵ_{rz} on outer surface

The large strain values obtained are a direct consequence of the steady state thermoelastic model employed in the analysis. In the real situation plasticity effects will also be present and these will redistribute the strains such that these are never greater than the yield strain. At large temperatures effects of plasticity cannot be ignored.

Stresses on the inner and outer surfaces are shown in figures 4.20–4.25 and figures 4.26–4.31, respectively. Near geometrical discontinuities such as edges and corners, BEM stresses are not accurately defined since the normal to the surface is not unique. By employing discontinuous elements (see, Brebbia *et. al.*, [6]) at such locations the solutions can be improved. Direct stresses σ_{rr} (see figure 4.20), $\sigma_{\theta\theta}$ (see figure 4.21) and σ_{zz} (see figure 4.22) on the inner surface are all compressive. The σ_{rr} has the smallest magnitude of the direct stresses as expected. Further, fluctuations in σ_{rr} near the edges of the geometry is apparent. The tangential stress $\sigma_{\theta\theta}$ and axial stress σ_{zz} remote from the hot spot location have constant values of -1743MPa and -3356MPa, respectively. In the hot spot region these peak to -3254MPa and -5049MPa, respectively. Thus, the hot spot elevates the tangential and axial stresses by factors of 1.9 and 1.5, respectively. The axial stress (σ_{zz}) has the largest magnitude, which arises due to the axial constraint at elevations of z equal to 0.0m and 1.0m. In comparison to $\sigma_{\theta\theta}$ and σ_{zz} the shear stresses $\sigma_{r\theta}$

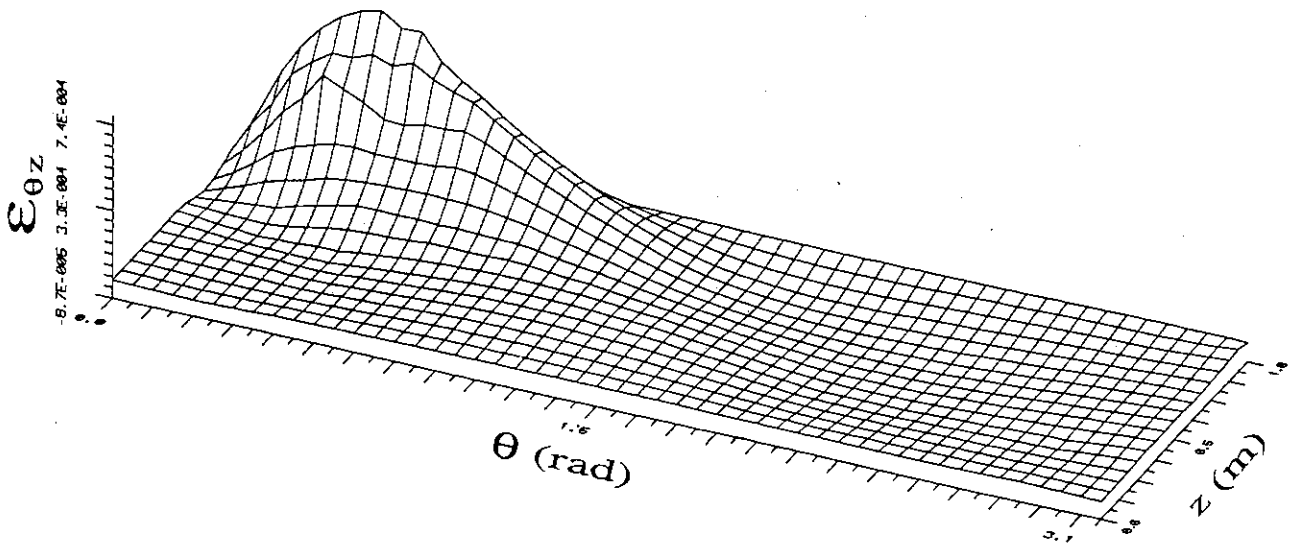


Figure 4.19: $\epsilon_{\theta z}$ on outer surface

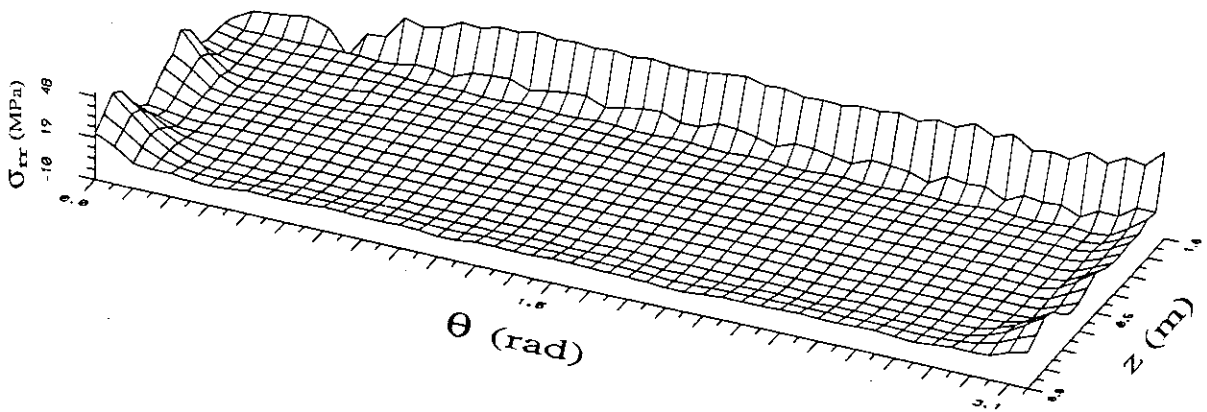


Figure 4.20: σ_{rr} on inner surface

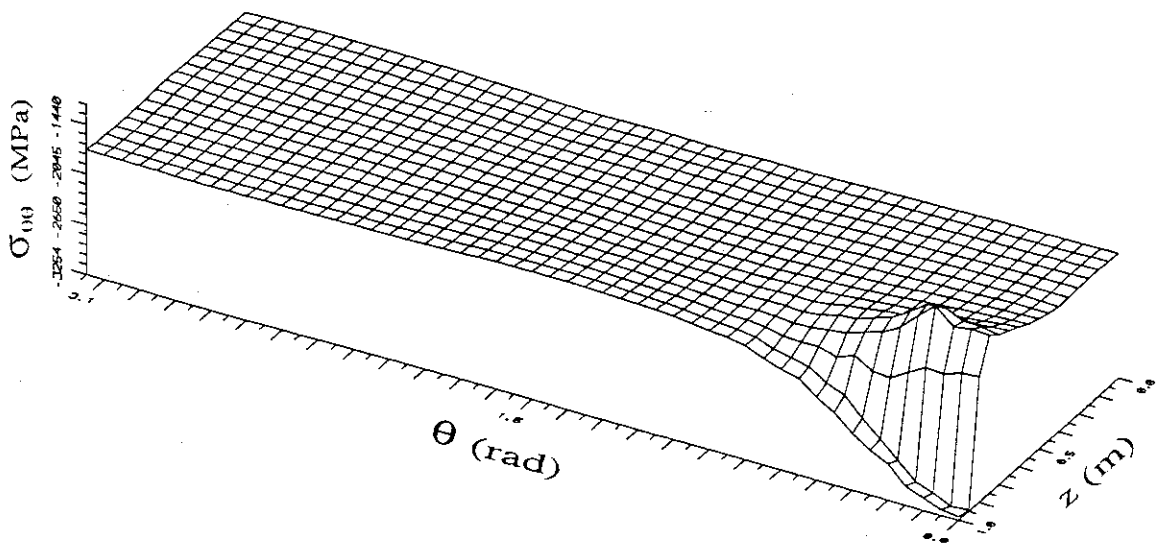


Figure 4.21: $\sigma_{\theta\theta}$ on inner surface

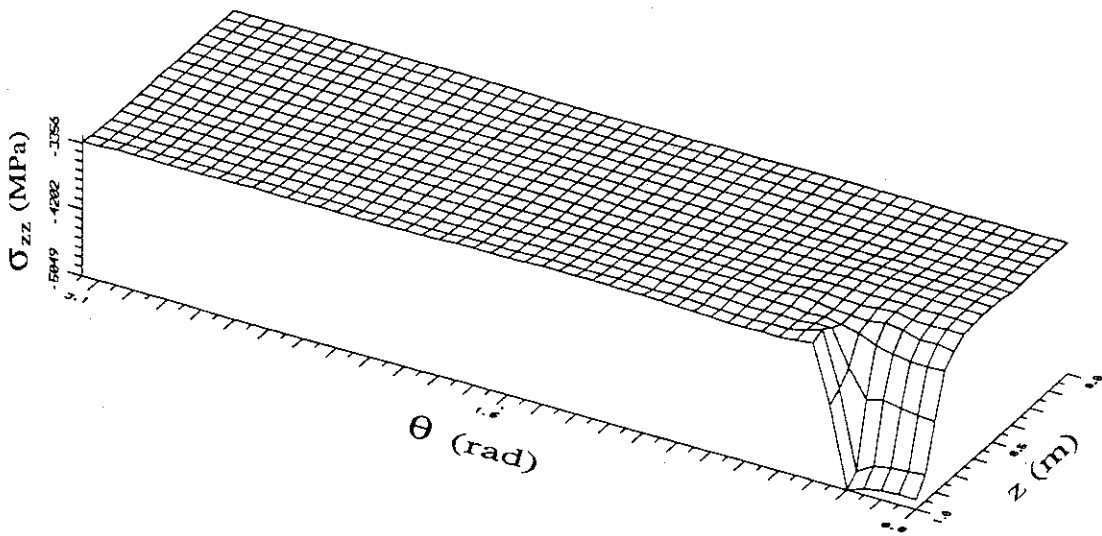


Figure 4.22: σ_{zz} on inner surface

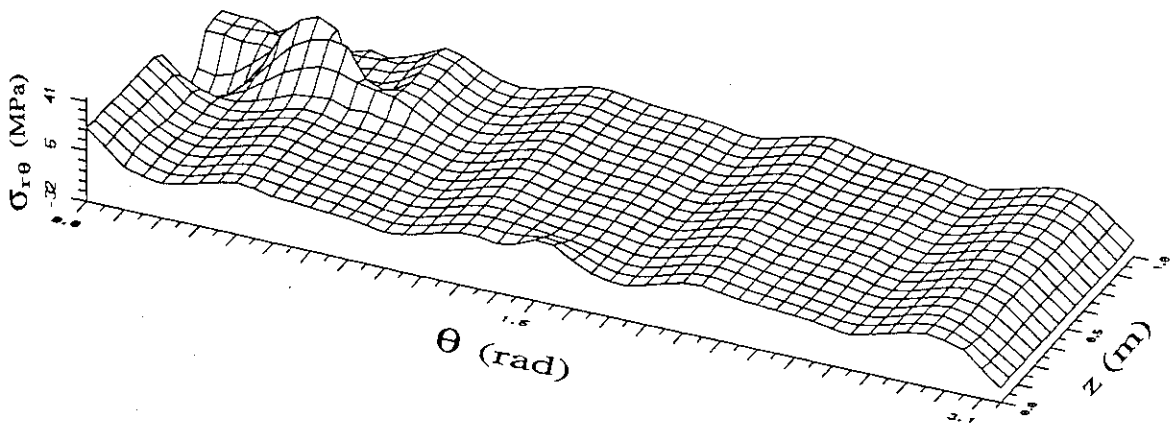


Figure 4.23: $\sigma_{r\theta}$ on inner surface

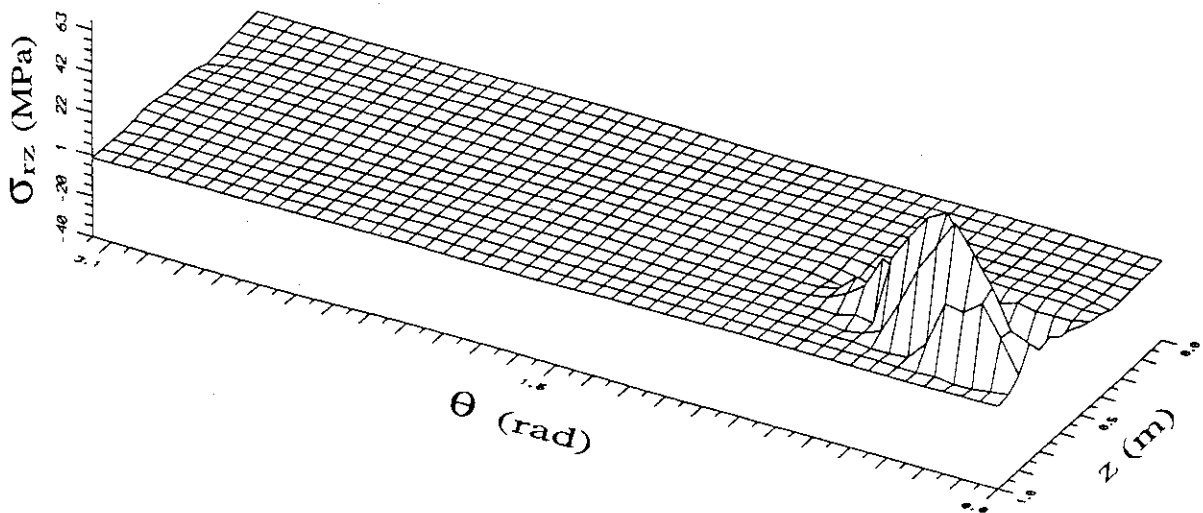


Figure 4.24: σ_{rz} on inner surface

(see figure 4.23), σ_{rz} (see figure 4.24) and $\sigma_{\theta z}$ (see figure 4.25) are extremely small and can thus be neglected. The largest shear stress with a peak magnitude of 651MPa occurs for $\sigma_{\theta z}$ in the vicinity of the hot spot. Far from the hot spot all the shear stresses are essentially zero.

The direct stresses σ_{rr} and $\sigma_{\theta\theta}$ are both tensile on the outer surface, see figure 4.26 and figure 4.27; σ_{rr} is negligible. The presence of the hot spot increases $\sigma_{\theta\theta}$ by a factor of approximately 1.2 relative to its value remote from the location of the hot spot. Axial stress σ_{zz} for $\theta > 90^\circ$ is tensile with an average value of 33MPa. For $\theta \leq 90^\circ$ σ_{zz} becomes compressive, at $\theta = 0^\circ$ and zero z elevation the compressive value is -8MPa. In the vicinity of the hot spot the

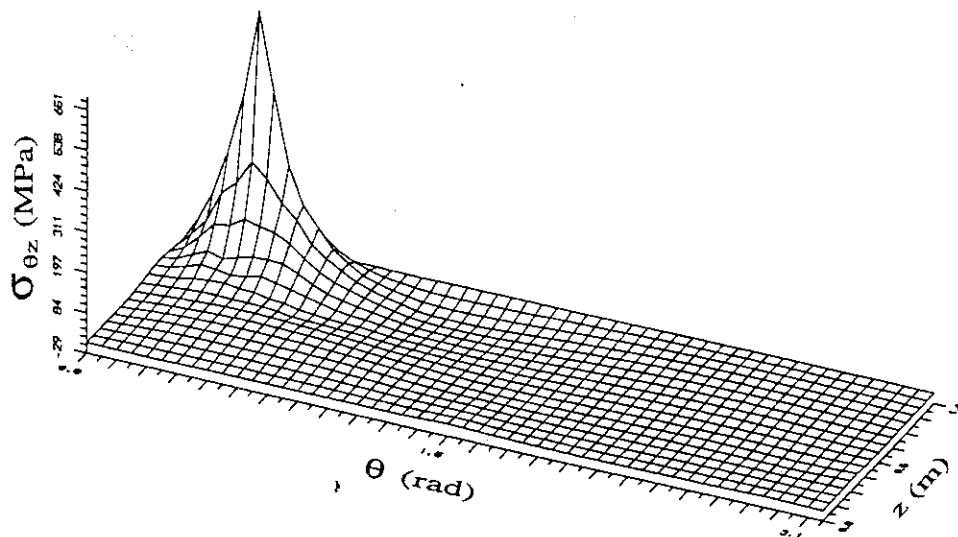


Figure 4.25: $\sigma_{\theta z}$ on inner surface

axial stress becomes tensile and attains a maximum value of 600MPa. As on the inner surface the shear stresses $\sigma_{r\theta}$ and σ_{rz} are insignificant in comparison with the direct stresses $\sigma_{\theta\theta}$ and σ_{zz} , see figure 4.29 and figure 4.30. The shear stress $\sigma_{\theta z}$ in figure 4.31 also becomes tensile (peak value of 100MPa) in the region of the hot spot on the outer surface. Outside this region it is zero.

From a structural integrity point of view, presence of large stress elevations in the vicinity of the hot spot could be detrimental. Generally, the highly elevated stresses on the inner and outer surface are in a state of compression and tension, respectively. The tensile stresses are extremely important since they can act as sites of crack initiation and subsequent propagation. Further, if a crack like defect is already present prior to the formation of the hot spot then it is possible that once a hot spot is formed the elevated tensile stresses could lead to its propagation. Once a crack propagates through the thickness the leak worthiness of the hot leg comes into question.

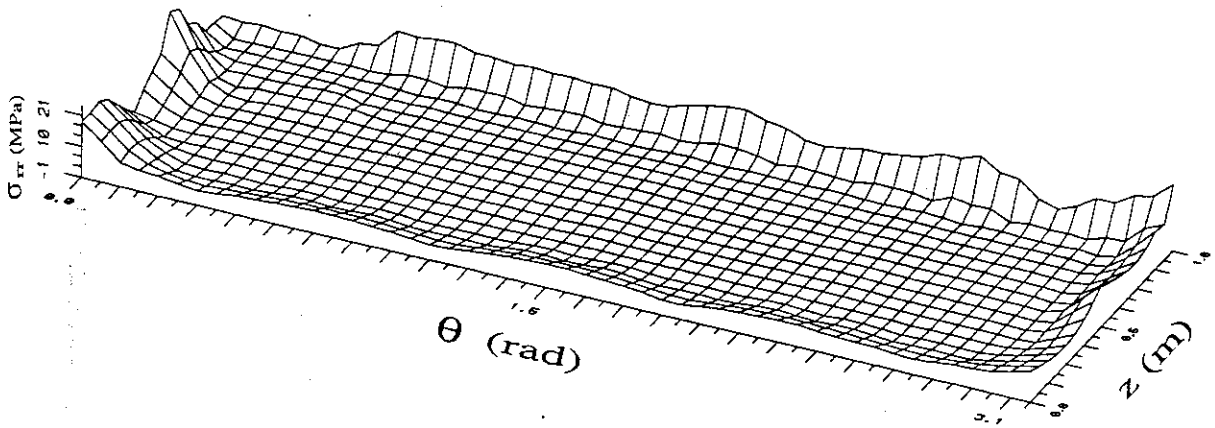


Figure 4.26: σ_{rr} on outer surface

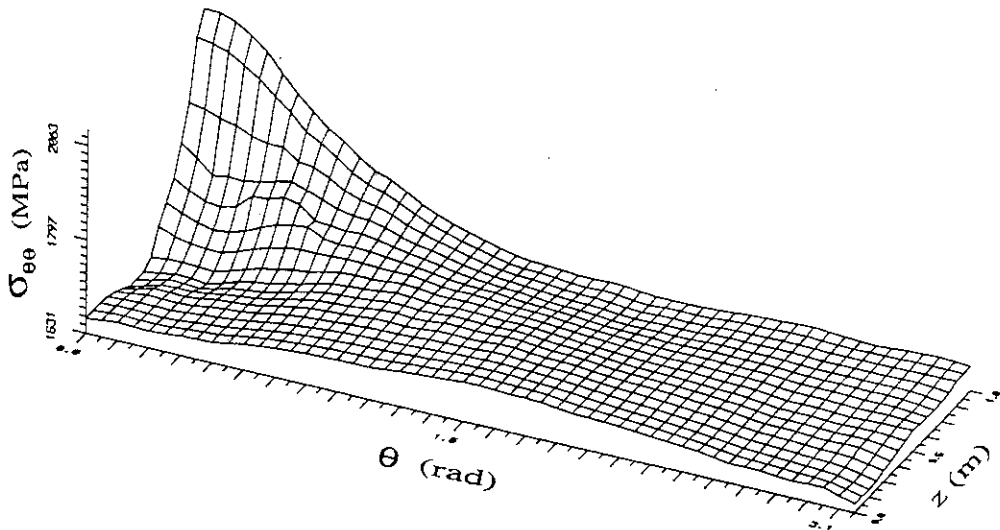


Figure 4.27: $\sigma_{\theta\theta}$ on outer surface

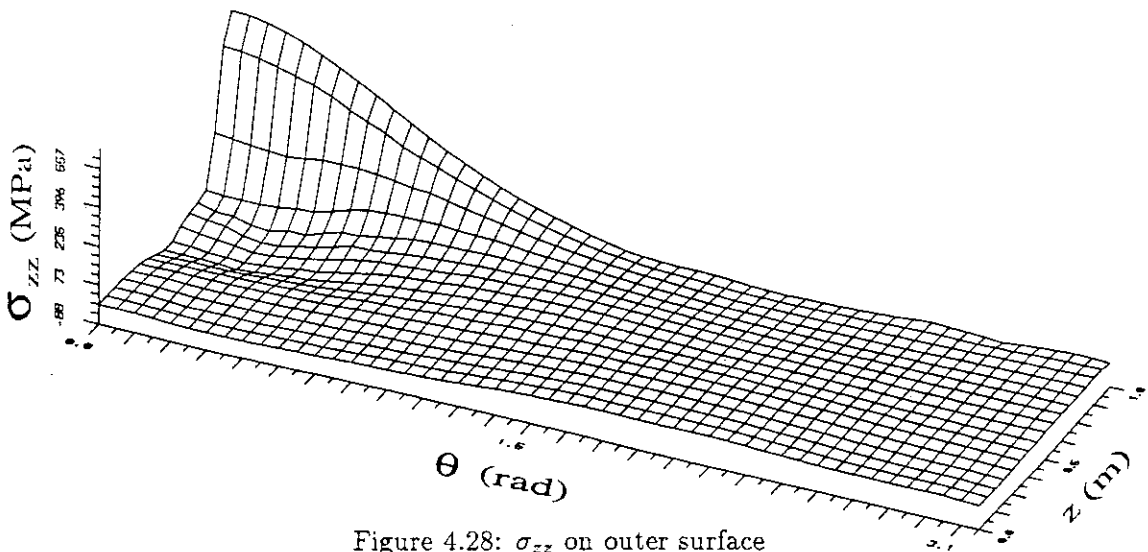


Figure 4.28: σ_{zz} on outer surface

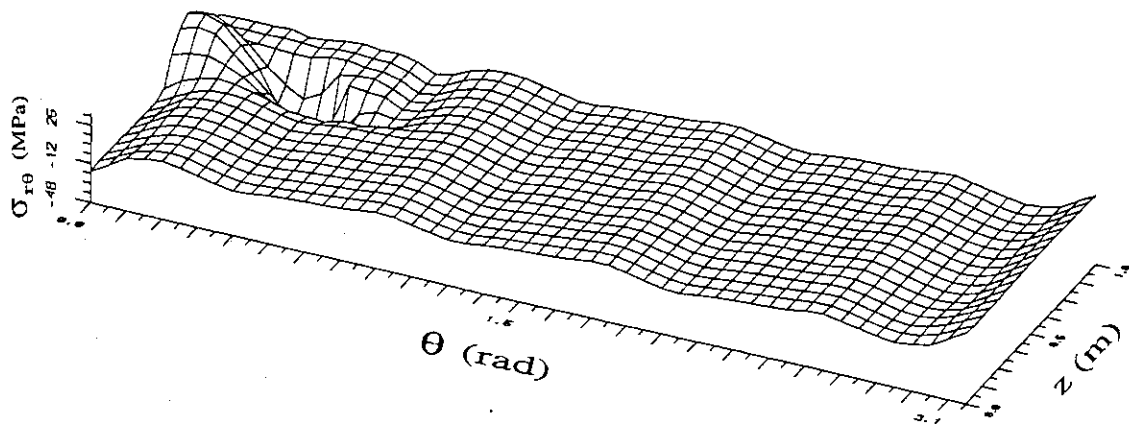


Figure 4.29: $\sigma_{r\theta}$ on outer surface

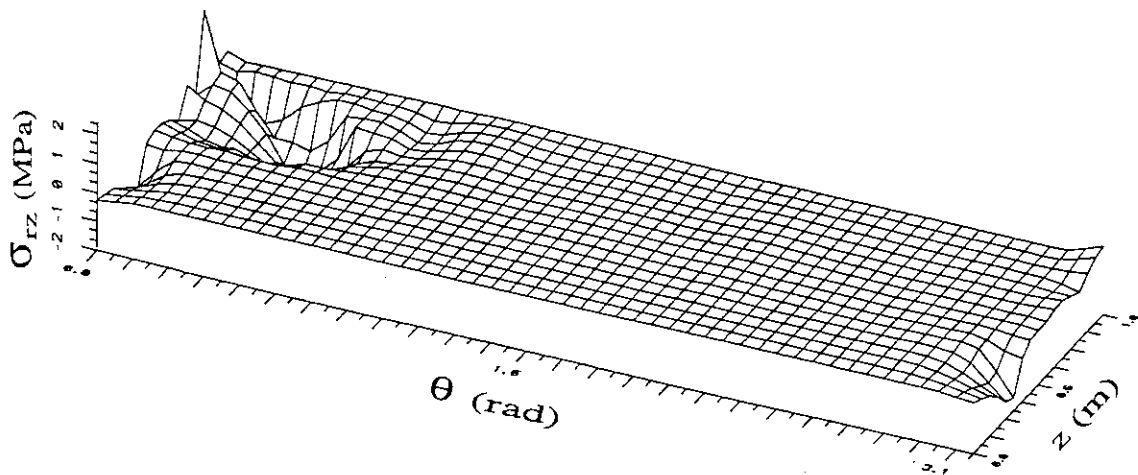


Figure 4.30: σ_{rz} on outer surface

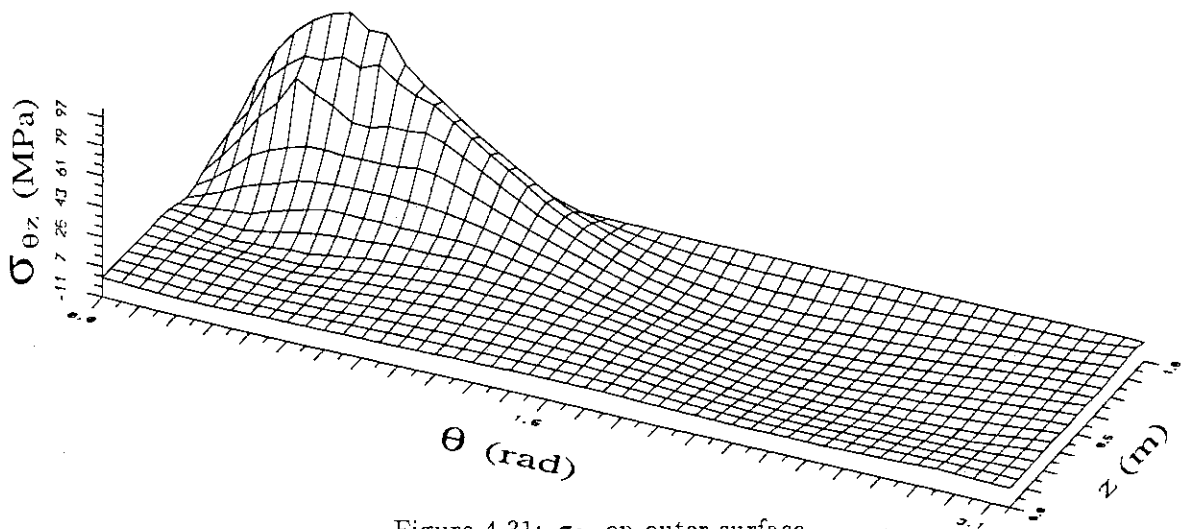


Figure 4.31: $\sigma_{\theta z}$ on outer surface

4.2 Hot Spot at Bend Section of Hot leg

Fission product aerosol deposition is more likely to take place at locations where the fluid flow direction is altered. Such an alteration occurs at the bend section of a hot leg and it is at this location that deposition could occur due to inertial impact. At the deposition site decay heat will give rise to thermal stresses that could threaten the structural integrity of the hot leg. Hence, it is important that the structural response of the bend section is understood.

In the modelling it is assumed that the hot leg has a 90° bend section. In practice the actual bend section forms a 60° angle, subsequently the 90° bend chosen for the analysis represents an extreme case. Further, fission product aerosol deposition models under development at JAERI are at present limited to a 90° bend geometry.

In practise the hot leg is supported by the the reactor pressure vessel and the steam generator. During normal operating conditions initial strains and stresses at the supports prior to the severe accident will be present. No attempt is made to model these initial strains and stresses since this data was not available at the time the analysis was conducted. In the analysis that follows it is assumed that at the steam generator—hot leg connection, no axial deformation of the hot leg occurs, only radial expansion is allowed. With reference to the schematic diagram of the cross-section through a 90° bend shown in figure 4.32, this axial constraint implies that

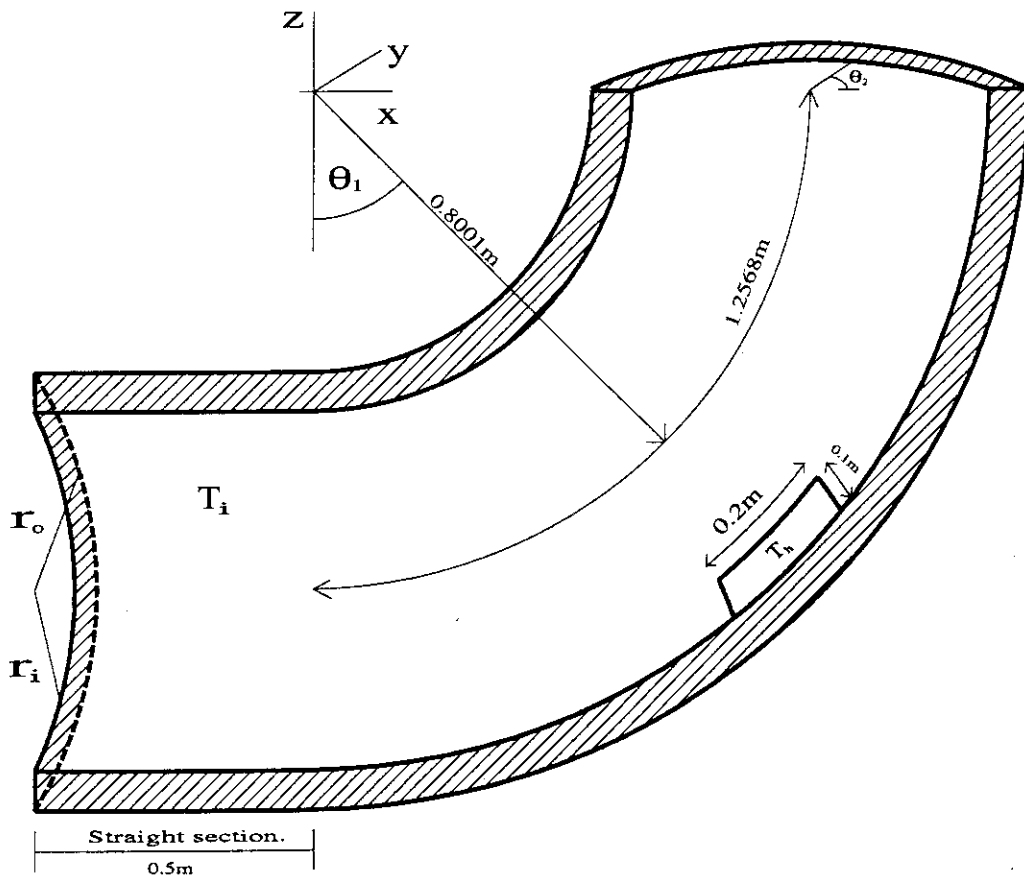


Figure 4.32: Bend geometry definition

U_z is zero at $z = 0.0m$ and expansion can only occur in the $x-y$ plane.

Any attempts to analyse the complete hot leg (*i.e.*, straight section of length 0.39762m and bend section) as shown in figure 3.1 using a three-dimensional model would require extremely large degrees of freedom and would be computationally expensive. Complete modelling

of the straight section is not necessary since at large distances from the hot spot location the structural response will become independent of the presence of the hot spot. This behaviour has been established for a hot spot situated in the straight section of the hot leg in § 4.1. Thus to reduce the model size a 90° bend with a straight section of $0.5m$ length is considered as depicted in figure 4.32. The inner r_i and outer r_o radii are identical to those used in § 4.1. The 90° bend has a radius of $0.8001m$.

In the simplified model, the constraints need to be established at the end of the straight section of $0.5m$ length, since the same constraints occurring at the pressure vessel-hot leg connection cannot be employed here. Referring to figure 4.32 an axial constraint at $x = -0.5m$ is applied which prevents the hot leg deformation in the x -direction but allows free expansion in the y - z plane. This constraint is reasonable since axial deformations far from the hot spot location will be negligible as shown in § 4.1. Further, since the problem has a symmetry plane at $y = 0$, with appropriate boundary conditions only half the problem needs to be solved.

In the analysis the hot spot, which is formed as result of fission product aerosol deposition is defined as a square surface patch of dimensions as shown in figure 4.32. It is symmetrically located at $\theta_1 = 45^\circ$ and only half the hot spot is shown in figure 4.32. The temperature transition region (TTR) is defined such that $S_1/S = 0.5$ (see figure 3.4) and has a linear temperature prescribed across it as in § 4.1. Hot spot temperature T_h and inner wall temperature T_i were prescribed the same values as those used in § 4.1.

Two separate analyses are conducted on the bend section defined above. In the first analysis, the outer wall temperature T_o is prescribed the same value as that used in § 4.1. In this case there is heat flow through the hot leg thickness due to the difference in temperature between the inner and outer walls. For the second analysis adiabatic boundary conditions are prescribed on the outer wall surface. The latter case is analogous to having an insulator on the outer surface that prevents heat loss from the hot leg to the surrounding environment.

For both analyses the same boundary element mesh was employed. This mesh, for the half symmetry the problem possesses is shown in figure 4.33 and consists of 408 elements with 3678 degrees of freedom. Nodal mesh points are defined relative to the cartesian coordinates (x, y, z) . The mesh distribution at the hot spot region is difficult to see due to the curvature of the bend. An internal pressure of 0.554MPa is also prescribed in the hot leg, outer surface is traction free. The two separate analyses can be done quite easily by changing the prescribed thermal boundary conditions on the mesh nodes defined over the outer hot leg surface.

As in § 4.1 results in terms of displacements, strains and stresses will be presented as variations over the inner and outer hot leg surfaces. In the analysis that follows, the surface variation of displacements, strains and stresses will be restricted to the 90° bend section since the surfaces can be uniquely defined in terms of a radius r and two angles θ_1 and θ_2 as shown in figure 4.34. The BEM code generates solutions in terms of cartesian coordinates (x, y, z) . Using this coordinate system, analysis of the results becomes difficult. A more suitable choice of a reference system would be cylindrical polar coordinates (r, θ_2, x') as defined in figure 4.34. This system also allows direct comparison of the results with those obtained in § 4.1. Consequently all solutions are transformed from the (x, y, z) to the (x', y', z') coordinate system centered along the hot leg axis, see figure 4.34. This constitutes a rotation of the original coordinate system (x, y, z) about the y -axis, consequently the y -axis and y' -axis are identical. Solutions in the cylindrical polar coordinates (r, θ_2, x') can be obtained from the cartesian coordinate system (y', z', x') . The angle θ_2 is measured relative to the y' axis and has positive direction from y' to z' . In the cylindrical polar coordinate system x' is directed along the hot leg axis and z' is directed towards the origin of the original coordinate system (x, y, z) . Any cross-section through the bend section is defined by the $y'-z'$ plane. Further the inclination of the $y'-z'$ plane is defined in terms of the angle θ_1 . Thus, any point on the inner or outer surface can be defined in terms of (r, θ_1, θ_2) , where $0^\circ \leq \theta_1 \leq 90^\circ$ and $-90^\circ \leq \theta_2 \leq 90^\circ$. The transformations needed to

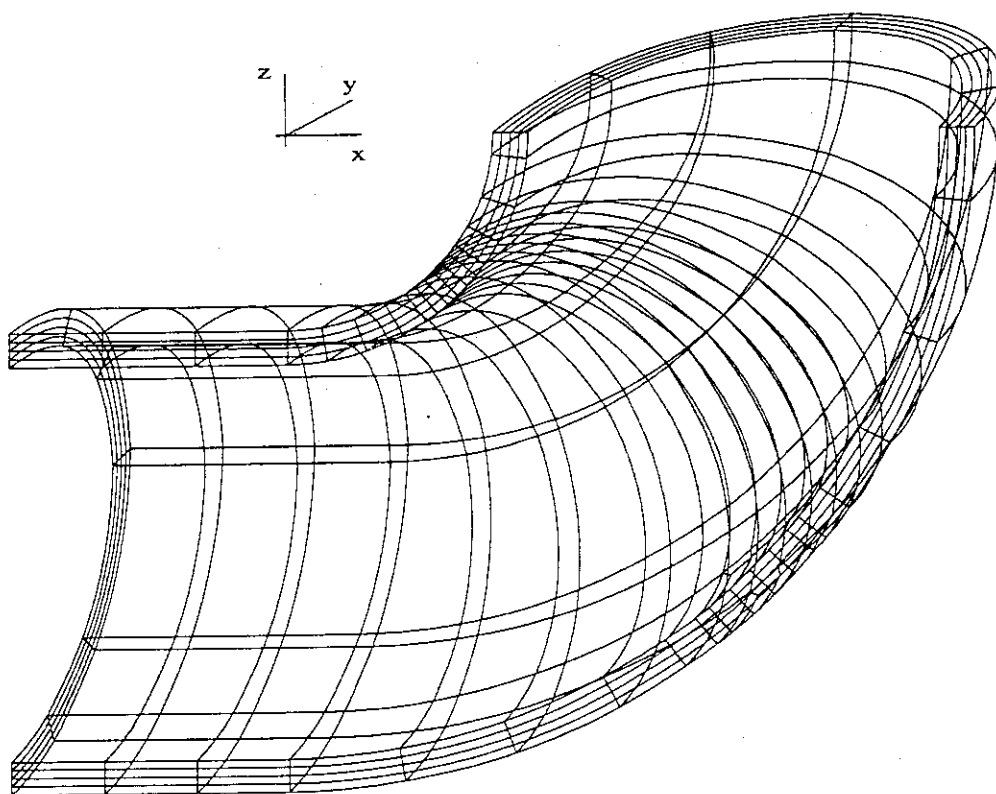


Figure 4.33: Mesh for bend analysis

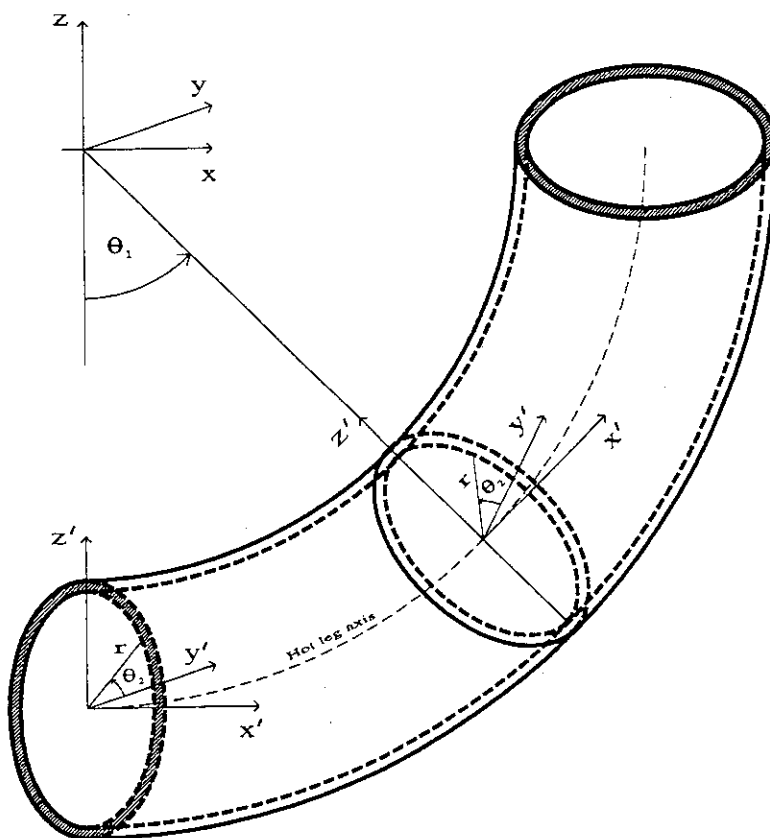


Figure 4.34: Cylindrical polar Coordinates centered on hot leg bend axis.

derive the displacements, strains and stresses in the cylindrical polar coordinates (r, θ_2, x') from the original cartesian coordinate system (x, y, z) can be found in § B.1 and § B.2. Solutions for the case when constant temperature boundary conditions are prescribed on the outer surface are presented in § 4.2.1, while solutions obtained when adiabatic boundary conditions are prescribed on the outer surface are presented in § 4.2.2.

4.2.1 Constant temperature boundary conditions on outer surface

The hot leg deformation obtained when the outer wall temperature is prescribed the same value as that used in § 4.1 is shown in figure 4.35. The original undeformed mesh is shown drawn

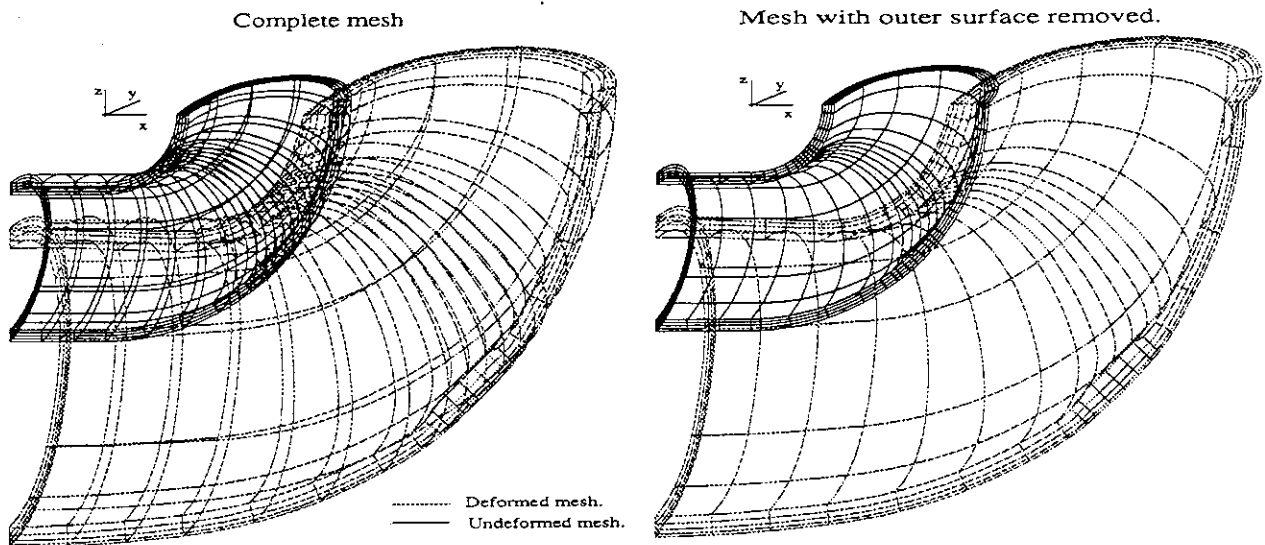
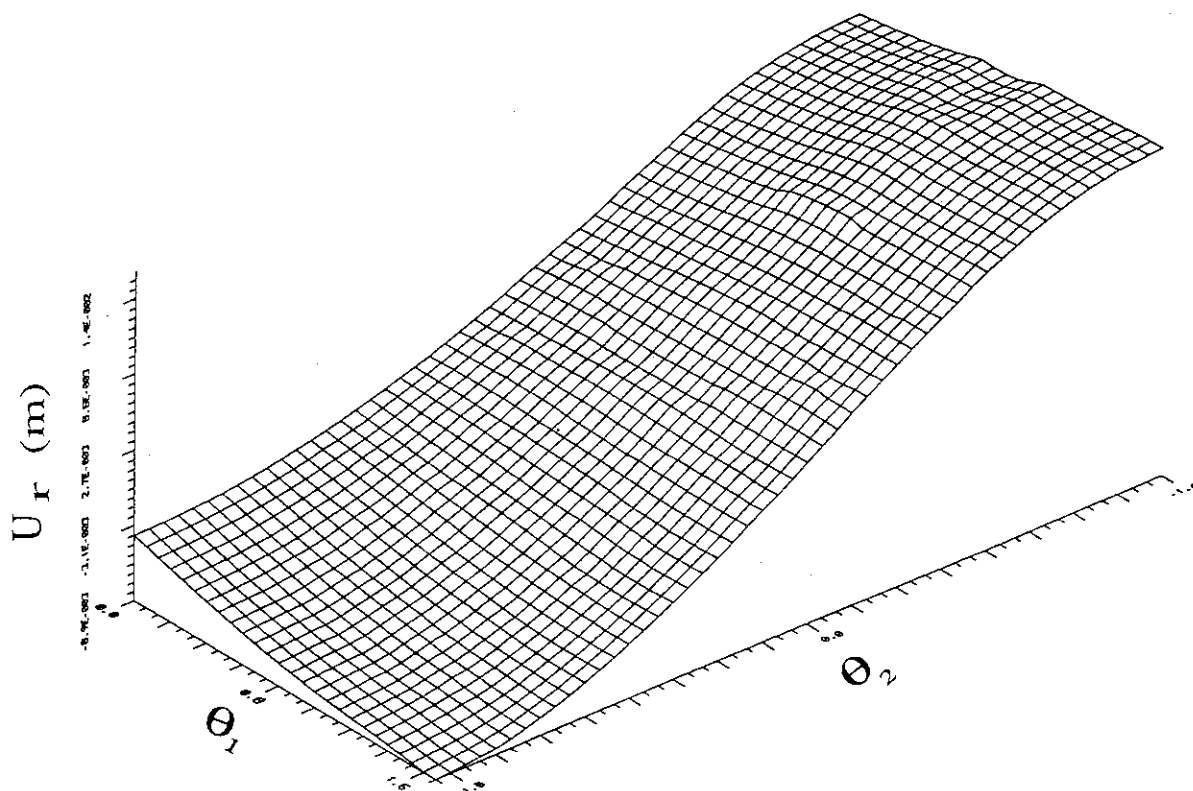


Figure 4.35: Bend deformation: temperature prescribed on outer surface

with a continuous line, while the deformed mesh which has been magnified by a factor of 80% is shown drawn with a dotted line. Swelling of the inner surface of the bend section at the location of the hot spot can be seen in the deformed mesh with the outer surface removed. This localised behaviour exhibits the same characteristics as those obtained in § 4.1 for the straight section analysis. In this analysis and that presented in § 4.1, identical thermal boundary conditions exist in the vicinity of the hot spot, thus, the deformation in this region must be similar for the two cases as obtained.

The global deformation of the bend section is as expected. At $z = 0.0m$ and $x = -0.5m$ (see figure 4.35), imposed axial constraints allow deformations to take place in the x - y and y - z planes, respectively. Hot leg movement at $z = 0.0m$ occurs in the x direction due to reaction forces generated by the axial constraint at $x = -0.5m$. Conversely, reaction forces generated by the axial constraint at $z = 0.0m$ produces movement of the hot leg in the negative z direction.

Inner and outer surface deformations measured relative to the cylindrical polar coordinates (r, θ_2, x') defined in figure 4.34 can be obtained by employing the transformations given in § B.1. It must be borne in mind that this coordinate system is not fixed but moves along the bend axis as the angle θ_1 varies, see figure 4.34. With respect to this system the inner surface variations of the radial U_r , tangential U_{θ_2} and axial $U_{x'}$ deformations are plotted in figure 4.36, figure 4.37 and figure 4.38, respectively. The surface is defined in terms of the angles θ_1 and θ_2 , where $\theta_2 = \pm 90^\circ$ defines the half symmetry plane of the problem and the hot spot occurs at $\theta_1 = 45^\circ$ and $\theta_2 = -90^\circ$. In the hot spot location a decrease in the radial deformation U_r

Figure 4.36: Inner surface variation of U_r

can be seen in figure 4.36. This corresponds to the swelling observed on the inner surface in figure 4.35 at the same location. Maximum radial deformation occurs along the edge $\theta_2 = -90^\circ$ as expected from intuitive arguments. Along the edge $\theta_2 = 90^\circ$ U_r is negative. This occurs due to movement of the hot leg axis. Hot leg deformation no longer takes place relative to its axis as in the straight section analysis presented in § 4.1.

The tangential deformation U_{θ_2} presented in figure 4.37 is zero along edges $\theta_2 = \pm 90^\circ$ as expected. This zero value occurs because on the symmetry plane of the problem $U_y = 0$ was prescribed. Within the range $-90^\circ < \theta_2 < 90^\circ$ all the U_{θ_2} variation is negative since the hot leg axis moves during thermal expansion of the hot leg bend section. This axial movement takes place due to the bend geometry and the imposed constraints. Even if the hot spot was not present axial movement would still take place.

As in the straight section analysis § 4.1, a local increase in U_{θ_2} takes place adjacent to the hot spot location, see figure 4.37. This localised variation can be attributed to thermal expansion resulting from the presence of the hot spot. The maximum variation of U_{θ_2} occurs at $\theta_2 = 0^\circ$ and is order of magnitude lower than the maximum variation of U_r in figure 4.36.

Axial deformation U_x , presented in figure 4.38 is zero at $\theta_1 = 90^\circ$. This zero value arises due to the prescribed zero axial constraint at $z = 0.0m$. The prescribed axial constraint at $x = -0.5m$ generates the observed maximum U_x variation at $\theta_1 = 0^\circ$ (or $x = 0.0m$). Generally U_x is positive within the entire θ_1 and θ_2 range and decreases to zero as θ_1 increases. This positive variation arises when the cartesian component of the displacement vectors U_x (positive quantity) and U_z (negative quantity) are substituted into equation B.4 of § B.1. The influence of the hot spot on the axial deformation can be seen in figure 4.38.

Across the thickness, expansion is also evident. The element width increases on moving from the outer to the inner surface. Thus, as in § 4.1 the inner surface undergoes greater deformation than the outer surface since $T_i > T_o$ as expected.

Stresses in the cylindrical polar coordinate system defined in figure 4.34 were also obtained

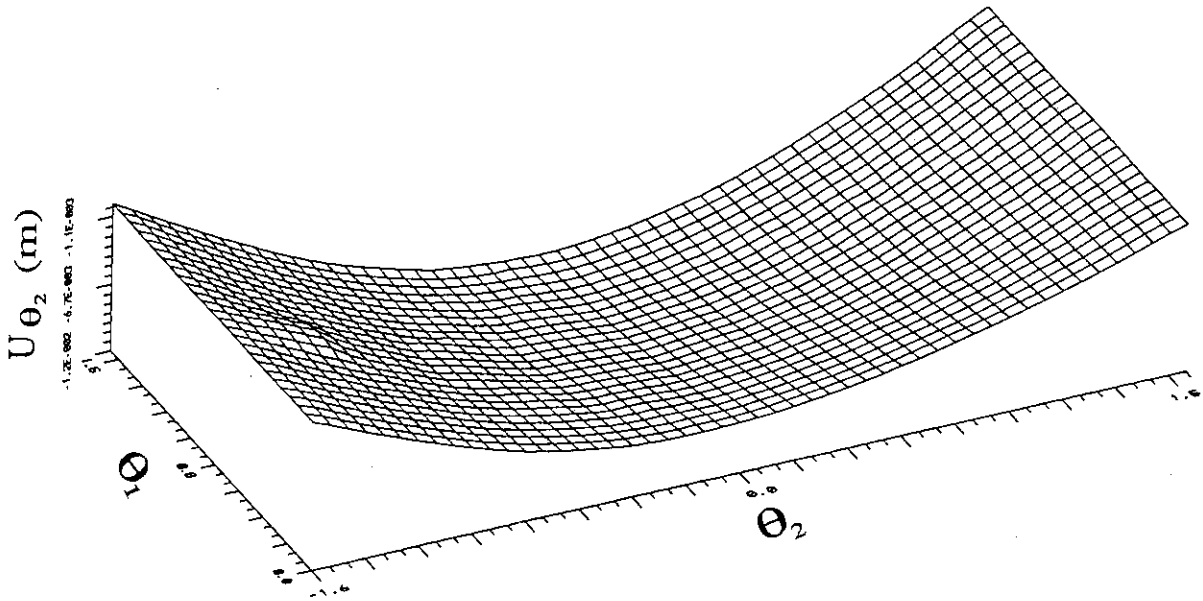


Figure 4.37: Inner surface variation of U_{θ_2}

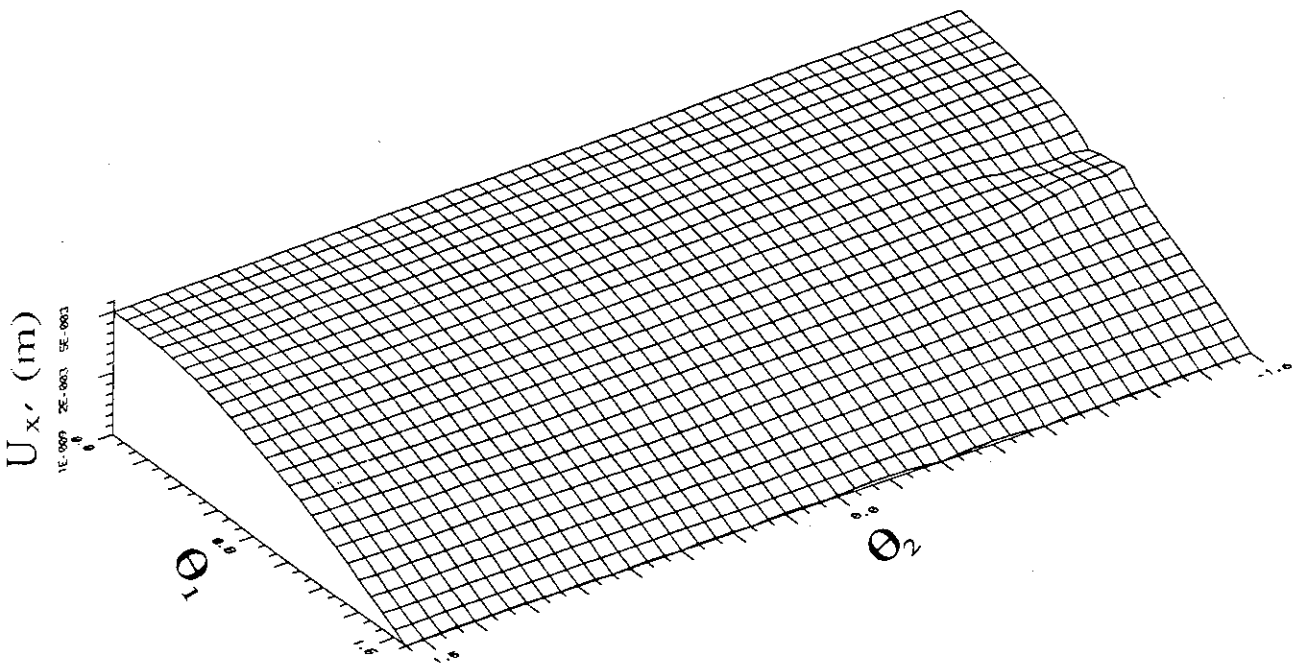


Figure 4.38: Inner surface variation of $U_{x'}$

using the transformations presented in § B.2. The inner and outer surface variation of these stresses are shown in figures 4.39–4.44 and figures 4.45–4.50, respectively. Generally large stress variations are obtained as in the analysis conducted in § 4.1. These result from the large thermal gradient that exists across the hot leg wall thickness and from the assumptions inherent in the linear elastic model.

The radial σ_{rr} , tangential $\sigma_{\theta_2\theta_2}$ and axial $\sigma_{x'x'}$ stresses are shown in figure 4.39, figure 4.40 and figure 4.41 respectively. Along the edges of the inner surface stress fluctuations become extremely large because the normal vector required in the determination of the stresses from the tractions is not uniquely defined at these locations. These fluctuations can be reduced by increasing the mesh density in this location. Relative to the stresses $\sigma_{\theta_2\theta_2}$ and $\sigma_{x'x'}$ the variation of σ_{rr} is negligible and all the direct stresses are compressive on the inner surface. Remote from the hot spot location the average $\sigma_{\theta_2\theta_2}$ variation has a value of -1829MPa. At the hot spot location ($\theta_1 = 45^\circ, \theta_2 = 0^\circ$) $\sigma_{\theta_2\theta_2}$ peaks to -3644MPa. Therefore, the hot spot increases $\sigma_{\theta_2\theta_2}$ by a factor of 2, which is the same order of magnitude as the straight section analysis (see § 4.1). For the axial stress $\sigma_{x'x'}$ the average variation remote from the hot spot is -1320MPa. This peaks at the hot spot location to a value of -3497MPa, which constitutes an increase by a factor of 2.6. The axial compressive stress variation for the bend section is a lot higher than that obtained for the straight section analysis (see § 4.1).

Shear stresses $\sigma_{r\theta_2}$, $\sigma_{rx'}$ and $\sigma_{\theta_2x'}$ are shown in figure 4.42, figure 4.43 and figure 4.44 respectively. These variations are very small compared with the tangential and axial stresses. Shear stress $\sigma_{r\theta_2}$ has the smallest magnitude and is only slightly affected by the hot spot. The shear stress $\sigma_{rx'}$ is unaffected by the hot spot and is essentially zero for $-30^\circ \leq \theta_2 \leq 30^\circ$, see figure 4.43. Along the edge $\theta_2 = -90^\circ$ it is compressive for $\theta_1 \leq 45^\circ$ and tensile for $\theta_1 > 45^\circ$. The tensile and compressive regions change sign along the edge $\theta_2 = 90^\circ$, see figure 4.43. For the shear stress $\sigma_{\theta_2x'}$, compressive and tensile stresses are produced adjacent to the hot spot. The peak tensile stress is the same order of magnitude as that obtained in the straight section analysis, see § 4.1.

The direct stresses σ_{rr} , $\sigma_{\theta_2\theta_2}$ and $\sigma_{x'x'}$ on the outer surface are shown in figure 4.45, figure 4.46 and figure 4.47, respectively. Once again as expected, the σ_{rr} variation is negligible relative to the other two direct stresses. On the outer surface all the direct stresses are tensile as in the straight section analysis presented in § 4.1. The average value of $\sigma_{\theta_2\theta_2}$ remote from the hot spot location is 2189MPa, see figure 4.46. In the vicinity of the hot spot this value increases to 2781MPa (*i.e.*, an increase by a factor of 1.3). For the axial stress $\sigma_{x'x'}$ the average remote value is 1654MPa, which in the hot spot region increases to a maximum value of 2431MPa. This constitutes to an increase by a factor of 1.5.

The shear stresses $\sigma_{r\theta_2}$, $\sigma_{rx'}$ and $\sigma_{\theta_2x'}$ shown in figure 4.48, figure 4.49 and figure 4.50, respectively, are negligible in comparison with the direct stresses $\sigma_{\theta_2\theta_2}$ and $\sigma_{x'x'}$. Comparisons of the inner (see figure 4.42) and outer (see figure 4.48) surface variations show that regions of tensile and compressive stresses are interchanged, although the variations are very small. For the shear stress $\sigma_{rx'}$, regions of tension and compression are also interchanged on the inner and outer surfaces. The outer surface magnitude of the compressive and tensile stresses is of the same order, see figure 4.49. Regarding $\sigma_{\theta_2x'}$, the outer surface variation is much smaller than the inner surface variation, indicating the decreasing influence of the hot spot through the hot wall thickness.

For the bend analysis the direct stresses are compressive on the inner surface and tensile on the outer surface. This variation is in agreement with that obtained for the straight section analysis of § 4.1. The elevated tensile stresses on the outer surface arising from the presence of the hot spot on the inner surface could also act as site of crack initiation if fatigue or creep is present.

The strain variations can be deduced from the stress variations presented by employing

the constitute equations of linear elasticity. These relationships can be found in [2].

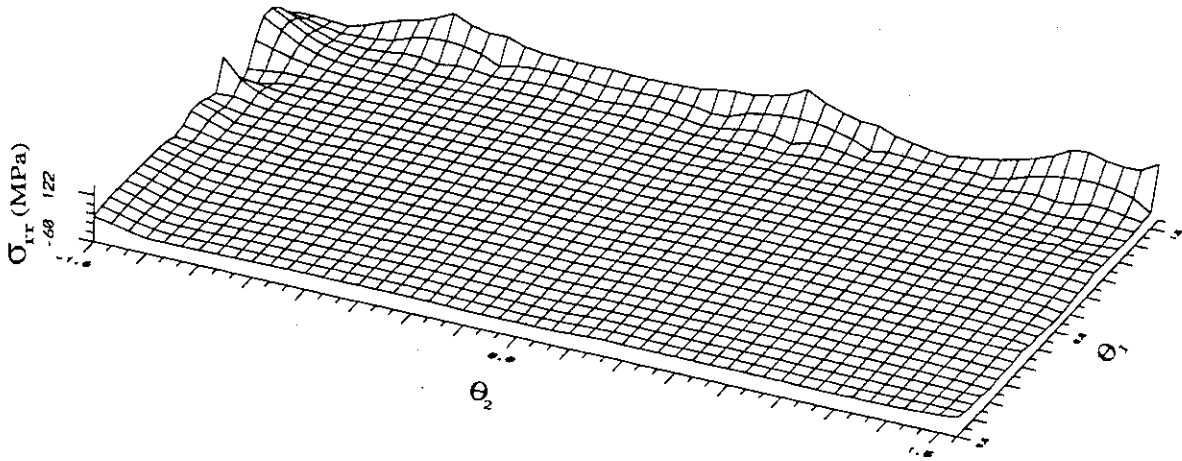


Figure 4.39: σ_{rr} on inner surface

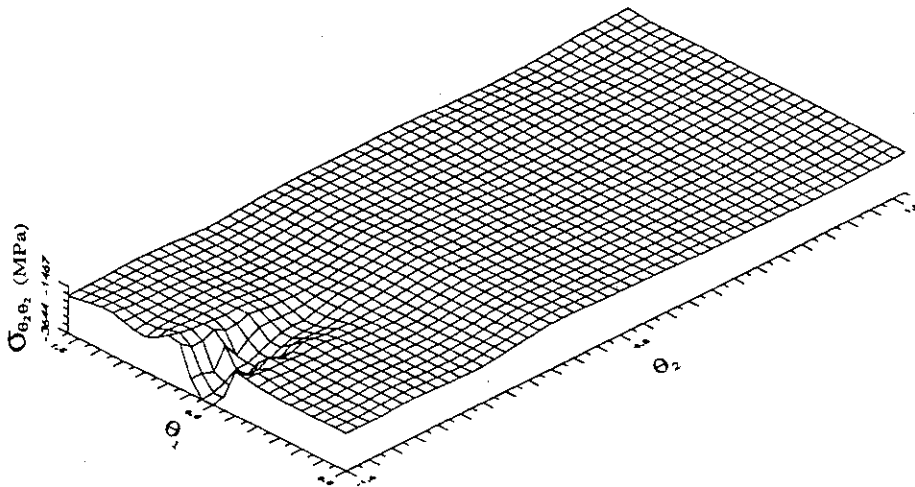


Figure 4.40: $\sigma_{\theta_2\theta_2}$ on inner surface

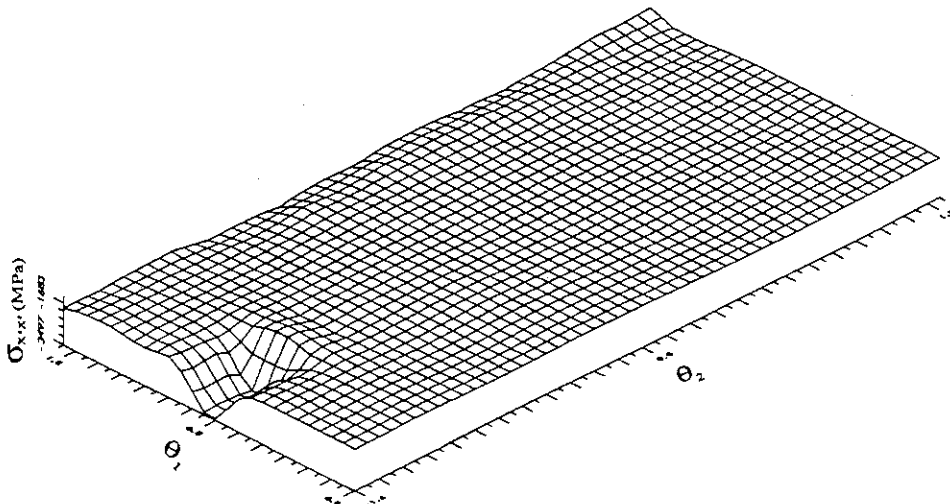


Figure 4.41: $\sigma_{x'x'}$ on inner surface

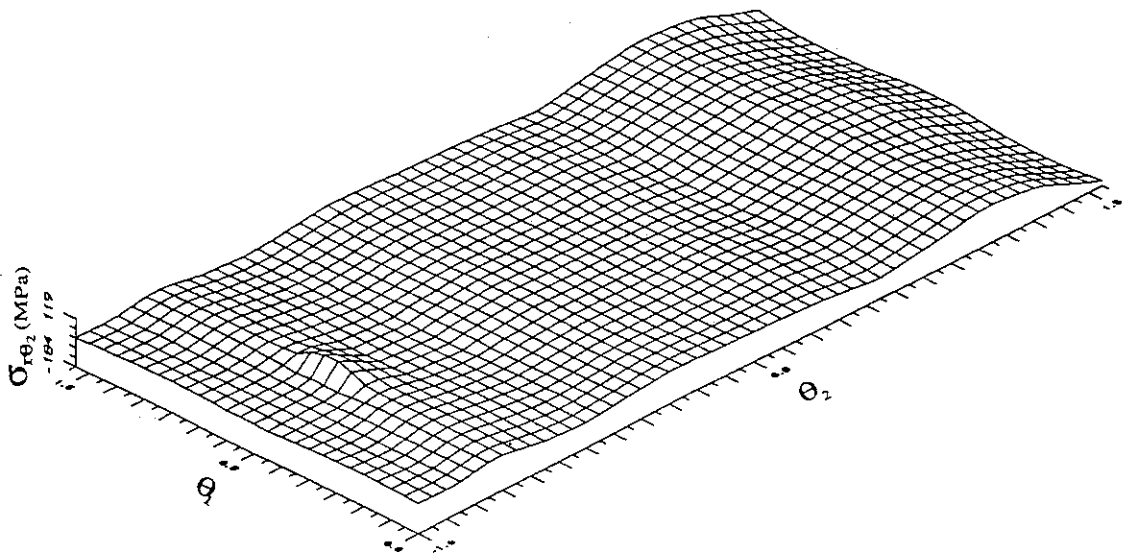


Figure 4.42: $\sigma_{r\theta_2}$ on inner surface

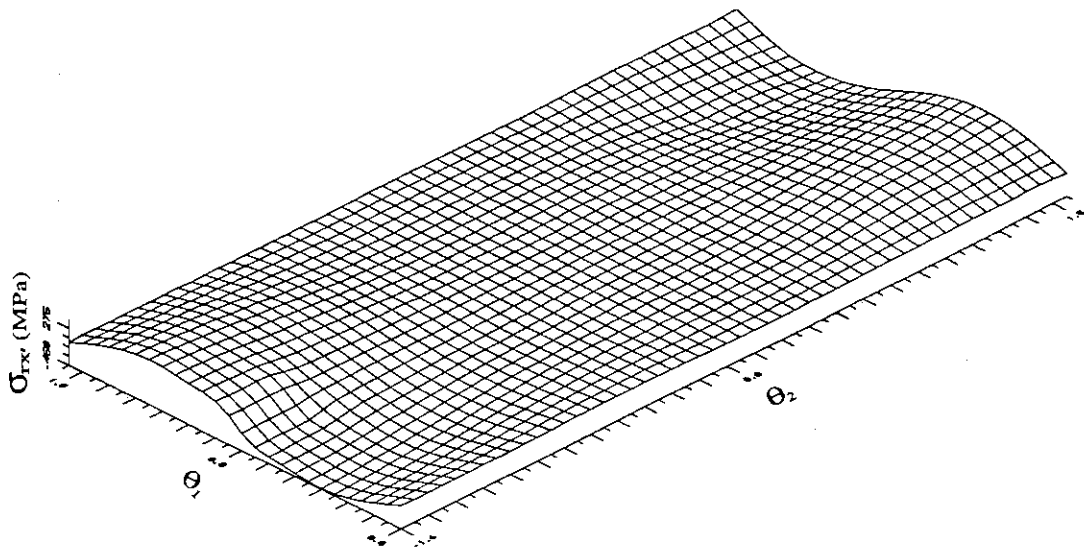


Figure 4.43: $\sigma_{rx'}$ on inner surface

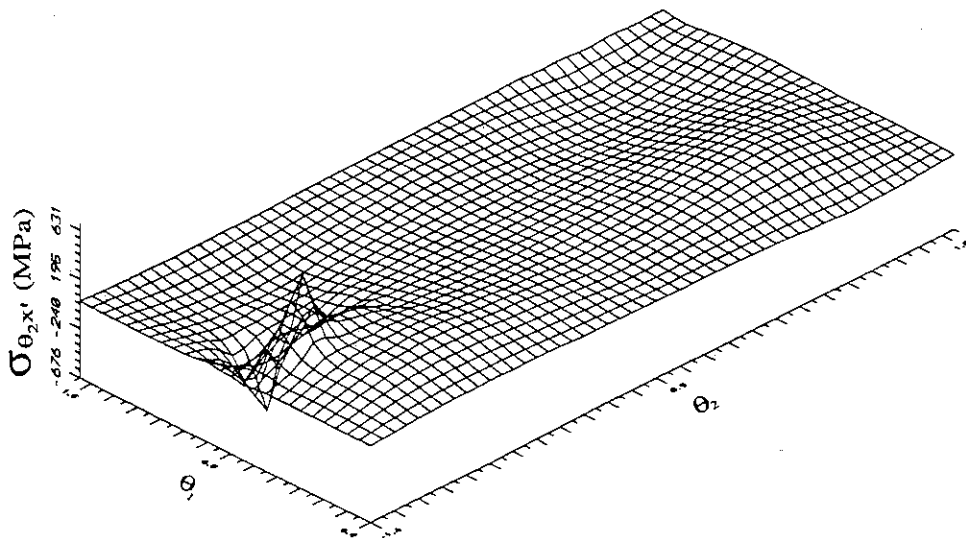


Figure 4.44: $\sigma_{\theta_2 x'}$ on inner surface

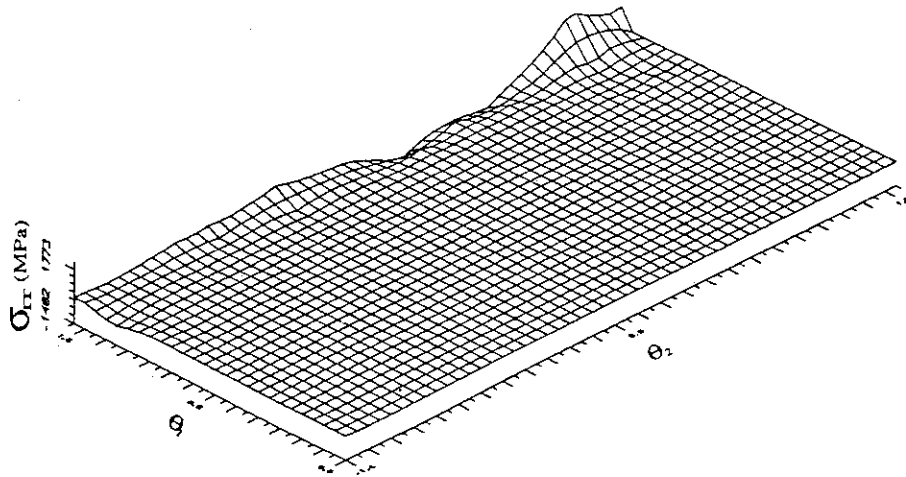


Figure 4.45: σ_{rr} on outer surface

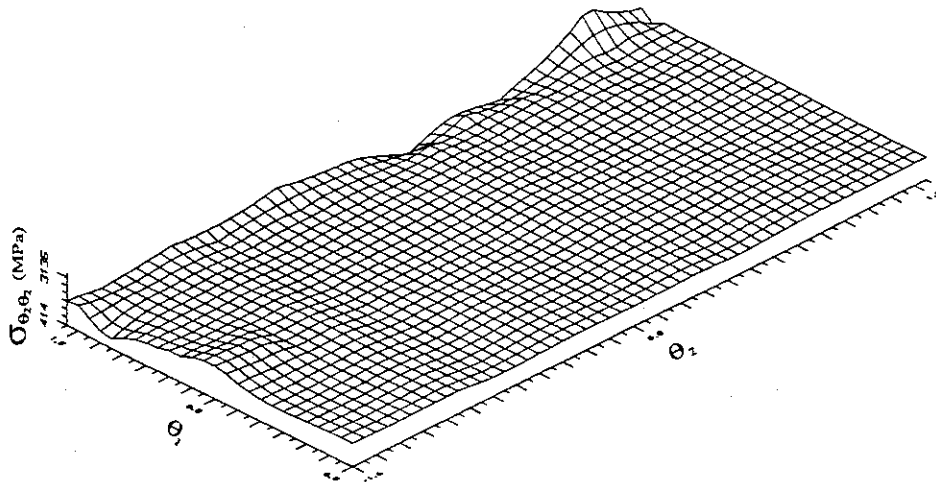


Figure 4.46: $\sigma_{\theta_2\theta_2}$ on outer surface

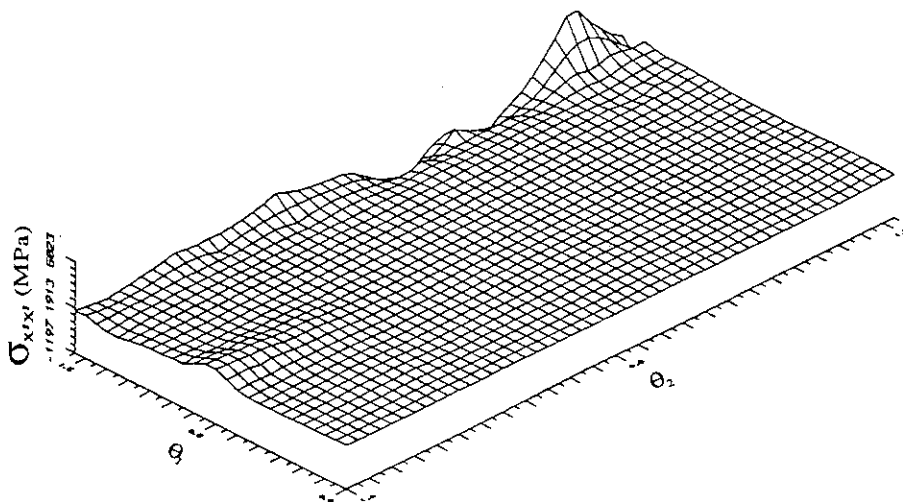


Figure 4.47: $\sigma_{x'_1x'_1}$ on outer surface

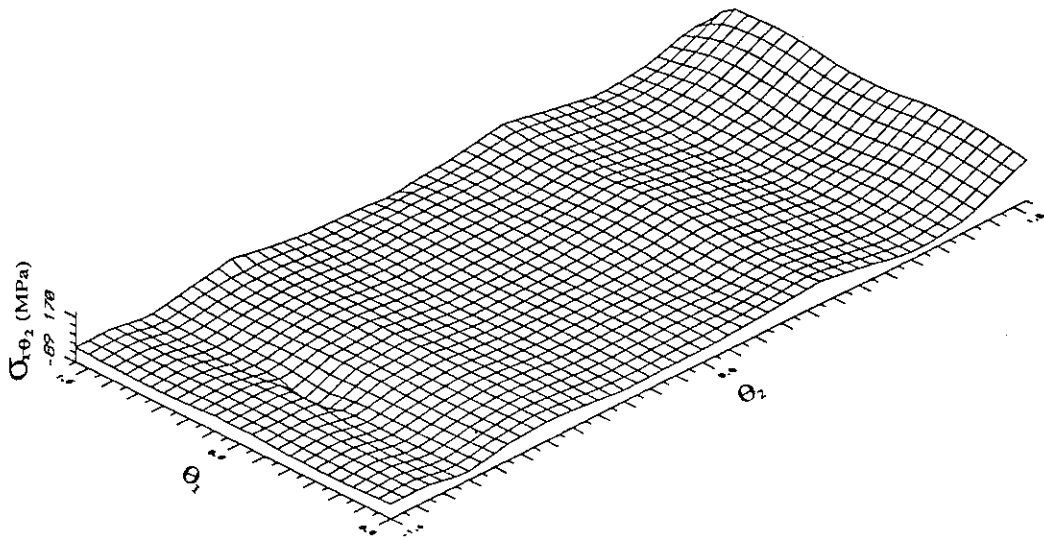


Figure 4.48: $\sigma_{r\theta_2}$ on outer surface

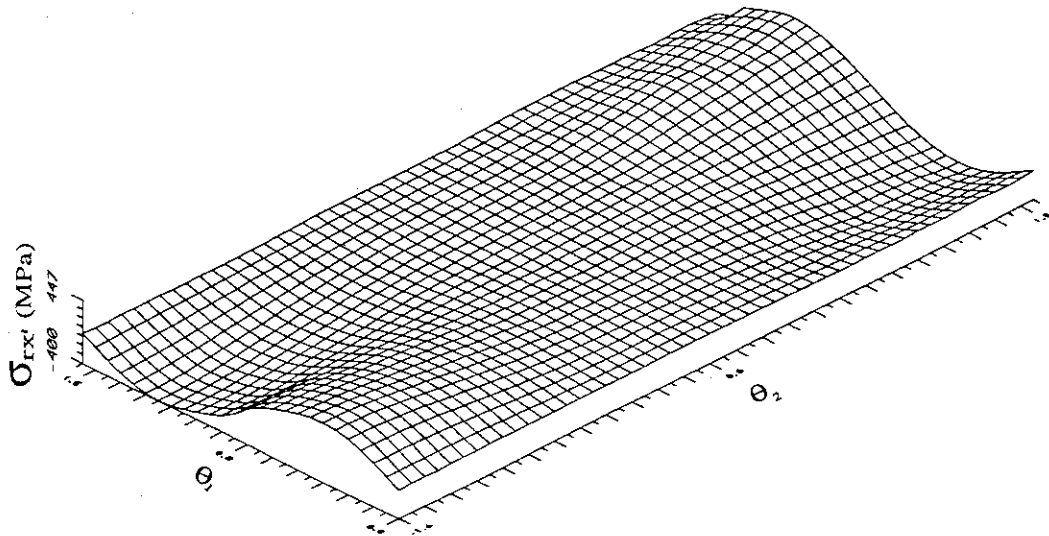


Figure 4.49: $\sigma_{rx'}$ on outer surface

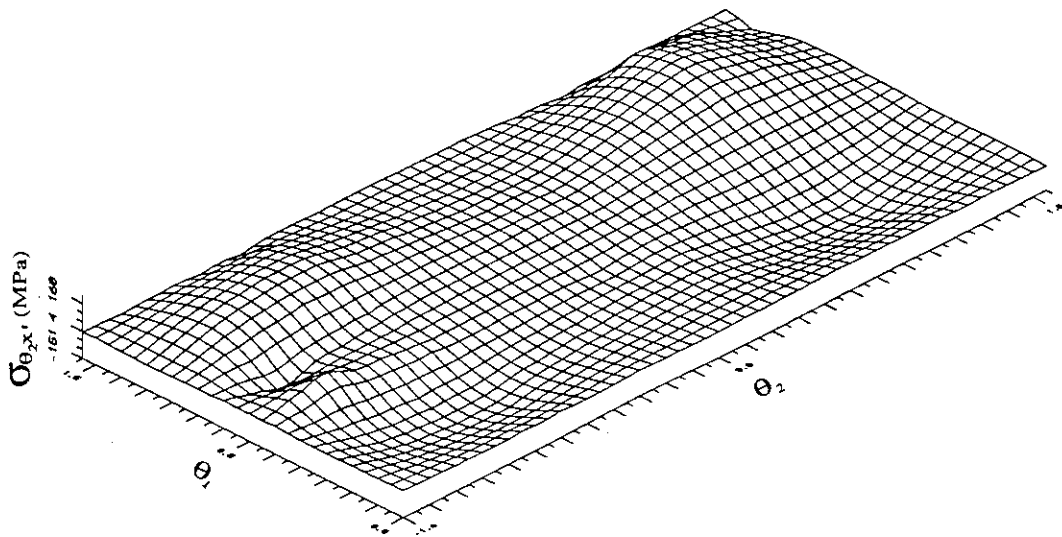


Figure 4.50: $\sigma_{\theta_2 x'}$ on outer surface

4.2.2 Adiabatic boundary conditions on outer surface

The analysis presented so far has assumed that a large thermal gradient exists across the hot leg thickness. In the real situation such thermal gradients cannot exist due to the presence of insulating material surrounding the hot leg. The aim of this insulation is to increase the thermal efficiency of the power plant by decreasing the amount of heat loss through the wall thickness to the surrounding atmosphere.

To model the effects of the insulation, it is assumed that adiabatic boundary conditions (*i.e.*, zero heat flux) exist on the outer surface of the hot leg containing a localised hot spot as shown in figure 4.32. This is an ideal case since in the real situation the heat flux will be small but finite.

For the analysis the hot leg and hot spot geometry chosen were identical to those employed in § 4.2.1. Further, with the exception of the zero heat flux boundary condition, all the remaining thermal boundary conditions and constraints were identical to those used in § 4.2.1. Furthermore, the mesh used for the analysis is the same as that shown in figure 4.33.

The resulting overall hot leg bend deformation obtained for the adiabatic boundary condition is shown in figure 4.51. The original undeformed mesh is shown drawn with a continuous

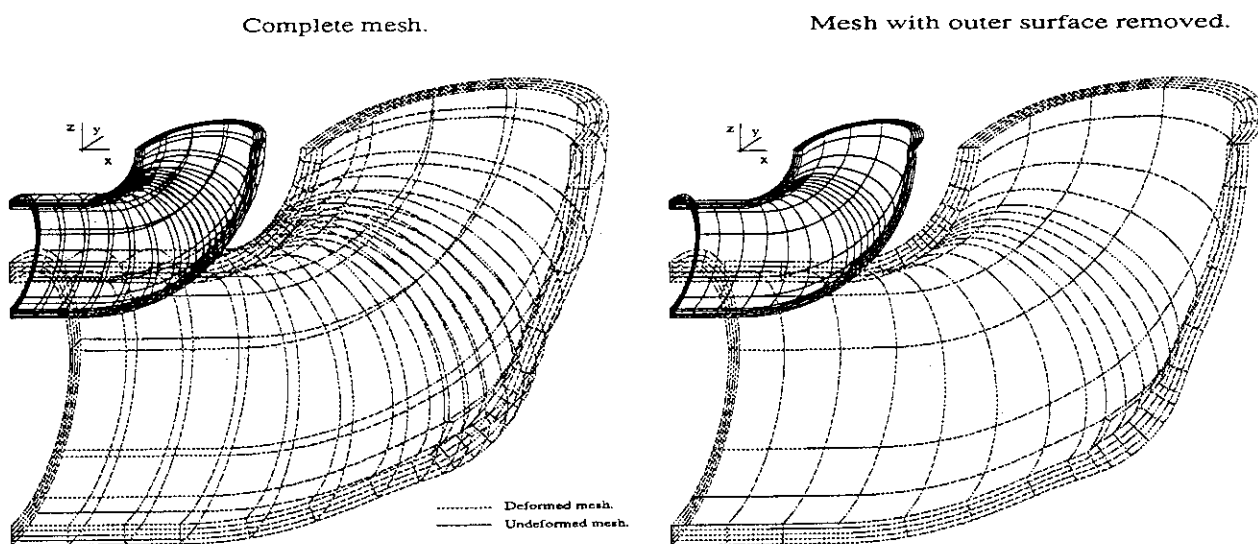


Figure 4.51: Bend deformation: adiabatic boundary condition on outer surface

line, while the deformed mesh which has been magnified by a factor of 80%, is shown drawn with a dotted line. All cross-sections far from the hot spot location experiences uniform expansion which is controlled by the imposed constraints. This is as expected since the adiabatic boundary condition reduces the temperature difference between the inner and outer wall surfaces. The uniform expansion can be realised by considering the expansion across the wall thickness; element width in the thickness direction is the same. This is in contrast to the expansion behaviour observed in the analysis (*i.e.*, § 4.2.1) in which a constant temperature was prescribed on the outer wall surface. For uniform expansion to take place it is reasonable to assume that the temperature difference between the inner and outer wall surfaces must be negligible. To verify this, the outer surface temperature variation was obtained and is plotted in figure 4.52. Notice in this figure that remote from the hot spot the surface temperature obtained is approximately 926°C which is in excellent agreement with the prescribed inner surface temperature. Further,

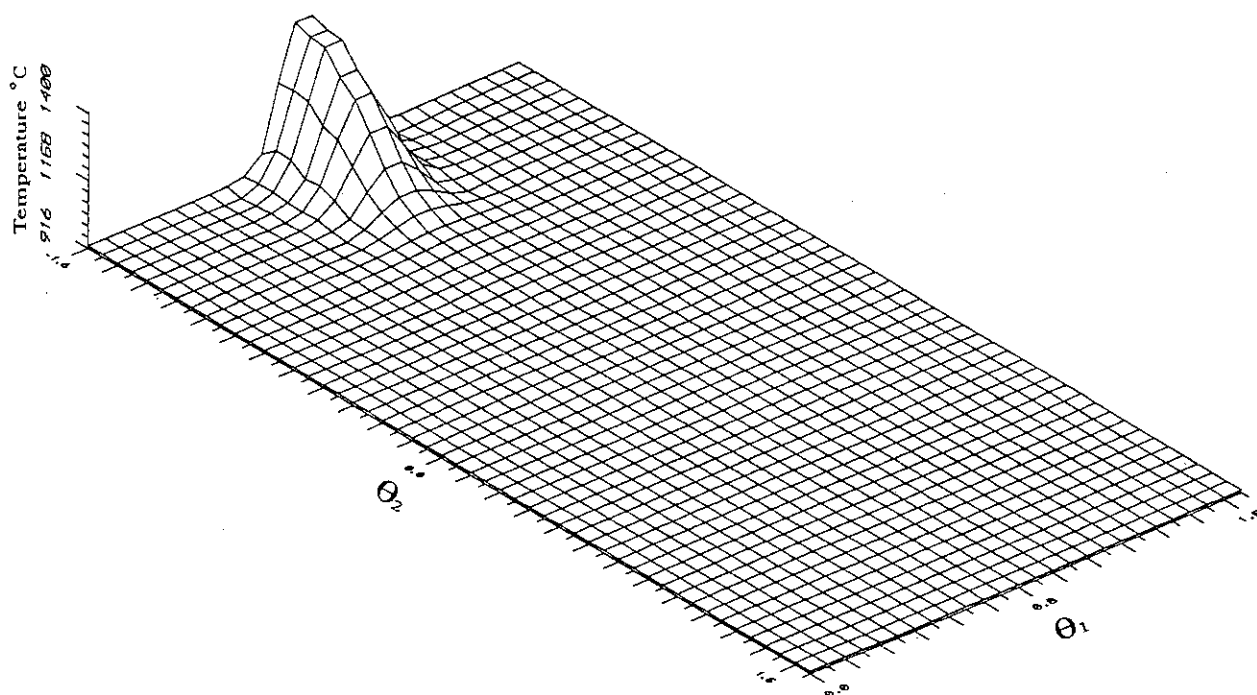


Figure 4.52: Temperature variation on outer surface

in the vicinity of the hot spot (*i.e.*, $\theta_1 = 45^\circ$ and $\theta_2 = -90^\circ$) a peak temperature of 1420°C is obtained, see figure 4.52. This is lower than the prescribed hot spot temperature (*i.e.*, 1500°C) because of heat dissipation due to variations of the temperature field in the radial r , tangential θ_2 and axial x' directions (defined in figure 4.34) in the vicinity of the hot spot.

Comparison of the bend deformations presented in figure 4.35 and figure 4.51 shows that the overall deformation is greater in the case when adiabatic boundary conditions are prescribed on the outer surface. This is due to the fact that the temperature difference between the inner and outer wall surfaces is much lower in this analysis as compared to that in § 4.2.1. Further, at the hot spot location in § 4.2.1 a swelling of the inner surface was obtained. No signs of any swelling on the outer surface were visible. In the present analysis at the vicinity of the hot spot “bulging” of the inner and outer wall surfaces is obtained, see figure 4.51. This is as expected and occurs due to the fact that a larger temperature field exists in the hot spot region relative to regions far from it. Thus, the deformation is more pronounced in the region of the hot spot when adiabatic boundary conditions are used.

In terms of the cylindrical polar coordinates defined in figure 4.34, inner surface variation of the radial U_r , tangential U_{θ_2} and axial $U_{x'}$ displacements are shown in figure 4.53, figure 4.54 and figure 4.55, respectively. Comparison of the inner surface deformations obtained in § 4.2.1 (see figures 4.36–4.38) with the present analysis shows that larger deformations occur when adiabatic boundary conditions are employed. At the site of the hot spot the radial deformation attains a maximum value which produces the observed “bulge”, see figure 4.53. The U_r variation becomes negative in the quadrant defined by $\theta_2 > 0^\circ$ due to movement of the bend axis arising from the imposed constraints and the thermal boundary conditions.

The tangential displacement (U_{θ_2}) is presented in figure 4.54. It has a similar pattern to the U_{θ_2} variation shown in figure 4.37 in § 4.2.1. The largest magnitude of U_{θ_2} occurs at $\theta_2 = 0^\circ$. At this location the solution obtained using the adiabatic boundary condition is 1.7 times greater than the corresponding solution obtained using the constant temperature boundary condition.

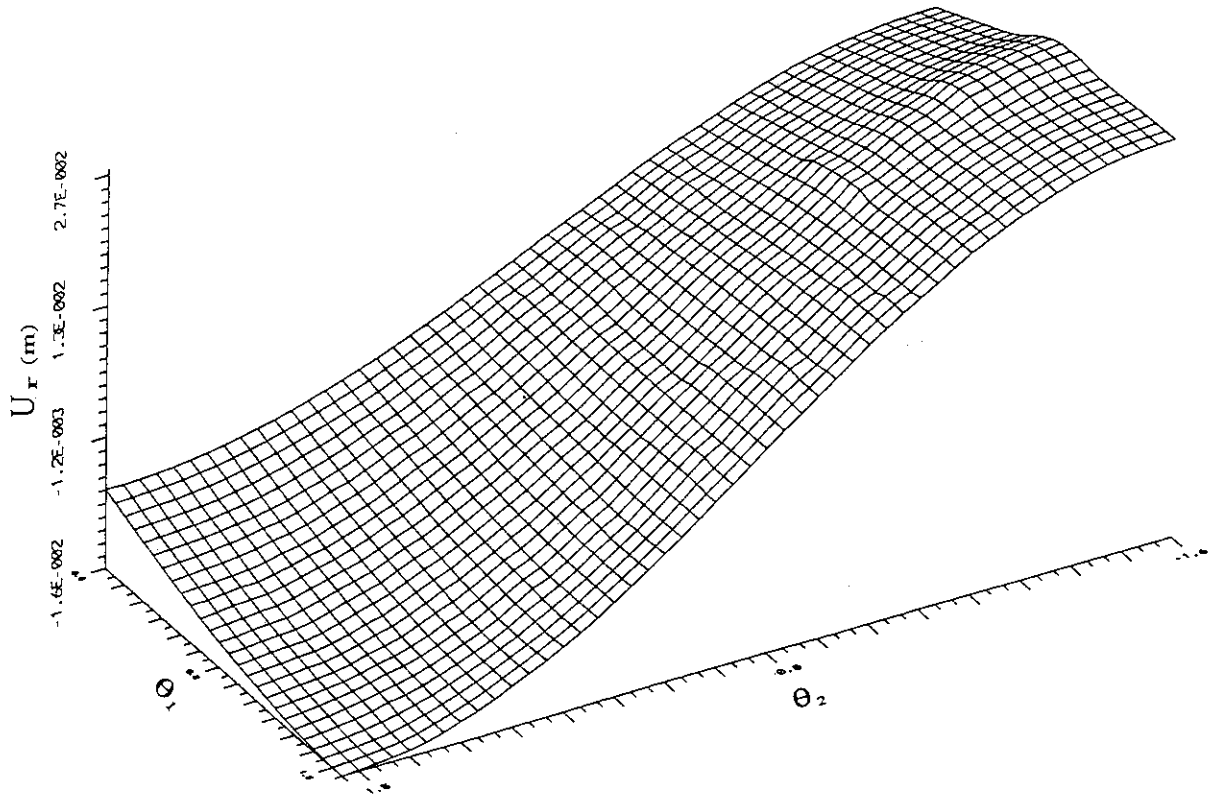


Figure 4.53: Inner surface variation of U_r

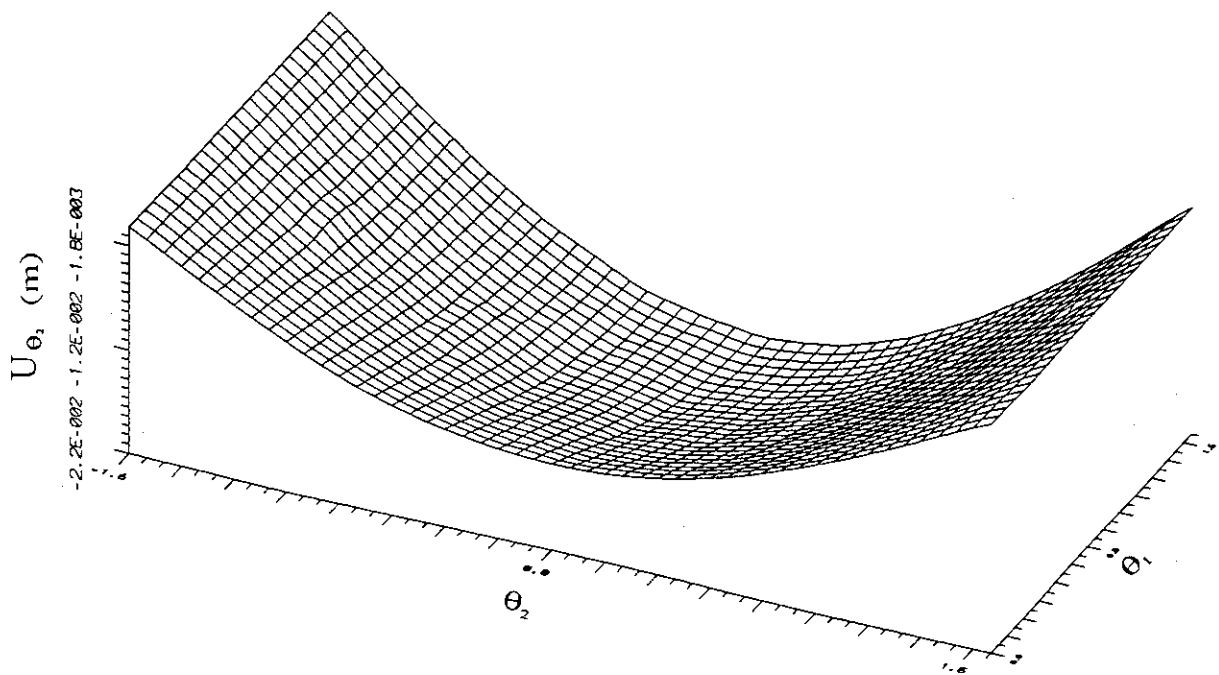
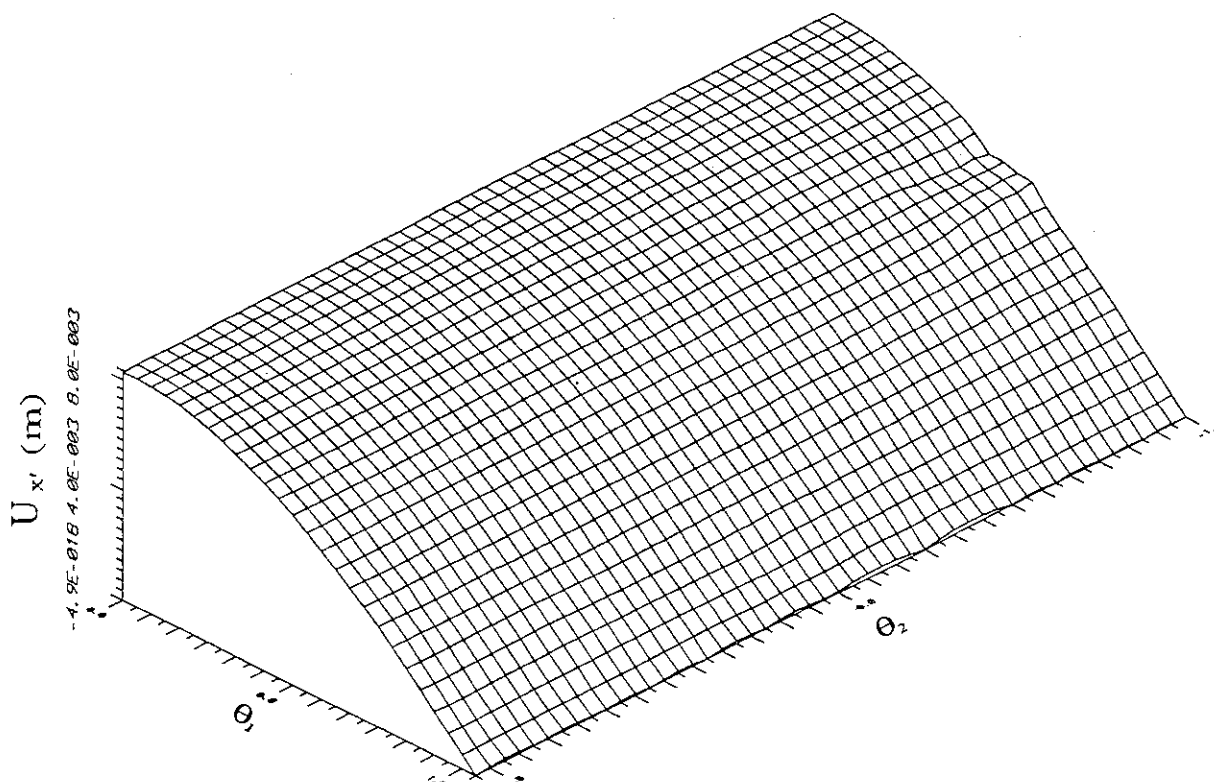


Figure 4.54: Inner surface variation of U_{θ_2}

Figure 4.55: Inner surface variation of $U_{x'}$

Adjacent to the hot spot, additional tangential deformation is also setup. The magnitude of this additional tangential deformation is much lower than that obtained in § 4.2.1. This can be seen by considering the maximum deformations at the location $\theta_1 = 45^\circ$, $\theta_2 \approx 69^\circ$ in figure 4.37 and figure 4.54.

The axial deformation shown in figure 4.55 essentially follows the same pattern as that obtained in § 4.2.1 (see figure 4.38), except that it is approximately 1.7 times larger at the maximum variation, which is obtained at $\theta_1 = 0^\circ$. This larger variation occurs since the temperature difference across the wall thickness is much smaller in comparison to that obtained in § 4.2.1.

In terms of cylindrical polar coordinates (r, θ_2, x') the radial σ_{rr} , tangential $\sigma_{\theta_2\theta_2}$ and axial $\sigma_{x'x'}$ stresses on the inner surface are shown in figure 4.56, figure 4.57 and figure 4.58 respectively. As expected σ_{rr} is negligible in comparison with $\sigma_{\theta_2\theta_2}$ and $\sigma_{x'x'}$. The maximum variations of $\sigma_{\theta_2\theta_2}$ and $\sigma_{x'x'}$ at the spot location are -1483MPa and -1533MPa, respectively. Far from hot spot these variations are extremely small. This is mainly due to the fact that the difference between the inner and outer surface temperatures is negligible, thus stresses cannot be established.

The shear stresses $\sigma_{r\theta_2}$, $\sigma_{rx'}$ and $\sigma_{\theta_2x'}$ on the inner surface are plotted in figures 4.59, figures 4.60 and figure 4.61, respectively. Relative to the direct stresses the shear stresses remote from the hot spot location are extremely small and can be considered to be zero since the temperature difference across the wall thickness is negligible. In the vicinity of the hot spot $\sigma_{r\theta_2}$ is tensile with a maximum value of 22MPa, and $\sigma_{rx'}$ has tensile and compressive maximum variations of 64MPa and -80MPa, respectively. The largest shear stress occurs for $\sigma_{\theta_2x'}$. It has tensile and compressive variations of 541MPa and -548MPa, respectively. Thus, all the shear stresses are increased in magnitude in the vicinity of the hot spot.

The outer surface variation of the direct stresses σ_{rr} , $\sigma_{\theta_2\theta_2}$ and $\sigma_{x'x'}$ are shown in fig-

ure 4.62, figure 4.63 and figure 4.64 respectively. Remote from the hot spot region both $\sigma_{\theta_2\theta_2}$ and $\sigma_{x'x'}$ are essentially zero. In the vicinity of the hot spot a sinusoidal decay of $\sigma_{\theta_2\theta_2}$ in both the θ_1 and θ_2 directions is obtained. This sinusoidal variation is not symmetrical about $\theta_1 = 45^\circ$ because the bend geometry under investigation, together with prescribed boundary conditions is not symmetrical about $\theta_1 = 45^\circ$. Consequently, the non-symmetrical variation arises because the prescribed axial constraint at $z = 0.0m$ is closer to the hot spot than the prescribed axial constraint at $x = -0.5m$. The observed sinusoidal variation is possibly due to the decay of outer surface temperature in the θ_1 and θ_2 directions as shown in figure 4.52. The maximum tensile variation of $\sigma_{\theta_2\theta_2}$ along the edge $\theta_2 = -90^\circ$ is approximately 210MPa, see figure 4.63. For $\sigma_{x'x'}$ the maximum tensile variation is approximately 300MPa.

The surface shear stresses $\sigma_{r\theta_2}$, $\sigma_{rx'}$ and $\sigma_{\theta_2x'}$ are shown in figures 4.65, figures 4.66 and figure 4.67, respectively. These are all zero at large distances from the hot spot. In the vicinity of the hot spot $\sigma_{r\theta_2}$ attains a maximum tensile variation of 20MPa. The variation of $\sigma_{rx'}$ is rather complex and varies within ± 47 MPa. For $\sigma_{\theta_2x'}$ (see figure 4.67) the maximum tensile and compressive values are 388MPa and -428MPa, respectively.

As in § 4.2.1 tensile stresses are generated on the outer surface in the vicinity of the hot spot. These stresses, although much smaller in magnitude, can still increase the possibility of crack formation since it is known that cracking occurs at sites of high stress elevations.

4.3 Conclusions

For the hot leg, analysis shows that the solution is very sensitive to the type of thermal boundary conditions prescribed on the inner and outer surfaces. In the analyses (§ 4.1 and § 4.2.1) for which the inner surface, outer surface and hot spot severe accident temperatures were 926° , 150° and 1500° , respectively, non uniform expansion across the hot leg thickness was obtained. This effect was most predominate on the inner surface, especially at the hot spot location where surface swelling was obtained. However, even after a magnification of the deformation by a factor of 80%, no visible swelling (§ 4.2.1) was observed on the outer surface. This behaviour is reasonable since maximum deformation would be expected at the site of maximum temperature (*i.e.*, hot spot location). Further, since the outer wall temperature is considerably lower than both the inner wall and hot spot temperatures then it is also reasonable to expect the outer surface to deform less than the inner. The non uniform expansion produced large stresses and strains, with peak variations in the hot spot region.

When an adiabatic boundary condition (§ 4.2.2) was prescribed on the outer surface (all other boundary conditions were the same as in the constant temperature case, *i.e.*, § 4.2.1) a uniform expansion across the hot leg thickness was obtained, which resulted in zero stresses being produced. This variation is reasonable since the difference in the inner and outer surface temperature was negligible, except at the location of the hot spot. At the hot spot location bulging of the inner and outer surface was obtained due to the maximum temperature variation through the thickness direction, resulting in the generation of peak stresses. Comparisons between the outer surface direct stresses for the constant temperature analysis and the adiabatic boundary condition shows that in the locality of the hot spot much larger stresses can be expected for the constant temperature case. This behaviour is reasonable since in the former case the temperature difference across the wall thickness is much larger.

The large strain and stress variations obtained in the analysis conducted are a direct consequence of the large magnitudes of the severe accident temperatures prescribed and of the limitations of the steady state thermoelastic model employed. At these exceedingly high temperatures the yield strains and stresses are not defined. In the real situation plasticity effects will also be present and these will redistribute the strains and stresses such that these are never greater than their yield values.

In all the analysis conducted, at the location of the hot spot on the inner surface large compressive direct stresses were obtained. On the outer surface at the same location, large tensile direct stresses were obtained. From a structural integrity point of view, presence of these large stress elevations in the vicinity of the hot spot could be detrimental. The tensile stresses are extremely important since they can act as sites of crack initiation and subsequent propagation. Further, if a crack like defect is already present prior to the formation of the hot spot then it is possible that once a hot spot is formed the elevated tensile stresses could lead to its propagation. Once a crack propagates through the thickness, leak worthiness of the hot leg comes into question.

Comparisons of the outer surface direct stresses obtained for the constant temperature analysis (§ 4.2.1) and between the adiabatic boundary condition (§ 4.2.2) shows that in the vicinity of the hot spot much larger stresses can be expected for the constant temperature case. This is reasonable since in the former case (*i.e.*, § 4.2.1) the temperature difference across the wall thickness is much larger and the resulting non uniform deformation generates large stresses.

Regarding the use of shell elements it is worth mentioning that these elements would not be suitable when non uniform, through the thickness deformation is expected in the analysis (*i.e.*, § 4.1 and § 4.2.1). These elements can be employed when the thermal boundary conditions are expected to produce uniform expansion across the thickness. Therefore, when the temperature difference between the inner and outer walls is negligible, as in § 4.2.2, shell elements can be used. At the hot spot location the difference between the inner and outer wall temperatures is not negligible, thus, in this region it may be appropriate to use elements that allow three-dimensional modelling. Further, transition elements must be employed to couple the shell elements with the elements used in the three-dimensional modelling region.

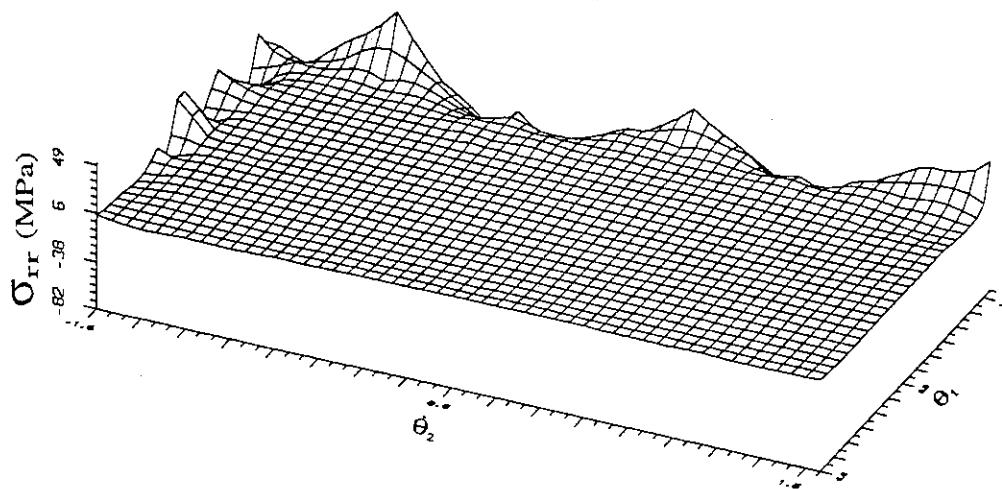


Figure 4.56: σ_{rr} on inner surface

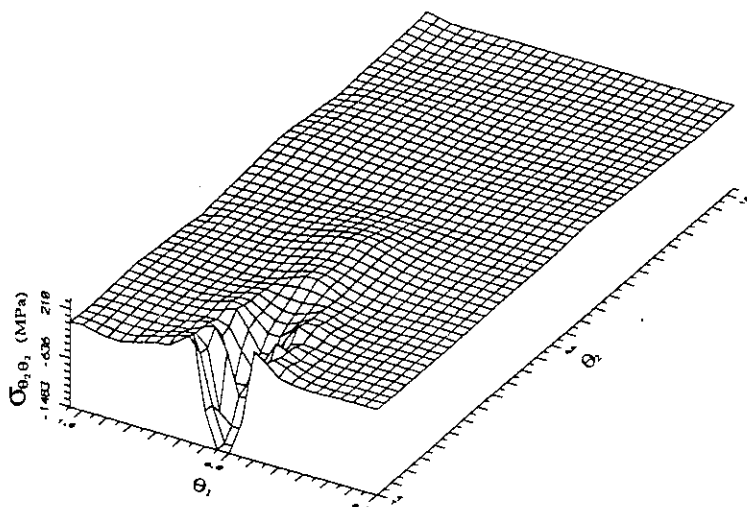


Figure 4.57: $\sigma_{\theta_2\theta_2}$ on inner surface

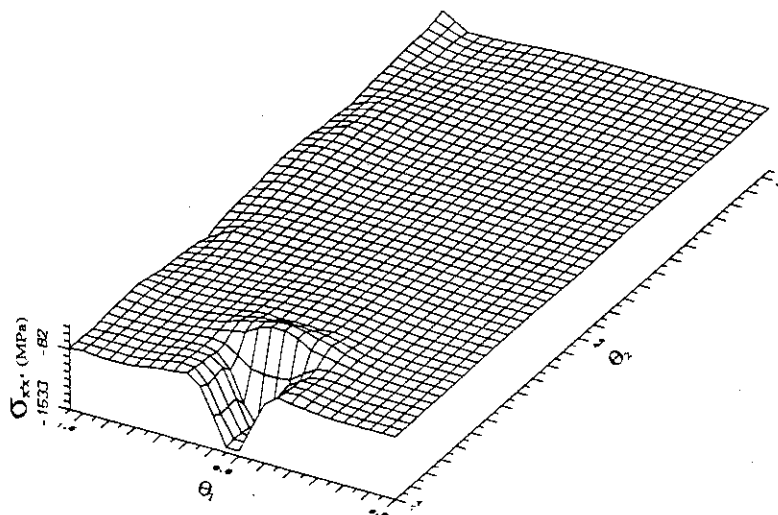


Figure 4.58: $\sigma_{x'_i x'_i}$ on inner surface

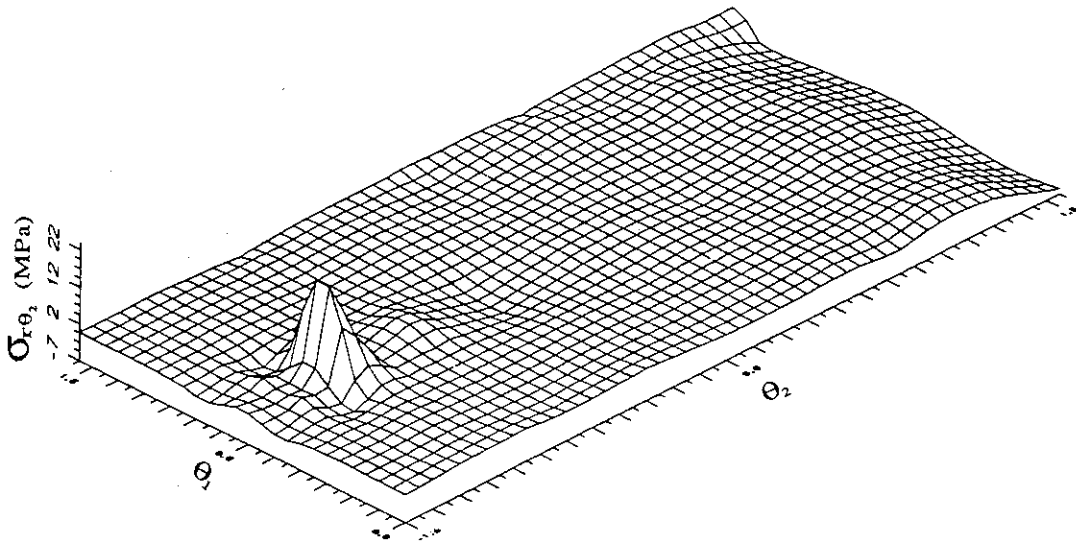


Figure 4.59: $\sigma_{r\theta_2}$ on inner surface

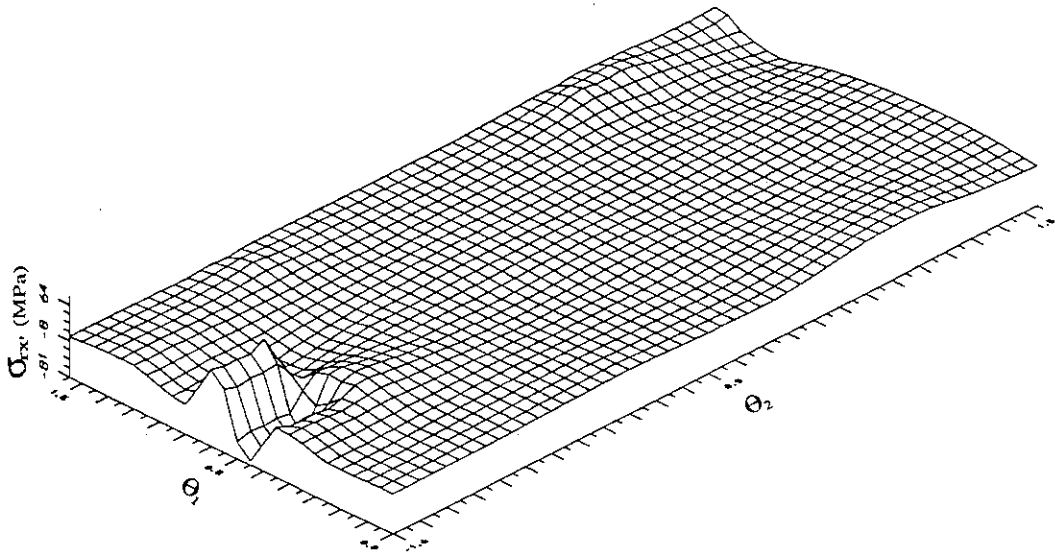


Figure 4.60: $\sigma_{r_x'}$ on inner surface

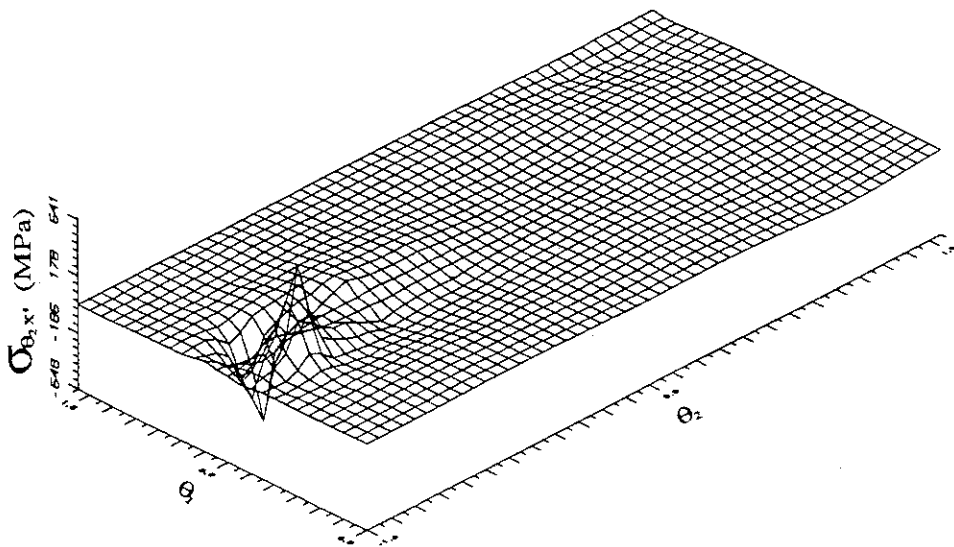


Figure 4.61: $\sigma_{\theta_2 x'}$ on inner surface

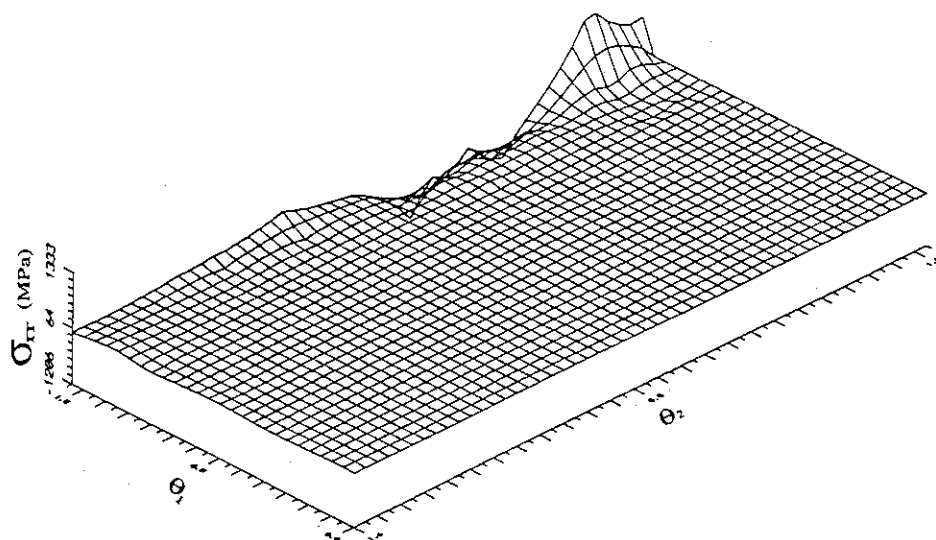


Figure 4.62: σ_{rr} on outer surface

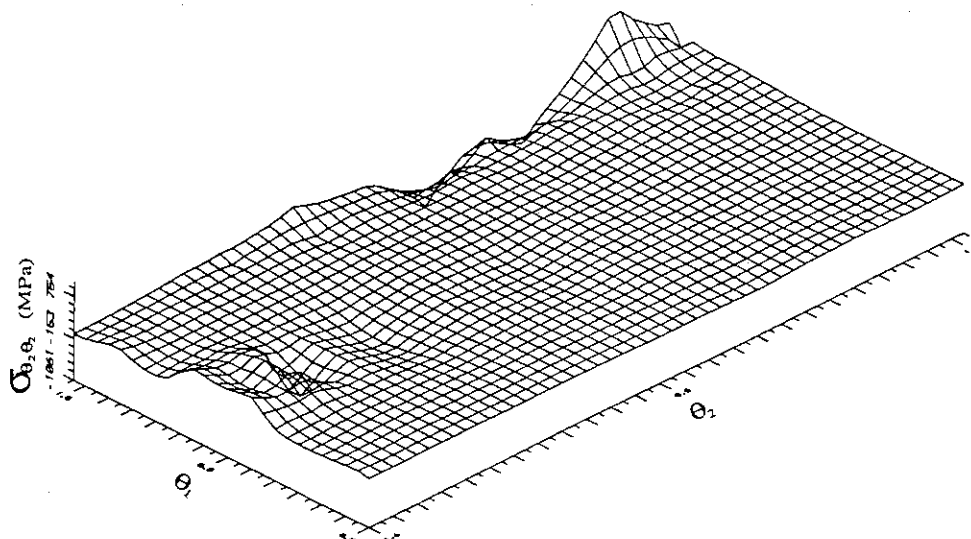


Figure 4.63: $\sigma_{\theta_2\theta_2}$ on outer surface

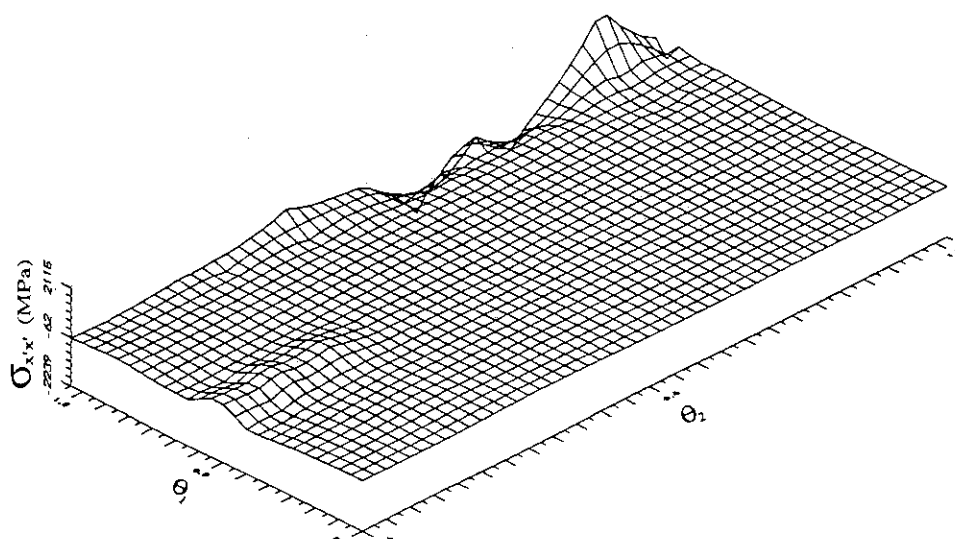


Figure 4.64: $\sigma_{x'x'}$ on outer surface

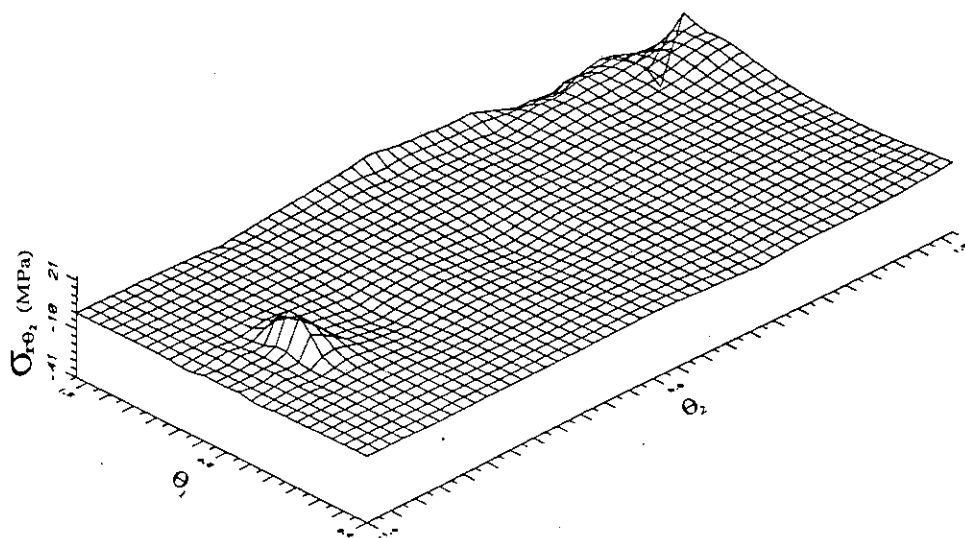


Figure 4.65: $\sigma_{r\theta_2}$ on outer surface

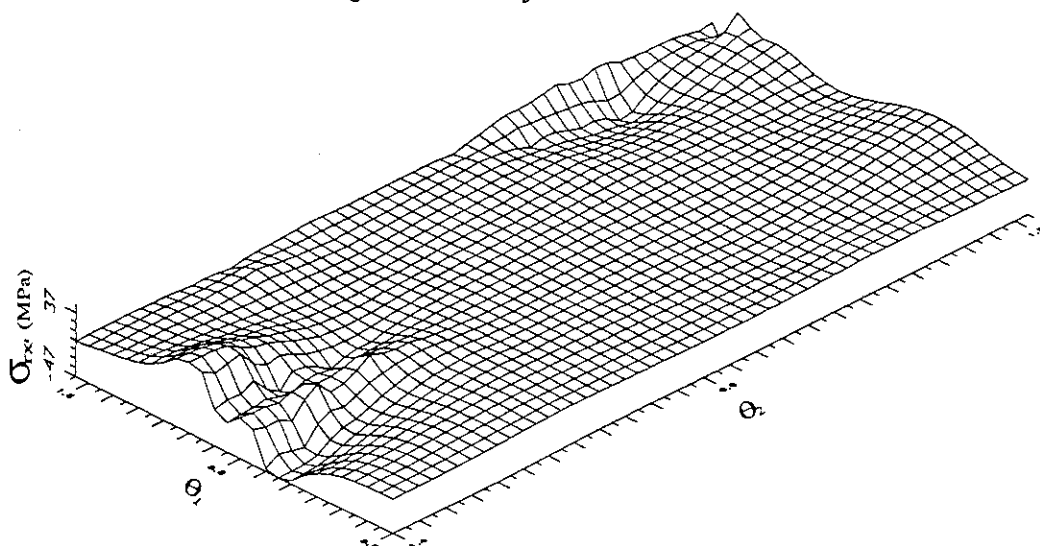


Figure 4.66: $\sigma_{rx'}$ on outer surface

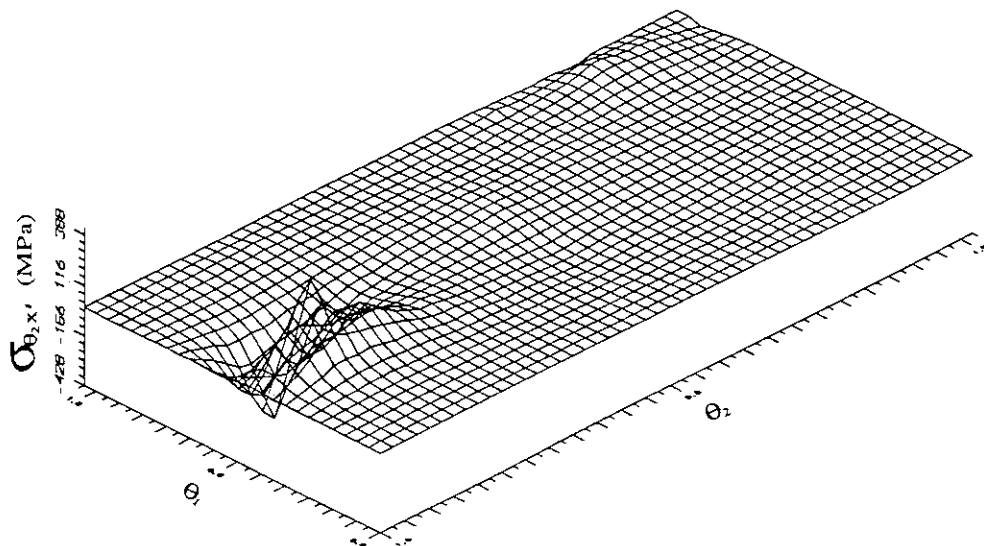


Figure 4.67: $\sigma_{\theta_2 x'}$ on outer surface

Chapter 5

Final Conclusions

A three-dimensional steady state thermoelastic analysis has been conducted on a slightly modified geometry of the hot leg of a pressurized water reactor (PWR) containing localised hot spots resulting from fission product aerosol deposition occurring during a hypothetical severe accident. The boundary element method (BEM) was selected as the numerical solution technique. The following conclusions can be drawn from the present analysis:

1. Solution convergence can be realised provided sufficiently large number of elements are employed and correct modelling of the temperature transition region (TTR) adjacent to the hot spot on the inner surface is conducted. The only correct temperature field across the TTR is that which can be represented by the interpolation functions employed in the BEM code. Further, incorrect solutions can also be generated if the TTR is too thin.
2. Non uniform expansion across the hot leg thickness was obtained in the analysis for which the temperature difference across the thickness was large. This was most predominate on the inner surface, especially at the hot spot location where surface swelling was obtained. However, even after a magnification of the deformation by a factor of 80%, in the bend section analysis, no visible swelling was observed on the outer surface. This behaviour is reasonable since maximum deformation would be expected at the site of maximum temperature (*i.e.*, hot spot location). Further, since the outer wall temperature is considerably lower than both the inner wall and hot spot temperatures then it is also reasonable to expect the outer surface to deform less than the inner.
3. When an adiabatic boundary condition was prescribed on the outer surface a uniform expansion across the hot leg thickness was obtained. At the hot spot location bulging of the inner and outer surface was obtained. This behaviour is reasonable since the adiabatic boundary conditions gives rise to outer wall temperature which is almost the same as the inner surface temperature. Consequently, a maximum temperature variation through the thickness was obtained in the vicinity of the hot spot which produced the bulging observed.
4. In the locality of the hot spot, direct stresses are much larger when a constant temperature (considerably less than inner surface temperature) is prescribed on the outer surface than when an adiabatic boundary condition is prescribed.
5. The large strain and stress variations obtained are a direct consequence of the large magnitudes of the severe accident temperatures prescribed and of the limitations of the steady state thermoelastic model employed. At these exceedingly high temperatures the yield strains and stresses are not defined.
6. In all the analysis conducted, at the location of the hot spot on the inner surface large compressive stresses were obtained. On the outer surface at the same location, large

tensile stresses were obtained. The presence of these large stress elevations in the vicinity of the hot spot could be detrimental to the integrity of the hot leg. The tensile stresses are extremely important since they can act as sites of crack initiation and subsequent propagation. Further, if a crack like defect is already present prior to the formation of the hot spot then it is possible that once a hot spot is formed the elevated tensile stresses could lead to its propagation. Once a crack propagates through the thickness, leak worthiness of the hot leg comes into question.

Since the analysis conducted has been based on steady state thermoelasticity it is difficult to draw firm conclusions on the integrity of the hot leg. Consequently, additional analysis must be conducted that includes the effects of plasticity and the effects of temperature on the material properties.

Acknowledgements

The authors would like to express their profound gratitude and indebtedness to Dr. Toshikuni Isozaki from JAERI for his invaluable advice and many fruitful discussions. Sincere thanks are due to Prof. M. Tanaka and Dr. T. Matsumoto from Shinshu University for their advice on the use of the 3D thermal stress analysis code.

Bibliography

- [1] Abe, K., Sugimoto, J. and Kajimoto, M., “Uncertainties Still Remaining in Severe Accident Research Activities at JAERI” to appear in *Nuclear Engng. Design.*, 1994.
- [2] Boley, B. A. and Weiner, J. H., *Theory of Thermal Stresses*, John Wiley and Sons, New York, 1960.
- [3] Zienkiewicz, O. C., *The Finite Element Method*, Third Edition, McGraw-Hill Book Company (UK) Limited, 1977.
- [4] Brebbia, C. A. and Dominguez, J., *Boundary Elements—An Introductory Course*, Computational Mechanics Publications and McGraw-Hill Book Company, 1989.
- [5] Matsumoto, T. and Tanaka, M., “An Alternative Discretization Technique for Regularized Boundary Integral Equations”, Proc. of BTEC-91, JASCOME, June 18 1991, Japan.
- [6] Brebbia, C. A., Telles, J. F. C. and Wrobel, L. C., *Boundary Element Techniques*, Springer-Verlag, Berlin and New York, 1984.
- [7] J. C. Lachat and J. O. Watson, “Effective Numerical Treatment of Boundary Integral Equation: A Formulation for Three-Dimensional Elastostatics”, *Int. J. Numer. Methods Engng.*, vol. 10, pp. 991-1005, 1976.
- [8] M. Kajimoto *et. al.*, Development of THALES-2, a Computer Code for Coupled Thermal-hydraulics and FP Transport Analysis for Severe Accident at LWR's and its Application to Analysis of FP Revaporization, Proc. Internat. Topical Mtg. on Safety of Thermal Reactors, Portland, Oregon, (1991), 584-592.

Appendix A

Analytical & Numerical Solution

A.1 Analytical Solution

Consider a pipe of length L , inner radius r_i and outer radius r_o . Let the inner surface be subjected to a uniform pressure P_i and uniform temperature T_i . The outer surface is at temperature T_o . The pipe is characterised by Young's modulus E , Poisson's ratio ν and thermal conductivity α . If the ratio $L/r_o \gg 1$ and if axial displacements are prevented, the problem is essentially one of plane strain. For this case, Boley and Weiner [2] have shown that the general solution in cylindrical coordinates is of the form,

$$U(r) = \frac{\alpha(1+\nu)}{(1-\nu)r} \int_{r_i}^r T(r)rdr + Ar + \frac{B}{r} \quad (\text{A.1})$$

for the radial displacement. The term $T(r)$ represents the temperature variation across the thickness of the pipe. The stresses can be obtained from the strain-displacement relations and Hooke's law as

$$\sigma_{rr} = -\frac{\alpha E}{(1-\nu)r^2} \int_{r_i}^r T(r)rdr + \frac{AE}{(1+\nu)(1-2\nu)} - \frac{BE}{(1+\nu)r^2}, \quad (\text{A.2})$$

$$\sigma_{\theta\theta} = \frac{\alpha E}{(1-\nu)r^2} \int_{r_i}^r T(r)rdr - \frac{\alpha ET(r)}{(1-\nu)} + \frac{AE}{(1+\nu)(1-2\nu)} + \frac{BE}{(1+\nu)r^2} \quad (\text{A.3})$$

and

$$\sigma_{r\theta} = 0. \quad (\text{A.4})$$

The constants A and B must be determined from the boundary conditions. Thus substituting $\sigma_{rr} = -P_i$ at $r = r_i$ and $\sigma_{rr} = 0$ at $r = r_o$ into equation A.2 gives

$$A = \frac{\alpha(1+\nu)(1-2\nu)}{(1-\nu)(r_o^2 - r_i^2)} \int_{r_i}^{r_o} T(r)rdr + \frac{(1+\nu)(1-2\nu)}{E} \frac{P_i r_i^2}{r_o^2 - r_i^2} \quad (\text{A.5})$$

and

$$B = \frac{\alpha(1+\nu)r_i^2}{(1-\nu)(r_o^2 - r_i^2)} \int_{r_i}^{r_o} T(r)rdr + \frac{(1+\nu)}{E} \frac{P_i r_i^2 r_o^2}{r_o^2 - r_i^2}. \quad (\text{A.6})$$

Hence the final expressions for the radial displacement becomes

$$U(r) = \frac{\alpha(1+\nu)}{(1-\nu)r} \left\{ \int_{r_i}^r T(r)rdr + \frac{(1-2\nu)r^2 + r_i^2}{r_o^2 - r_i^2} \int_{r_i}^{r_o} T(r)rdr \right\} + \frac{P_i r_i^2 (1+\nu)}{E(r_o^2 - r_i^2)r} [(1-2\nu)r^2 + r_o^2]. \quad (\text{A.7})$$

A.2 Numerical Solution

The influence of the hot spot on the structural response of the hot leg should diminish as the distance from the hot spot increases. Thus, far from the hot spot the structural response of the hot leg is governed by the uniform pressure and temperature boundary conditions prescribed. In this region the structural response must be similar to a pipe (without hot spot) with identical boundary conditions.

In order to check this, a straight section of the hot leg (without hot spot) was analysed subjected to the same temperature and pressure boundary conditions as presented in § 4.1. The geometrical dimensions considered are identical to those in § 4.1. Without the presence of the hot spot the problem contains another plane of symmetry. Thus only 1/8 of the original hot leg needs to be modelled with appropriate boundary conditions on the symmetry planes. Three meshes were designed, as shown in figure A.1, containing 77, 348 and 424 elements with 654, 3138 and 3822 degrees of freedom, respectively.

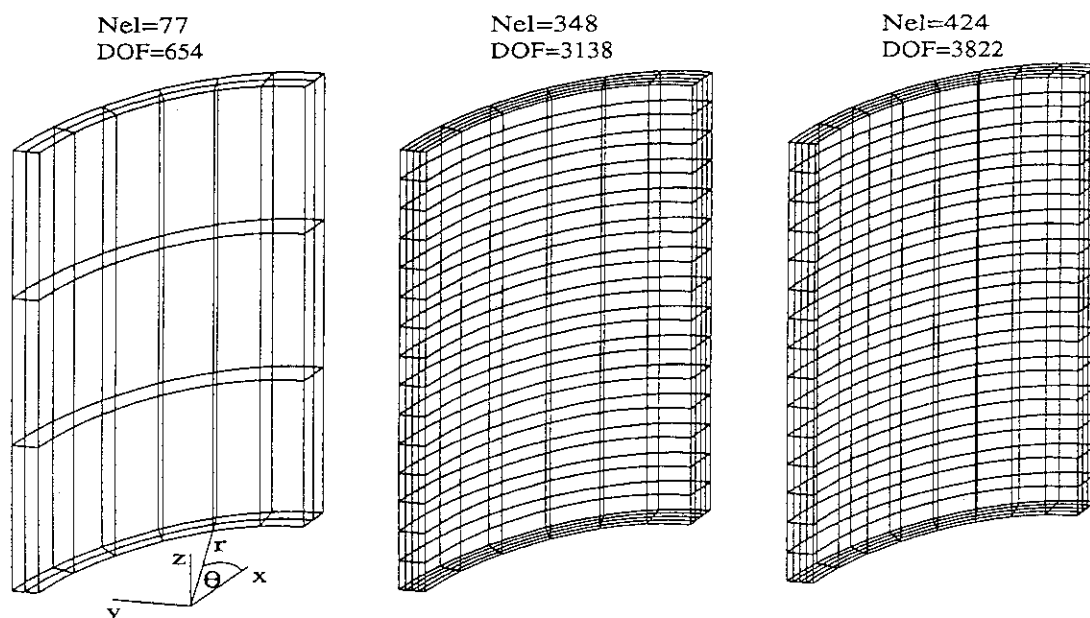


Figure A.1: Mesh refinement for 1/8 modelling of Hot leg.

To compare the analytical solutions with the numerical solutions it is necessary to establish a relationship for the temperature variation (*i.e.*, $T(r)$ in § A.1) across the thickness of the hot leg. This relationship was obtained by plotting the nodal temperature against the radial distance r , on the x - z plane at $z = 1.0m$. This plot is shown in figure A.2. A logarithmic curve was fitted through the data points allowing the temperature variation to be expressed as

$$T(r) = -4876.82 \times \ln r - 3946.5 \quad (\text{A.8})$$

across the thickness. By employing $T(r)$ in equation A.7 the variation of the radial displacement across the thickness was calculated. The analytic solution together with the numerical displacement solutions for the three meshes is presented in figure A.3. All the numerical solutions are in good agreement with the analytic solution. Essentially all the three meshes generate the same solutions over the range of r considered. The solutions obtained using the coarse mesh (*i.e.*, 77 elements) and the most refined mesh (*i.e.*, 424 elements) differ by less than 0.06%. The solution obtained using the intermediate mesh (*i.e.*, 348 elements) falls in between the coarse and most refined mesh solutions. This indicates that the solution is converging. The maximum difference between the analytical solution (*i.e.*, equation A.7) and the three meshes employed is 0.3% over the entire thickness.

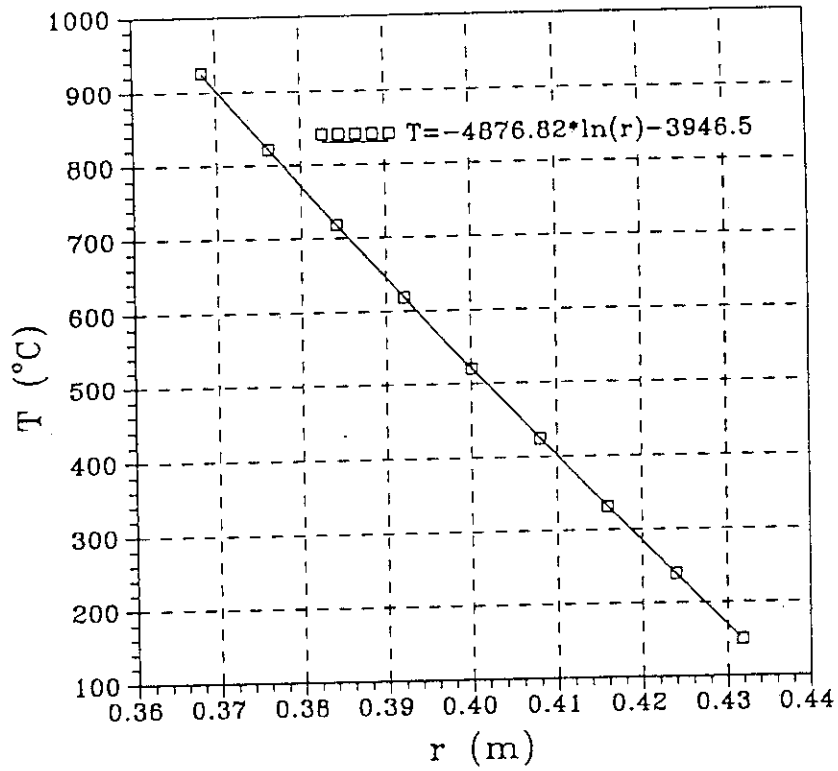


Figure A.2: Temperature variation across thickness.

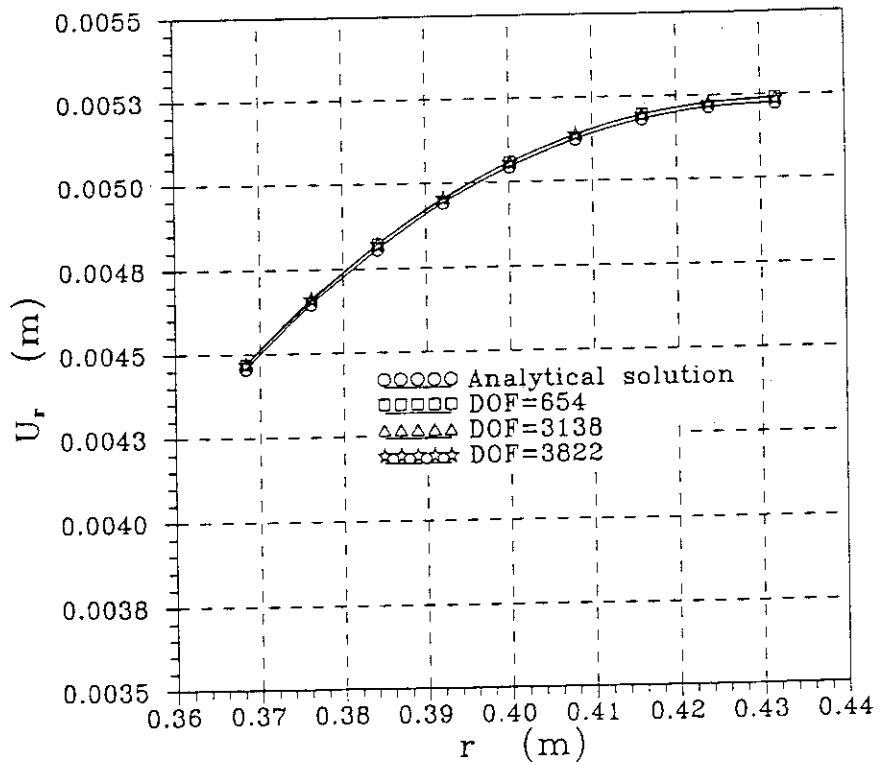


Figure A.3: Analytic and numerical solutions.

Appendix B

Transformations

With reference to figure 4.34 the transformations required to derive the displacements and strains (same for stresses) in cylindrical polar coordinates (r, θ_2, x') from the original cartesian coordinates (x, y, z) are presented below.

B.1 Displacements

In the first rotation about the y -axis the coordinate system (x, y, z) is transformed into (x', y', z') as shown in figure B.1 diagram A. The y -axis in figure B.1 points into the plane of the page. For this transformation the positive sense of the angle θ , measured relative to the z -axis is in the direction shown (*i.e.*, from z to x). In the bend section analysis (see figure 4.34) rotation of each plane perpendicular (*i.e.*, $y'-z'$ plane) to the hot leg axis takes place in the negative direction as shown in figure B.1 diagram B. Thus, a rotation through an angle θ_1 (see figure B.1

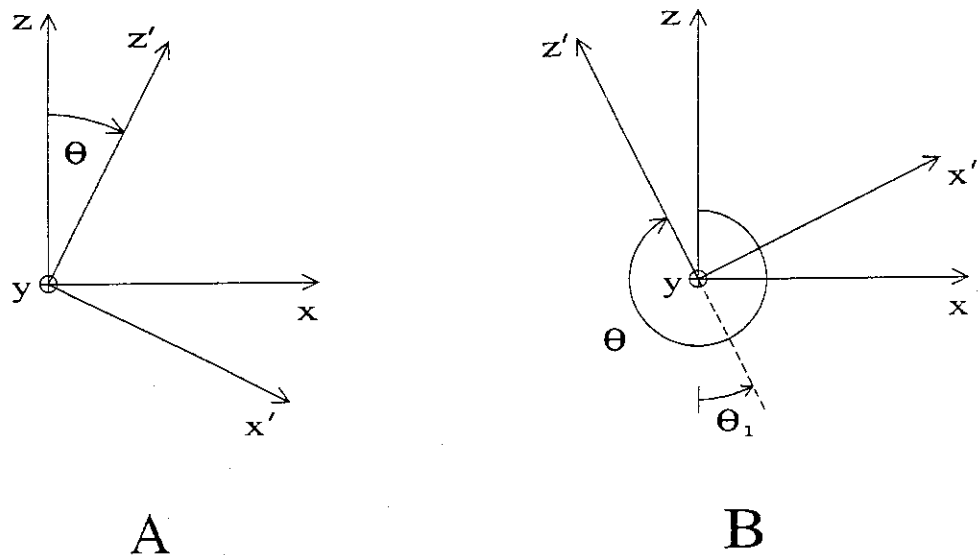


Figure B.1: Rotation about y axis.

diagram B) measured relative to the $-z$ axis corresponds to a positive rotation through angle θ measured relative to the $+z$ axis. The angle needed for the first transformation is defined in equation B.1.

$$\theta = 2\pi - \theta_1 \tag{B.1}$$

As the coordinate system (x', y', z') rotates about the y -axis the angle θ_1 varies within the range $0^\circ \leq \theta_1 \leq 90^\circ$.

The cylindrical polar coordinates (r, θ_2, x') centered on the hot leg axis are obtained from the cartesian coordinates (y', z', x') , see figure B.2. In figure B.2 the x' axis is pointing out of

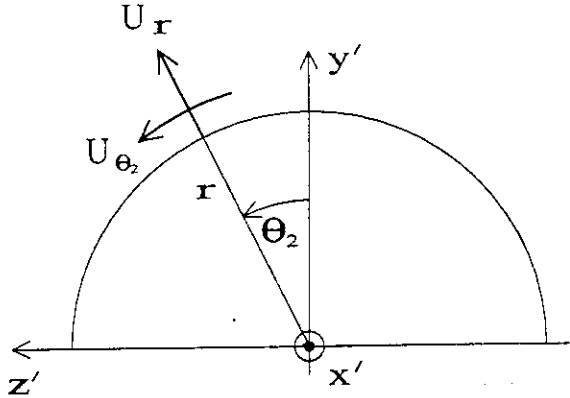


Figure B.2: Definition of cylindrical polar coordinates.

the plane of the page and is directed along the bend axis. The angle θ_2 is measured relative to the y' axis and has positive direction from y' to z' . At any $y'-z'$ plane θ_2 is defined such that $-90^\circ \leq \theta_2 \leq 90^\circ$.

Using the sequence of transformations mentioned above the radial, tangential and axial deformations defined as U_r , U_{θ_2} and $U_{x'}$, respectively, in the cylindrical polar coordinate system (r, θ_2, x') can be expressed as

$$U_r = U_x \sin \theta \sin \theta_2 + U_y \cos \theta_2 + U_z \cos \theta \sin \theta_2 \quad (\text{B.2})$$

$$U_{\theta_2} = U_x \sin \theta \cos \theta_2 - U_y \sin \theta_2 + U_z \cos \theta \cos \theta_2 \quad (\text{B.3})$$

$$U_{x'} = U_x \cos \theta - U_z \sin \theta. \quad (\text{B.4})$$

In equations B.2-B.4 components of the deformation in the original coordinate system (x, y, z) are represented by U_x , U_y and U_z .

B.2 Strains

With respect to the rotations defined in § B.1 the strain components in the cylindrical polar coordinate system (r, θ_2, x') as functions of the original cartesian coordinates (x, y, z) can be expressed as

$$\begin{aligned} \varepsilon_{rr} = & \varepsilon_{xx} \sin^2 \theta \sin^2 \theta_2 + \varepsilon_{xy} \sin \theta \sin 2\theta_2 + \varepsilon_{xz} \sin 2\theta \sin^2 \theta_2 + \varepsilon_{yy} \cos^2 \theta_2 + \\ & \varepsilon_{yz} \cos \theta \sin 2\theta_2 + \varepsilon_{zz} \cos^2 \theta \sin^2 \theta_2 \end{aligned} \quad (\text{B.5})$$

$$\begin{aligned} \varepsilon_{r\theta_2} = & 0.5\varepsilon_{xx} \sin^2 \theta \sin 2\theta_2 + \varepsilon_{xy} \sin \theta \cos 2\theta_2 + 0.5\varepsilon_{xz} \sin 2\theta \sin 2\theta_2 - 0.5\varepsilon_{yy} \sin 2\theta_2 + \\ & \varepsilon_{yz} \cos \theta \cos 2\theta_2 + 0.5\varepsilon_{zz} \cos^2 \theta \sin 2\theta_2 \end{aligned} \quad (\text{B.6})$$

$$\begin{aligned} \varepsilon_{rx'} = & 0.5\varepsilon_{xx} \sin \theta_2 \sin 2\theta (\cos^2 \theta - \sin^2 \theta) + \varepsilon_{xy} \cos \theta \cos \theta_2 - \varepsilon_{xz} \sin^2 2\theta \sin \theta_2 - \\ & \varepsilon_{yz} \sin \theta \cos \theta_2 + 0.5\varepsilon_{zz} \sin \theta_2 \sin 2\theta (\sin^2 \theta - \cos^2 \theta) \end{aligned} \quad (\text{B.7})$$

$$\begin{aligned} \varepsilon_{\theta_2\theta_2} = & \varepsilon_{xx} \sin^2 \theta \cos^2 \theta_2 - \varepsilon_{xy} \sin \theta \sin 2\theta_2 + \varepsilon_{xz} \sin 2\theta \cos^2 \theta_2 + \varepsilon_{yy} \sin^2 \theta_2 - \\ & \varepsilon_{yz} \cos \theta \sin 2\theta_2 + \varepsilon_{zz} \cos^2 \theta \cos^2 \theta_2 \end{aligned} \quad (\text{B.8})$$

$$\begin{aligned} \varepsilon_{\theta_2x'} = & 0.5\varepsilon_{xx} \cos \theta_2 \sin 2\theta (\cos^2 \theta - \sin^2 \theta) - \varepsilon_{xy} \cos \theta \sin \theta_2 - \varepsilon_{xz} \sin^2 2\theta \cos \theta_2 + \\ & \varepsilon_{yz} \sin \theta \sin \theta_2 + 0.5\varepsilon_{zz} \cos \theta_2 \sin 2\theta (\sin^2 \theta - \cos^2 \theta) \end{aligned} \quad (\text{B.9})$$

$$\varepsilon_{x'x'} = \varepsilon_{xx} \cos^2 \theta - \varepsilon_{xz} \sin 2\theta + \varepsilon_{zz} \sin^2 \theta. \quad (\text{B.10})$$

The stress components can be obtained from the strain components by replacing ε with σ in the above expressions.